Title
From instabilities to turbulence in rotating stratied ows with horizontal and vertical shear

Author
Arobone, Eric Moore

Publication Date
2014

Peer reviewed|Thesis/dissertation

UNIVERSITY OF CALIFORNIA, SAN DIEGO

From instabilities to turbulence in rotating stratified flows with horizontal and vertical shear

A dissertation submitted in partial satisfaction of the
requirements for the degree
Doctor of Philosophy

in

Engineering Sciences (Mechanical Engineering)

by

Eric Moore Arobone

Committee in charge:

Professor Sutanu Sarkar, Chair
Professor Scott Baden
Professor Geno Pawlak
Professor Kraig Winters
Professor William Young

2014

The dissertation of Eric Moore Arobone is approved, and it is acceptable in quality and form for publication on microfilm and electronically:

_____

_____

_____

_____

_____

Chair

University of California, San Diego

2014

DEDICATION

To my parents and my wife for their loving support.

EPIGRAPH

Overthinking, overanalyzing separates the body from the mind. Withering my intuition leaving all these opportunities behind.

—Tool "Lateralus"

TABLE OF CONTENTS

LIST OF FIGURES

LIST OF TABLES

ACKNOWLEDGEMENTS

I wish to begin by acknowledging the unconditional love and support of my parents, Robert and Nancy. Their unwavering belief in my abilities to overcome adversity and grow as a person was instrumental to my development. I am continually inspired by their humility, compassion, optimism, and perseverance throughout their incredibly challenging lives. It is impossible for me to hang my head for long when life is difficult knowing all the challenges they have overcome without becoming embittered or callous. Additionally, I wish to show appreciation for the love and friendship provided by my wife, Kerrie, over the last seven years. Her implicit trust and support of me has made the difficulties of leaving everyone we knew in Maryland and Pennsylvania as painless as possible. Even though our work has often limited our time for each other her wit, patience, and respect has made it easier to deal with the frustration of so much time spent apart. I look forward to a lifetime of mutual growth and happiness together. I also wish to acknowledge the support of my extended family and close friends who frequently lent an ear when I needed an escape from my work.

I am grateful for the opportunities presented to me by my thesis adviser, Professor Sutanu Sarkar. Professor Sarkar and Professor Stefan Llewellyn Smith were helpful during my transition from structured undergraduate education to open-ended coursework and research. I cannot stress enough the importance of Professor Sarkar's mentorship to successes I had as a student and researcher. His ability to give his students creative control of their projects, develop a sense of pride and enjoyment from their work, and motivate success is nothing short of an art form. Professor Kraig Winters' influence over my work and development cannot be overstated. His course formally introduced me to linear stability analysis which has contributed greatly to this dissertation. He also gave me time-saving advice related to algorithm development using high-performance computing, helped improve my teaching, and offered informal advising and support without hesitation. I am thankful for having the opportunity to learn much about scientific computing and databases from Professor Scott Baden and his student, Alden. While working as his teaching assistant, Professor Geno Pawlak helped me greatly improve my

teaching skills, which were initially rather abysmal. Lastly, Professor Bill Young's theory seminar on ocean surface processes assisted the latter stages of my thesis research.

I wish to acknowledge current and former members of Professor Sarkar's research group for support and friendship. Kyle was instrumental in helping me get my feet off the ground after first joining the group through both friendly discussions and through help with understanding the tricks of the trade. Bishakh's work ethic and intensity were contagious and we accomplished much together during our occasional collaborative work binges. Discussions with Hieu have been very helpful in part due to the proximity of our research areas, but also because of his openness to spontaneous discussion. Matt, Narsimha, Vamsi, Anikesh, Masoud, Karu, and Iman have also contributed to making my time in Professor Sarkar's lab as pleasant as possible and have aided me through constructive criticism of my work. Professor John Taylor has assisted me greatly through conversations at conferences and by offering pointers on my manuscripts.

I am thankful for my time at Penn State University and the quality of its undergraduate education. Classes and discussions with math Professor Leonid Berlyand were instrumental in my preparedness for graduate coursework. Informal advising by my fluid mechanics teacher, Professor Kendra Sharp, eventually led to my decision to pursue research and graduate school. I want to also thank Warren and Tom of the Penn State Applied Research Lab for introducing me to fluid dynamics research.

I owe many thanks to Irwin and Joan Jacobs for their commitment to the UC San Diego engineering school and for providing financial support for my first two years of graduate school. Without their fellowship I likely would have not been able to join UC San Diego. The next three years of support were provided by the National Science Foundation grant OCE-0835839, for which I am grateful. Computational resources from San Diego Supercomputing Center's Triton Affiliations and Partners Program and the Extreme Science and Engineering Discovery Environment enabled much of the research contained in this thesis.

The contents of Chapter 2 are published in the *Physics of Fluids Journal*. E.

Arobone and S. Sarkar. "The statistical evolution of a stratified mixing layer with horizontal shear invoking feature extraction", Phys. Fluids, 22, 115108, 2010. The dissertation author was the primary researcher and the research supervisor was the co-author of the paper.

The contents of Chapter 3 are published in the *Journal of Fluid Mechanics*. E. Arobone and S. Sarkar. "Evolution of a stratified rotating shear layer with horizontal shear. Part I. Linear stability", J. Fluid Mech., 703, 29-48, 2012. The dissertation author was the primary researcher and the research supervisor was the co-author of the paper.

The contents of Chapter 4 are published in the *Journal of Fluid Mechanics*. E. Arobone and S. Sarkar. "Evolution of a stratified rotating shear layer with horizontal shear. Part 2. Nonlinear evolution", J. Fluid Mech., 732, 373-400, 2013. The dissertation author was the primary researcher and the research supervisor was the co-author of the paper.

The contents of Chapter 5 are in the process of being submitted for publication in the *Journal of Fluid Mechanics*. The dissertation author is the primary researcher and the research supervisor is the co-author of the paper.

VITA

2008	B. S. in General Mathematics and Mechanical Engineering, Pennsylvania State University, University Park, PA.
2010	M. S. in Engineering Sciences (Mechanical Engineering), University of California, San Diego, La Jolla, CA.
2014	Ph. D. in Engineering Sciences (Mechanical Engineering), University of California, San Diego, La Jolla, CA.

PUBLICATIONS

JOURNAL PAPERS

E. Arobone and S. Sarkar. "Evolution of a stratified rotating shear layer with horizontal shear. Part 2. Nonlinear evolution", *J. Fluid Mech.*, 732, 373-400, 2013.

E. Arobone and S. Sarkar. "Evolution of a stratified rotating shear layer with horizontal shear. Part I. Linear stability",*J. Fluid Mech.*, 703, 29-48, 2012.

E. Arobone and S. Sarkar. "The statistical evolution of a stratified mixing layer with horizontal shear invoking feature extraction", *Phys. Fluids*, 22, 115108, 2010.

ABSTRACT OF THE DISSERTATION

From instabilities to turbulence in rotating stratified flows with horizontal and vertical shear

by

Eric Moore Arobone

Doctor of Philosophy in Engineering Sciences (Mechanical Engineering)

University of California, San Diego, 2014

Professor Sutanu Sarkar, Chair

Two idealized rotating and stratified flows are explored using linear stability analysis and three-dimensional direct numerical simulations. The first problem explores barotropic mean flow containing horizontally-oriented shear flow in the form of a mixing layer. The second problem explores a uniform baroclinic mean flow in the form of a homogeneous density front in thermal wind balance with uniform vertical shear. Both flows are explored using Richardson and Rossby numbers appropriate for submesoscale shear flows, with lateral length scales of roughly 1 to 20 kilometers. The horizontal shear flow results in simultaneous inertial and barotropic instabilities provided the mixing layer vorticity is opposite in sign and substantially greater in magnitude than the Coriolis parameter. When

the vorticity of the mixing layer is opposite in sign and similar in magnitude to the Coriolis parameter the barotropic instability is fundamentally altered. The vertical wavenumber associated with this new instability increases by an order of magnitude destabilizing barotropic vortices leading to increased turbulence intensity well outside of the inertially unstable regime.

Symmetric instability (fluctuations have no along-front variation and are aligned with isopycnals) has been identified in the literature as a potential route to turbulence at fronts as an alternative to wind-driven boundary layer mixing. Linear analysis and simulations of a uniform baroclinic flow in initial geostrophic balance performed here suggest that the instability responsible for initiating transition to turbulence should be near-symmetric and not exactly symmetric as predicted for asymptotically large time scales. Owing to near-symmetry, the instability fundamentally differs from the purely symmetric instability due to currents crossing surfaces of constant density and tapping the reservoir of potential energy available in the front. The presence of strong vertical shear only intensifies this effect as time increases. A highly-resolved turbulent simulation demonstrates a pathway to turbulence from quiescent flow via near-symmetric currents which succumb to shear-convective instabilities which in turn act to destabilize vorticity fluctuations aligned with the mean vorticity in the base flow. Once these fluctuations are sufficiently strong enough, the flow three-dimensionalizes and rapidly breaks down into turbulence throughout the domain.

Chapter 1

Introduction

The submesoscale regime lies between the large anisotropic mesoscale, well approximated by geostrophic and hydrostatic balance, and the nearly isotropic microscale. Submesoscale turbulence is characterized by horizontal length scales of $L \sim \mathcal{O}(1-10\text{km})$, and by horizontal flow varying on times scales of $U/L \sim \mathcal{O}(1\text{day})$. Balanced dynamics (e.g. quasigeostrophy) are characterized by an inverse energy cascade and vanishing dissipation as $Re = UL/\nu \to \infty$, as is the case for two-dimensional turbulence. Submesoscale turbulence is the term used to collectively refer to mechanisms which enable an energy cascade from nearly balanced flow to dissipative scales. Several such pathways have been identified through observations and simulations over the last couple of decades (McWilliams, 2010).

It was long thought that the submesoscale regime was populated almost exclusively by inertia-gravity waves, however this was called into question when it was pointed out that vortical motions can coexist with waves on these scales (Kunze & Sanford, 1993). Resolving submesoscale features within the mesoscale upper-ocean field proved difficult until recent technological advances. A study in 1985 exploring the California Current (Flament *et al.*, 1985) gave observational evidence suggesting active submesoscale processes in the upper ocean. Here, sea surface temperature plots were used to infer the evolution of an upwelling filament with barotropic instabilities of horizontal scale $\sim$ 15 km. A front southwest of Bermuda was explored in 1986 by towing a profiling CTD called SeaSoar and using a ship-mounted Doppler current profiler (Pollard & Regier, 1992). Here, rapid

time scales and rapid changes in potential vorticity $\left(Q = -\rho_0^{-1}\left(\omega_i + \delta_{i3} f\right) \partial\rho/\partial x_i\right)$ were observed over 10 km scales along isopycnals. Also, small surface-trapped eddies played an important role in mixing and transport across the thermocline. In 2004, the Subtropical Front in the north-east pacific was studied using an undulating CTD system (Hosegood *et al.*, 2006). Wavelet analysis showed that horizontal density variability was significant down to 2 km scales, significantly smaller than previously thought. In 2007, a front within the Kuroshio was explored using freely-drifting and towed instruments for a matter of weeks resolving scales from kilometers to millimeters (D'Asaro *et al.*, 2011). Here, results indicated that unforced submesoscale instabilities were more important in the development of upper ocean turbulence than fluxes of heat, moisture or momentum at the surface.

1.1 Submesoscale Horizontal Shear

Turbulent stratified flow with horizontal shear occurs in a wide variety of geophysical scenarios. Boundary currents, topographical wakes, and flow from river deltas can all result in strong horizontal shear subjected to nearly vertical stratification. In many geophysical flows there is an abundance of horizontal kinetic energy organized into vortices and there is uncertainty regarding the fate of this energy. In the 1980s, the POLYMODE Local Dynamics Experiment identified, in greater detail and quantity than previously studied, unusually long-lived submesoscale coherent vortices (SCVs). SCVs are quite intermittent in comparison to inertia-gravity waves and submesoscale turbulence, but prove quite effective in transporting chemicals and tracers from their origin. There is a strong anticyclone bias present in SCVs, posited as due to intense localized mixing events at generation sites (McWilliams, 1985).

Spiral eddies on the sea surface have been observed at the ocean's surface since the Apollo Mission, being roughly $10 - 25$ km wide and predominantly cyclonic (Munk *et al.*, 2000). The spirals are noticeably absent within 6° of the equator, and are highly concentrated in the Mediterranean Sea in Autumn. The structure of many of the eddies is reminiscent of the prototypical "cat's eye" pattern

associated with horizontal shear instability. The preference for cyclone formation was suggested to be due to instabilities which target anticyclonic vortices and the more rapid growth of cyclonic shear in frontal jets. It was later argued that oceanic spirals were primarily due to ageostrophic baroclinic instability, with the observed shear instability being a component of secondary circulations (Eldevik & Dysthe, 2002).

There are observations of asymmetry between cyclonic and anticyclonic vortices in geophysical flows, e.g. figure 1 of Potylitsin & Peltier (1998) which shows asymmetry of the von Karman vortex street in the lee of mountains on the island of Jan Mayen. Flament *et al.* (2001) observed a horizontal shear layer, containing anticylonic vortices having $\omega_3 \sim -f$, forming in the westward North Equatorial Current past the island of Hawaii. The shear layer grew in thickness owing to paring of these anticylonic vortices. It was suggested that stronger vortices were not observed due to inertial instability. Anticyclones are quite difficult to generate in the laboratory in a homogeneous fluid, e.g. Kloosterziel & van Heijst (1991) and Afanasyev & Peltier (1998).

The so-called balance equations are intermediate to the geostrophic and primitive equations in accuracy, defined as to retain a global energy invariant (Gent & McWilliams, 1983*a*). Three conditions resulting in singularity of the balance equations were identified, suggesting loss of geostrophic or hydrostatic balance (Gent & McWilliams, 1983*b*). The first condition is the change of sign of absolute vorticity ($A = \omega_3 + f$), which coincides with onset of the inertial instability. The second condition is the change in sign of the vertical density gradient, which indicates gravitational instability. The last condition coincides with change in sign of the difference between absolute vorticity and strain rate ($A - s$), which gives rise to the ageostrophic anticyclonic instability. This instability provides a mechanism to generate unbalanced flow, albeit with slower growth rates than observed for the largely balanced baroclinic instability. While the baroclinic instability can manifest in the submesoscale regime it is more relevant to the slumping of fronts and hence restratification than it is to the forward energy cascade (Molemaker *et al.*, 2005).

1.2 Submesoscale Vertical Shear

Submesoscale frontogenesis is a well-known mechanism which enables a forward cascade of energy from balanced to unbalanced flow. In frontogenesis, density gradients are amplified through nonlinear interactions between horizontal flow and horizontal density gradients in the presence of background larger-scale straining. Frontogenesis results in frontal meanders which generate coherent vortices. This mechanism is ubiquitous in the upper ocean due to the presence of lateral buoyancy gradients and most visible when the mixed layer is deep. It is important to note that while submesoscale fronts meander due to unbalanced submesoscale motions, the fronts themselves are usually very nearly in balance (Thomas *et al.*, 2008).

For Eady flow, a vertically sheared current $u_1 = Sx_3$ in balance with a stably stratified density field $\rho = M^2 x_2 + N^2 x_3$, unbalanced flow is due primarily to frontogenesis and subsequent frontal instabilities (Molemaker *et al.*, 2010). Horizontal shear is the primary driver for the observed frontal instabilities. Because of the lack of a surface mixed layer these simulations have a very large deformation radius, effectively eliminating the submesoscale baroclinic instability, confining it to larger length scales.

The symmetric instability (SI) is an instability of baroclinic zonal flows where perturbations contain no longitudinal variation, and are thus two-dimensional. The stability analysis of Stone (1966) explores a balanced zonal flow of the form $u(z)$ which is balanced by a temperature field of the form $\theta(y, z)$. The symmetric instability dominates when the Richardson number ($Ri = N^2/S^2$) is between 0.25 and 0.95 for $S = ||\partial \boldsymbol{u}_h/\partial x_3||$, while baroclinic and Kelvin-Helmholtz (K-H) instabilities dominate at higher and lower Ri, respectively. In a more general case, including horizontal shear, instability manifests when potential vorticity ($q = -\rho_0^{-1}(\omega_i + f\delta_{i3})\partial\rho/\partial x_i$) or PV is of opposite sign of the Coriolis parameter in stably stratified regions of as noted in Hoskins (1974). These more general flows are susceptible to inertial/centrifugal and symmetric instabilities which act on absolute vertical vorticity opposing planetary rotation and vertical shear, respectively. In general, balanced baroclinic zonal flows have PV given by $q = -fS^2 + (\omega_3 + f)N^2$ (Thomas *et al.*, 2013).

The symmetric instability occurs when potential vorticity and the Coriolis parameter have opposite signs, or $fQ < 0$. This instability can also yield a forward cascade to energy dissipation. In the limit of pure symmetric instability, fluctuations receive energy from the vertical shear production. A two-dimensional simulation of an idealized front with negative fQ gave rise to slantwise motions associated with symmetric instability, but significant fluctuation growth was only observed once symmetric instability reached finite amplitude and a secondary shear instability occurred (Taylor & Ferrari, 2009). Observations of the Gulf Stream show that the energy injection to small scales via symmetric instability is the same order of magnitude as energy removal via baroclinic instability (Thomas *et al.*, 2013).

An exceptionally sharp (1km) front near the beginning of the Kurushio extension was investigated by D'Asaro *et al.* (2011). Shipboard measurements, a Lagrangian float and a towed profiling vehicle allowed for measurements of turbulence intensity (inferred from vertical motions of the float), temperature, salinity, pressure, and velocity profiles. The front is less than $1km$ wide and about $20m$ deep and contains vertical motion resulting from upper ocean turbulence. Dissipation at the front is estimated to be $10 - 20$ times stronger than outside the front but surface winds and cooling are too weak to explain the observed turbulence. The potential vorticity was found to take the opposite sign of f for 0.2 days while the vessel passed through the front, strongly suggesting symmetric instability as the relevant mechanism. These results suggest that in some regions of the upper ocean, lateral density gradients and symmetric instability may be more important than atmospheric forcing in setting turbulence intensity.

Chapter 2

Nonlinear Evolution of a Stratified Shear Layer with Horizontal Shear

2.1 Introduction

Turbulent stratified flow with horizontal shear occurs in a wide variety of atmospheric and oceanographic scenarios. Boundary currents, wakes of towed or self-propelled objects, and flow from river deltas can all result in strong horizontal shear subjected to nearly vertical stratification. In geophysical flows there is an abundance of horizontal kinetic energy organized into vortices whose vertical structure is of interest. While the effect of stratification on turbulent flow with vertical mean shear has received considerable attention in the case of two streams with uniform but different density (Thorpe, 1973; Koop & Browand, 1979; Smyth & Moum, 2000*b*,*a*; Smyth *et al.*, 2001; Strang & Fernando, 2001; W.R. & Caulfield, 2003) as well as in streams with ambient stratification (Tse *et al.*, 2003; Pham *et al.*, 2009; Pham & Sarkar, 2010), the horizontal case has only been investigated a handful of times (Jacobitz & Sarkar, 1998, 2000; Basak & Sarkar, 2006).

Systematic study of flows with horizontal shear started with linear theory which was employed to study the effect of stratification on the stability of the

mean flow profile. The instability of a two-dimensional shear flow, $U(x_2, x_3)$ with both vertical and horizontal shear, in a medium with uniform buoyancy frequency, N, was investigated in Blumen (1971) under the assumptions of hydrostatic and inviscid perturbations. A sufficient condition for stability in the general situation of non-planar shear was not found. In the simplified case of one-dimensional shear, $U(x_2)$, in a stratified fluid, instability was found to require an inflection point in the flow profile and developed an additional dependence on the vertical mode of oscillation. Three-dimensional instability of a horizontally oriented hyperbolic tangent mixing layer, $U(x_2) = U_0 \tanh(x_2/L)$, in a fluid with constant N was explored by Deloncle *et al.* (2007) because Squire's theorem does not apply to this particular flow. While the most unstable modes remain two-dimensional with (x_1, x_2) dependence, stratification was found to destabilize a broad range of three-dimensional perturbations. Three-dimensional perturbations with $k_3 L < 1/Fr_h$, where $Fr_h = U_0/LN$, yielded growth rates very near those associated with two-dimensional perturbations.

Subsequently, nonlinear simulations into the regime of turbulence were carried out in the case of uniform shear flow. Linearized disturbances in flow with uniform shear do not show exponential growth but algebraic growth is possible. Nonlinearly evolving disturbances in unstratified flow with uniform shear develop into turbulence with exponentially growing kinetic energy. The case of uniform vertical mean shear, $U = Sx_3$ in a stratified fluid has been studied extensively and it is found that, for gradient Richardson number $Ri_g = N^2/S^2$ that exceeds a critical value (0.18 to 0.25), turbulence is extinguished. The case of non-vertical shear was studied by Jacobitz & Sarkar (1998) in a DNS study of stratified flow with mean velocity, $U = S\sin(\theta)x_2 + S\cos(\theta)x_3$. The case with purely horizontal shear, $\theta = \pi/2$, showed significantly higher turbulence levels compared to purely vertical shear. Nevertheless, for a sufficiently high stratification with $N^2/S^2 \simeq 2$, turbulence was extinguished in the case with purely horizontal shear as well.

The next step was simulation of a turbulent flow with an inflectional mean velocity that allows linear instabilities. A shear layer with velocity difference ΔU in the horizontal (x_2) direction and uniform stratification was investigated by Basak

& Sarkar (2006), emphasizing the structure of the density and vorticity fields. Although the vertical velocity was suppressed by stratification, inflectional shear maintained horizontal velocity fluctuations preventing relaminarization. In the stratified cases, Kelvin-Helmholtz (KH) rollers merged to form coherent vortical structures which persisted for much longer times than in the unstratified case, where KH rollers were short-lived due to secondary instabilities. Co-rotating coherent structures also emerge in simulations of unstratified mixing layers at moderate Reynolds numbers (Winant & Browand, 1974), but buoyancy plays a greater role in dynamics than inhibiting vertical motion and affects the evolution of coherent structures. A lattice of vortex cores, with vertical core height, l, such that $Fr = \Delta U/Nl = O(1)$, emerged in the stratified cases (Basak & Sarkar, 2006) resulting from the tilting and truncation of columnar vortical structures. Density intrusions were found to propagate laterally from the shear layer owing to buoyant parcels of fluid expelled from the coherent structures spreading laterally like gravity currents.

Given the occurrence of coherent vortices with vertical structure in the simulations (Basak & Sarkar, 2006) of *turbulent* flow with horizontal shear, it is appropriate to review the literature on vertical structure of stratified vortices in simpler configurations. A pair of counter-rotating vortices was shown experimentally by Billant & Chomaz ($2000a$) to undergo a zigzag instability characterized by a vertically modulated twisting and bending of the vortex pair. The accompanying theoretical analysis (Billant & Chomaz, $2000c$) suggests that the vertical wavelength l_3 corresponds to $Fr = u_h/Nl_3 \sim O(1)$. Waite & Smolarkiewicz (2008) performed simulations of a stratified counter-rotating vortex pair at a Reynolds number higher than explored in the laboratory experiment. The early-time evolution agreed with linear analysis and experiments of the zigzag instability (Billant & Chomaz, $2000a,c$) while the late-time evolution was qualitatively different owing to transition to turbulence. Deloncle *et al.* (2008) performed DNS of the zigzag instability, similar to Waite & Smolarkiewicz (2008), and showed that the transition to turbulence occurs at large buoyancy Reynolds number. The instability of a tilted Oseen-Lamb vortex was experimentally investigated by Meunier *et al.*

(2007) for the case of small inclination angles. Thin strips along the edge of the vortices showed strong shear and large density variation. Along the edges of the vortex, shear layer and jet instabilities are observed. This instability was observed at higher Froude numbers than the zigzag instability.

The current work, in contrast to the previous study of a horizontally-oriented shear layer (Basak & Sarkar, 2006), focuses on the evolution of flow statistics in the shear layer including examination of the role of coherent structures. Quantitative assessment of the role of coherent structures requires means to isolate coherent vortical flow from the rest of the flow field. Since a universally accepted definition of a vortex is currently unavailable, multiple methods of feature extraction were considered. Several commonly used vortex eduction criteria using information contained in the rate of deformation tensor, $\boldsymbol{\nabla u}$, are introduced in Chong *et al.* (1990) and Jeong & Hussain (1995), and assessed in Chakraborty *et al.* (2005) and Haller (2005). For example, the Q criterion defines a vortex as a region where the norm of the rate of rotation tensor, $\|\boldsymbol{\Omega}\|$, exceeds the norm of the rate of strain tensor, $\|\boldsymbol{S}\|$. The Δ criterion defines vortices as the regions of flow where $\boldsymbol{\nabla u}$ has complex eigenvalues, implying locally swirling flow. λ_2 identifies vortices as regions of the flow where the rotational rate exceeds strain rate only in a specific plane. Coherent vortex extraction (Farge *et al.*, 2001) separates an incoherent (small-amplitude) component from a given field. Since wavelets are isolated both with respect to length scale and physical location, they are especially suitable for stratified flows that are dominated by sparse multiscale features. This motivates an examination of wavelet-based decomposition of the vorticity field in the present problem.

2.2 Problem Definition

A temporally evolving shear layer representing two streams with velocity difference ΔU is subjected to uniform stable stratification in the vertical direction. The streamwise velocity (u_1) varies only in the transverse (x_2) direction, where the initial vorticity thickness ($\delta_{\omega,0}$) characterizes the width of the region separating the

streams. The streamwise (x_1) and vertical (x_3) directions are assumed to be infinite and homogeneous. Kinematic viscosity and thermal diffusion are denoted by ν and κ, respectively. Figure 2.1 shows a detailed schematic.

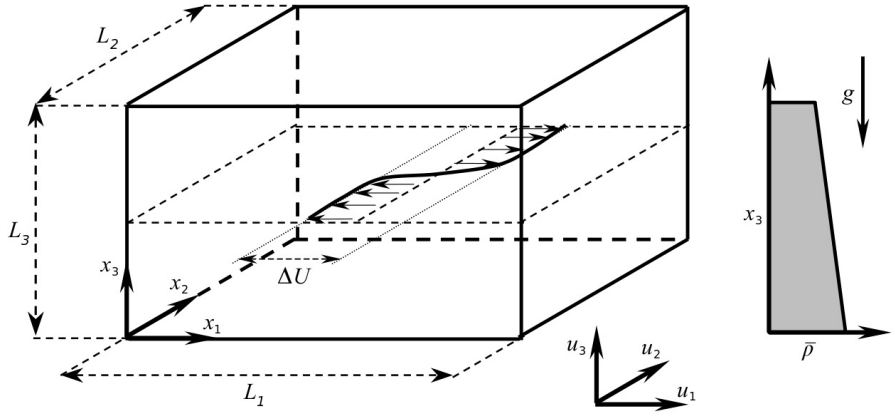

Figure 2.1: Schematic of the mixing layer.

2.2.1 Initial Conditions

The initial mean flow field is given by a hyperbolic tangent velocity profile of the following form,

$$\langle u_1 \rangle = \frac{\Delta U}{2} \tanh\left(\frac{2x_2}{\delta_{\omega,0}}\right), \langle u_2 \rangle = 0, \langle u_3 \rangle = 0. \tag{2.1}$$

Flow variables are decomposed into mean and fluctuation quantities via the Reynolds decomposition. Averaging is performed in the homogeneous directions, x_1 and x_3. Quantities surrounded by angle brackets represent means and primed variables represent fluctuations. The vorticity thickness of the mixing layer is given by

$$\delta_\omega = \frac{\Delta U}{\max\left\{\partial\left\langle u_1\right\rangle/\partial x_2\right\}}. \tag{2.2}$$

The initial fluctuating field is prescribed with three dimensional fluctuations having an energy spectrum, $E(k) = Ck^4 e^{-2(k/k_0)^2}$, which accelerates transition to turbulence. The peak wavenumber, k_0, is selected to correspond with a wavelength of $1.7\delta_{\omega,0}$. The initial turbulent kinetic energy is

$$K_0\left(x_2\right) = 0.029\left(\Delta U\right)^2 exp\left[-\left(x_2/\delta_{\omega,0}\right)^2\right], \tag{2.3}$$

such that fluctuation energy peaks at the midplane of the shear layer.

2.2.2 Governing Equations

The dimensional equations for conservation of mass, momentum, and density of an incompressible fluid are given below (dimensional variables indicated by *):

Continuity :

$$\frac{\partial u_i^*}{\partial x_i^*} = 0 \tag{2.4}$$

Momentum :

$$\frac{\partial u_i^*}{\partial t^*} + \frac{\partial\left(u_i^* u_j^*\right)}{\partial x_j^*} = -\frac{1}{\rho}\frac{\partial p^*}{\partial x_i^*} + \nu\frac{\partial^2 u_i^*}{\partial x_j^* \partial x_j^*} - g\delta_{i3} \tag{2.5}$$

Density :

$$\frac{\partial \rho^*}{\partial t^*} + \frac{\partial\left(\rho^* u_j^*\right)}{\partial x_j^*} = \kappa\frac{\partial^2 \rho^*}{\partial x_j^* \partial x_j^*} \tag{2.6}$$

The density and pressure fields are decomposed in the following manner,

$$\rho^{*}\left(x_i,t\right)=\rho_0+\overline{\rho}(x_3)+\rho^{'*}\left(x_i,t\right), \tag{2.7}$$

$$p^{*}\left(x_i,t\right)=\overline{p}(x_3)+p^{'*}\left(x_i,t\right), \tag{2.8}$$

where $\overline{\rho}(x_3)$ represents the background stratification and $\overline{p}\,(x_3)$ represents hydrostatic pressure balancing the initial density profile ($\rho_0^{*}=\rho_0+\overline{\rho}$). The non dimensional variables for this problem are given as

$$t=\frac{t^{*}\Delta U}{\delta_{\omega,0}},\quad x_i=\frac{x_i^{*}}{\delta_{\omega,0}},\quad u_i=\frac{u_i^{*}}{\Delta U}, \tag{2.9}$$

$$\rho^{'}=\frac{-\rho^{'*}}{\delta_{\omega,0}\left(d\overline{\rho}/dx_3\right)},\quad p'=\frac{p^{'*}}{\rho_0\Delta U^2}. \tag{2.10}$$

When Boussinesq approximations are assumed, the following non dimensional equations are obtained,

Continuity :

$$\frac{\partial u_i}{\partial x_i}=0, \tag{2.11}$$

Momentum :

$$\frac{\partial u_i}{\partial t}+\frac{\partial\left(u_iu_j\right)}{\partial x_j}=-\frac{\partial p^{'}}{\partial x_i}+\frac{1}{Re_0}\frac{\partial^2 u_i}{\partial x_j\partial x_j}-Ri_{b,0}\rho^{'}\delta_{i3}, \tag{2.12}$$

Density :

$$\frac{\partial\rho^{'}}{\partial t}+\frac{\partial\left(\rho^{'}u_j\right)}{\partial x_j}-u_j\delta_{j3}=\frac{1}{Re_0Pr}\frac{\partial^2\rho^{'}}{\partial x_j\partial x_j}, \tag{2.13}$$

where,

$$Re_0 = \frac{\Delta U \delta_{\omega,0}}{\nu}, \quad Ri_{b,0} = -\frac{g}{\rho_0}\frac{d\overline{\rho}}{dx_3}\frac{\delta^2_{\omega,0}}{\Delta U^2} = \frac{N^2\delta^2_{\omega,0}}{\Delta U^2},$$
$$Pr = \frac{\nu}{\kappa}.$$

Here, Pr is taken to be unity for the sake of reasonable computational cost. Dirichlet boundary conditions are enforced for all flow variables at the transverse boundaries where flow variables are fixed to the values given in Table 2.1. Periodicity is enforced in the streamwise and vertical directions through Fourier decomposition. Boundary influence increases with time as the shear layer grows laterally.

Table 2.1: Boundary conditions at the transverse boundaries

$u_1\left(x_1, -L_2/2, x_3\right) = -0.5$	$u_1\left(x_1, L_2/2, x_3\right) = 0.5$
$u_2\left(x_1, -L_2/2, x_3\right) = 0$	$u_2\left(x_1, L_2/2, x_3\right) = 0$
$u_3\left(x_1, -L_2/2, x_3\right) = 0$	$u_3\left(x_1, L_2/2, x_3\right) = 0$
$\rho^{'}\left(x_1, -L_2/2, x_3\right) = 0$	$\rho^{'}\left(x_1, L_2/2, x_3\right) = 0$
$p^{'}\left(x_1, -L_2/2, x_3\right) = 0$	$p^{'}\left(x_1, L_2/2, x_3\right) = 0$

Table 2.2: Simulation parameters.

case	Re_0	$Ri_{b,0}$	Pr	L_1	L_2	L_3	N_1	N_2	N_3
$A0$	680	0	1	43.0	25.8	12.9	640	384	192
$A1$	680	0.113	1	86.0	68.8	25.8	640	512	192
$A2$	680	0.358	1	86.0	68.8	25.8	640	512	192
$A3$	680	1.132	1	86.0	68.8	25.8	640	512	192
$A3_{low}$	680	1.132	1	86.0	68.8	25.8	640	512	192
$2D$	680	-	1	3440	51.6	0	25,600	384	1

2.2.3 Computational Method

The numerical algorithm is different from Basak & Sarkar (2006) who employed a second-order finite difference method in all directions. Instead, we employ spectral collocation in the streamwise and vertical directions and finite difference

in the transverse direction. The transverse velocity is stored on a grid staggered in the transverse direction. The Navier-Stokes and density equations are marched using a third order mixed Runge-Kutta/Crank-Nicolson time scheme with viscous terms treated implicitly. A Rayleigh damping function is used near the $x_2 = \pm L_2/2$ boundaries, with a width of approximately $3\delta_{\omega,0}$, to prevent spurious reflections. The Poisson equations for pressure and removal of velocity divergence are solved using the Thomas algorithm. Parallelization is accomplished using MPI. Case specific computational details are shown in Table 2.2.

2.2.4 Case Study

A total of six simulations were performed as listed in Table 2.2, five of which used the initial conditions described in section 2.2.1. Case $A0$ investigates the evolution of an unstratified mixing layer, while cases $A1$, $A2$, and $A3$ explore the effect of various values of uniform stratification. For comparison, case $2D$ investigates the evolution of a two dimensional mixing layer. Case $A3_{low}$ is identical to case $A3$, however, initial velocity fluctuations have an amplitude smaller by a factor of 10^{-3}. This allows investigation of the effect of linearly evolving initial conditions on statistical evolution and the formation of vortical structures. In case $2D$, a very large value of L_1 was used so that statistics would be reproducible, since averaging is performed across pencils instead of planes as in the $3D$ simulations.

2.3 Effects of Buoyancy on Mean Flow and Turbulent Stresses

The bulk Richardson number ($Ri_b = N^2\delta_\omega^2(t)/\Delta U^2$) represents the ratio of the stabilizing effect of buoyancy to the destabilizing effect of horizontal shear. N^2 is varied between simulations to investigate the effect of stratification on dynamics. In addition to an unstratified case, a two dimensional simulation was performed for comparison against the limit of $N^2/S^2 >> 1$. Statistics from case A0 validated well against the results of Pantano & Sarkar (2002) and Basak & Sarkar (2006).

Thickness growth rates, $Ri_b(Nt)$, and visualizations of vorticity components agreed well with the results of Basak & Sarkar (2006) for stratified runs. Growth rates for the two dimensional and stratified cases are shown in figure 2.2(a). Here, growth rate is defined using the momentum thickness, $\delta_\theta = \int_{-L_2/2}^{L_2/2} \frac{1}{4} - \left(\frac{\langle u_1 \rangle (x_2)}{\Delta U}\right)^2 dx_2$. Plots of $Ri_b(Nt)$ and $Ri_b(t)$ for the stratified simulations are given in figure 2.2(b),(c). $Ri_b(Nt)$ is nearly proportional to $(Nt)^2$, implying the eventual dominance of stratification effects in all stratified cases. In case $A3$, the bulk Richardson number reached values in excess of 80, while exhibiting substantial vertical variability.

2.3.1 Self-Similarity of Turbulence Statistics and the Large Richardson Number Limit

The temporal evolution of turbulence intensities in cases with high stratification, cases A3 and A2, show an approach to an asymptotic profile, indicative of self-similar evolution. Figure 2.3(a) illustrates the evolution towards self-similarity in profiles of the spanwise root mean square (rms) fluctuation for case A3. After an initial transient, turbulence levels in stratified cases depend primarily on the local value of $Ri_b(t)$. This result is illustrated by figure 2.3(b) which compares profiles between the stratified cases at comparable values of $Ri_b\,(t)$. The A0 case also reaches self-similar energetic profiles after a much shorter initial transient process due to its intense turbulent fluxes. Additionally, the 2D case reaches self-similar behavior far more quickly than the stratified cases.

In the limit of $Ri_b(t) \gg 1$, turbulence statistics such as $\langle u_1' u_1' \rangle$, $\langle u_2' u_2' \rangle$, $\langle u_1' u_2' \rangle$, and $\langle \rho' u_3' \rangle$, lose their dependence on $Ri_b(t)$ in the stratified simulations and, therefore, self-similar evolution is observed. Case $A3$ exhibits self-similar energetics over the longest range of time while case $A2$ exhibits self-similarity briefly before experiencing strong boundary effects. Nevertheless, because $Ri_b \propto (Nt)^2$, eventually all flows with nonzero N will reach the $Ri_b \gg 1$ limit as suggested in figure 2.2(c).

The influence of initial disturbance levels was also explored for the stratification of case A3. Most second-order turbulence statistics showed agreement between cases $A3$ and $A3_{low}$ after an initial adjustment period. Other statistics,

such as $\langle u_3' u_3' \rangle$ and $\langle \rho' \rho' \rangle$, showed some differences dependent upon the initial turbulent kinetic energy.

According to Billant & Chomaz (2001) for a strongly stratified inviscid flow with quasi-horizontal eddies that evolves self-similarly vertical velocity fluctuations should scale like $u_3' \sim \Delta U Ri_b^{-1/2}$ and scalar fluctuations should scale like $\rho' \sim (d\bar{\rho}/dx_3)\delta_\omega Ri_b^{1/2}$. For cases $A1$ and $A2$ this type of scaling does not seem to hold in the self-similar regime. Case $A3$ however appears to have a small enough horizontal Froude number for the strongly stratified assumption to hold and a similar scaling is observed.

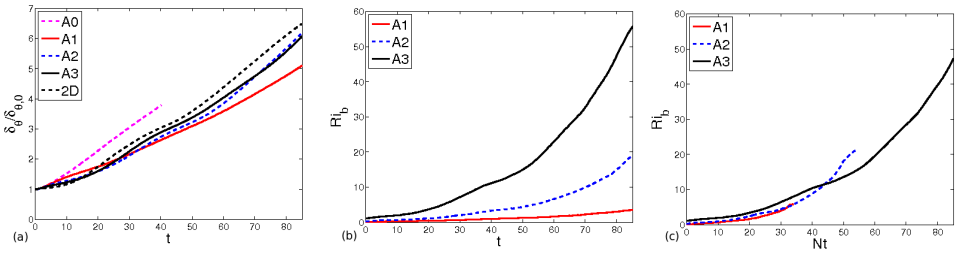

Figure 2.2: (a) The evolution of momentum thickness of the shear layer. The evolution of bulk Richardson number as a function of (b) t and (c) Nt. To convert from t to Nt multiply by 0.336, 0.828, and 1.064 in stratified cases A1, A2 and A3, respectively.

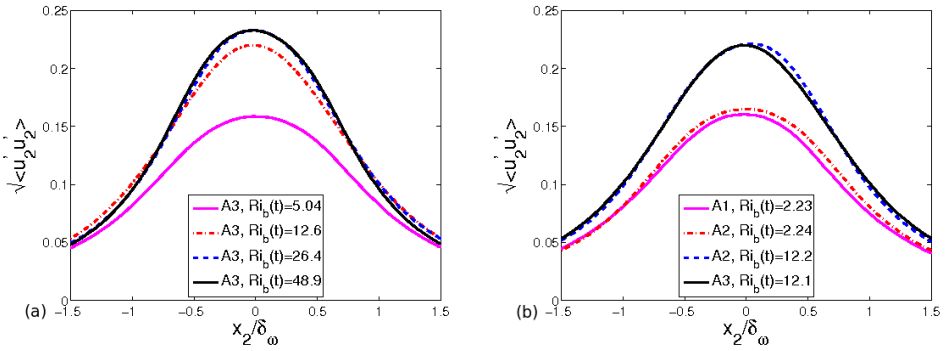

Figure 2.3: Profiles of transverse fluctuations. (a) Evolution in the strongly stratified case (A3). (b) Cases A1 and A2 at different times but matching Ri_b. Similarly, cases A2 and A3 at different times but matching Ri_b.

2.3.2 Comparisons Among Unstratified, Stratified, and Two-Dimensional Results

Comparisons are made among the statistics of unstratified, stratified, and two-dimensional shear layers once self-similarity is attained. The stratified cases show the emergence of coherent vortical structures as illustrated later in Figure 2.10. These coherent structures change turbulence profiles as discussed below.

Statistical quantities of interest are presented in Figure 2.4, showing key similarities and differences. Profiles of $\langle u_1' u_1' \rangle$ and $\langle u_2' u_2' \rangle$ in the stratified cases are very similar to those found in the two-dimensional shear layer. The agreement is due to the coherent nature of the ω_3 field associated with the columnar coherent structures. Turbulent shear stress, $\langle u_1' u_2' \rangle$, shows reasonable agreement between the two-dimensional and stratified cases except outside of $|x_2| < \delta_\omega$ where, for the stratified case, shear stress takes much larger values than the two-dimensional case. This is due to the formation of density intrusions which propagate laterally from the shear region. These intrusions advect slower-than-ambient flow horizontally, contributing to the increased levels of $\left|\langle u_1' u_2' \rangle\right|$ well outside of the region containing vortical structures.

The profile of $\langle u_1' u_1' \rangle$ in cases $A3$ and $2D$, figure 2.4(a), develops a profile consisting of two distinct regions. The region close to the centerline ($|x_2| < \delta_\omega/2$) we designate the 'head' of the profile while the surrounding region we identify as the 'shoulders'. The development of the 'head' coincides with vortex staggering, which would not emerge if vortices were centered about the centerline. In fact, for a row of Rankine vortices $\langle u_1' u_1' \rangle$ would take the value of zero at the centerline. The centerline value of transverse fluctuations, $\langle u_2' u_2' \rangle$, show significant growth in the stratified runs due to coherent structures with well organized ω_3 fields, increasing transverse momentum transfer in comparison to the weakly organized vorticity field observed in case A0.

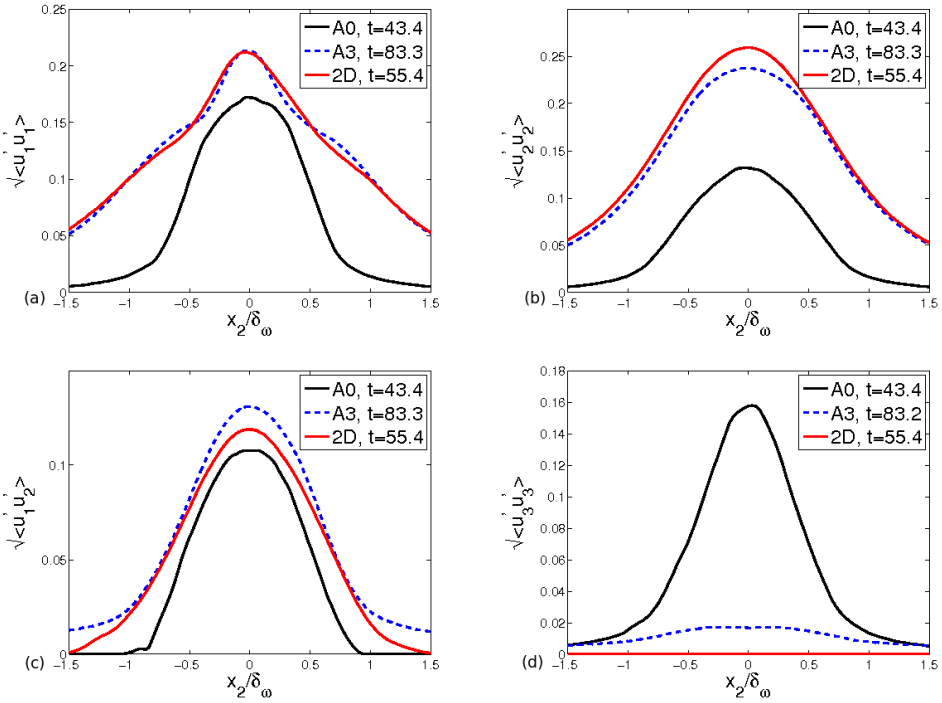

Figure 2.4: Comparison of self-similar statistics of stratified, unstratified, and two-dimensional simulations

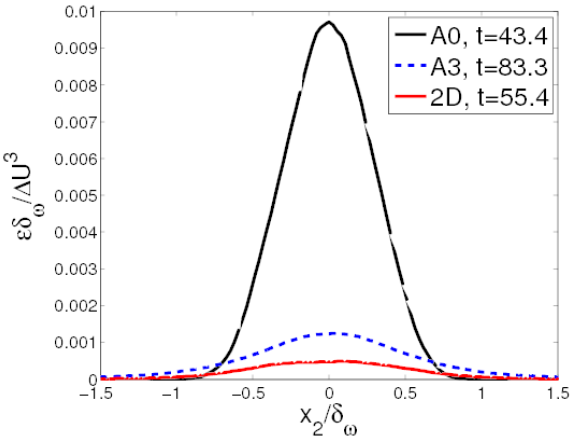

Figure 2.5: Comparison of dissipation from stratified, unstratified, and two-dimensional simulations

2.4 Evolution of Dissipation Statistics

Irreversible viscous dissipation of fluctuating kinetic energy, ϵ, is defined as $\epsilon = \frac{2}{Re_0}\left\langle s'_{ij} s'_{ij} \right\rangle$, where $s'_{ij} = \frac{1}{2}\left(u'_{i,j} + u'_{j,i}\right)$. Irreversible dissipation of scalar variance due to diffusive effects, ϵ_ρ, is defined as $\epsilon_\rho = \frac{2}{Re_0 Pr}\left\langle \rho'_{,i} \rho'_{,i} \right\rangle$.

A substantial reduction in turbulent dissipation is observed in the presence of stratification, as shown in Figure 2.5. Dissipation, however, does not decrease to the levels found in two-dimensional simulations due to the large vertical gradients of velocity induced by buoyancy. Turbulent dissipation maintains integrated values, $\int_{-L_2/2}^{L_2/2} \epsilon dx_2$, at least two to three times larger in the stratified cases than observed in the two-dimensional case. Thin dislocations of vorticity develop as vertical shearing leads to pockets of vorticity subjected to strong vertical viscous diffusion contributing greatly to energy dissipation. The vertical distance across these dislocations, i.e. the dislocation thickness, is small compared to horizontal thickness.

Time evolution of the integrated fluctuating viscous and scalar dissipations as well as buoyancy Reynolds number, $Re_B = \epsilon/\nu N^2$, are plotted for the stratified cases in Figure 2.6. The reproducible results of self-similarity seen in the evolution of turbulent stresses do not apply to turbulent and scalar dissipation until much later in the simulations. These show significant variation between cases $A1$ - $A3$, which is likely due to the differences in dislocation thickness. Dislocation thickness, l_d scales with $\sqrt{\nu/N}$ between cases which helps explains why the integrated dissipation reaches its largest values in case $A3$. Case $A1$ shows higher values of integrated dissipation initially due to the far greater presence of small scale turbulence, but vertical gradients become so significant in the dislocations that case $A3$ eventually dominates.

Initially there is a drop in viscous dissipation, seen in Figure 2.6(a), as viscosity suppresses high wavenumber components of the initial fluctuations. The subsequent drop in dissipation when $5 \lesssim t \lesssim 20$ corresponds to the time when the vorticity field organizes into large columnar vortices. It is plausible that the $2D$ curve could represent the limit of $N^2/S^2 \to \infty$ during this process. The following period over which dissipation increases, $20 \lesssim t \lesssim 80$, is when dislocations form

and grow as a result of vertical shearing and instabilities acting on the vortices. The slope at which dissipation increases during this time period is proportional to N in the stratified cases, implying that buoyancy plays a role in the small scale dynamics of these cases.

The buoyancy Reynolds number shows a steep decrease initially in case $A1$ which continues until boundary effects become significant.The increase in dissipation due to dislocations is so significant in case $A3$ that the centerline value of ϵ increases when $40 \lesssim Nt \lesssim 80$. This intensification of centerline dissipation could result in a reemergence of turbulent behavior at late time, provided dislocations contain sufficiently strong vertical shear for Kelvin-Helmholtz instabilities and turbulence to overcome stratification.

Slices of local $\widetilde{Re}_B = \widetilde{\epsilon}/\nu N^2$ are shown in the x_2 midplane for cases $A1$ and $A3$ in Figure 2.7. In both cases, localized patches of high $\widetilde{Re}_B$ are seen, which explains why turbulent behavior is observed in case $A1$ although the mean value is $Re_B \approx 1.28$. In all three stratified cases, the ratio of $\epsilon_{\max}/\widetilde{\epsilon}$ takes values between 30 and 50 due to the localized nature of the dissipation field after the formation of spatially sparse dislocations. Thus, although the mean buoyancy Reynolds number is close to unity, the flow is far from laminar. The dissipation is also highly anisotropic, i.e. the contribution of vertical gradients of horizontal velocity dominate at large Ri_b. The values of Re_B in all three stratified cases are much smaller than those observed in the ocean (e.g. EUC system), which is due to both physics and computational limitations. The lack of baroclinicity and mean vertical shear keep dissipation relatively small and isolated. Additionally, since DNS is used Re_0 takes values much smaller than expected for a typical horizontal shear flow in the ocean, which indirectly tends to reduce Re_B values.

Local gradient Richardson numbers, $Ri_g = N^2/\left(u_{1,3}^2 + u_{2,3}^2\right)$, of order one are common within the coherent structures. This result is consistent with the hypothesis of Lilly (1973) and results of Riley & de Bruyn Kops (2003). Vertical shear is intense within the dislocations leading to local Richardson numbers of less than a half in case $A3$. Visualizations of local Ri_g are nearly identical to local Re_B, especially in case $A3$, and hence not included.

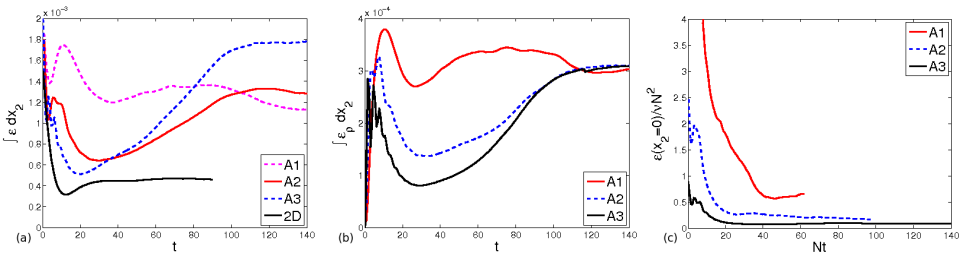

Figure 2.6: Evolution of (a) integrated viscous dissipation, (b) integrated scalar dissipation and (c) the buoyancy Reynolds number, $\widetilde{Re}_B = \widetilde{\epsilon}/\nu N^2$ at the x_2 midplane.

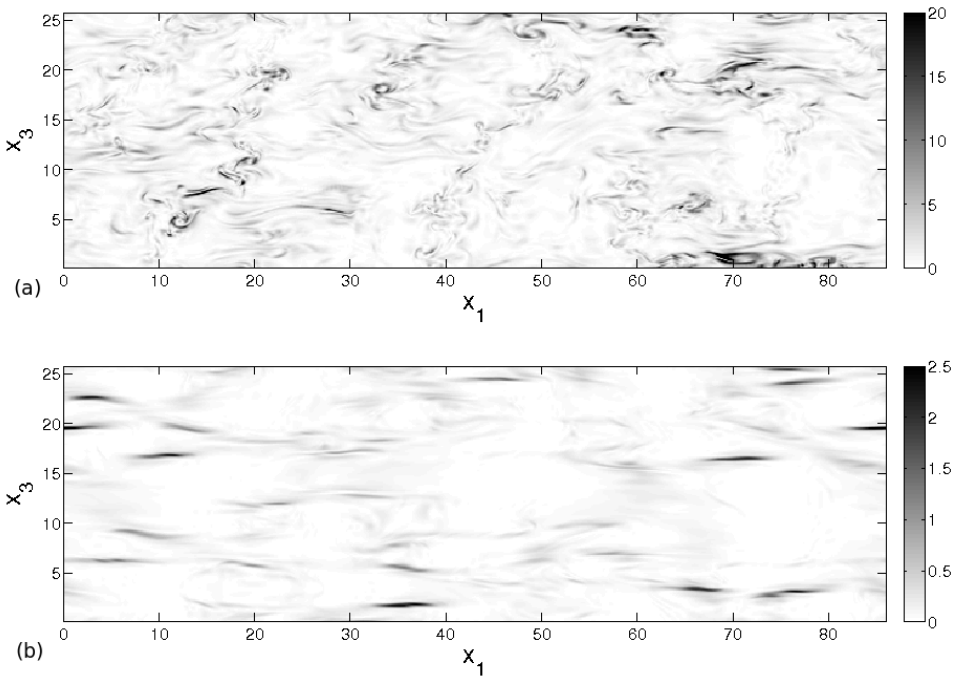

Figure 2.7: Vertical cuts of the x_2 midplane with $\widetilde{\epsilon}/\nu N^2$ from (a) the weakly stratified case (A1) and (b) the strongly stratified case (A3) (bottom) at times $t = 84.2$ and $t = 82.2$ respectively.

2.5 Turbulent Kinetic Energy Budgets

The evolution equation for the fluctuating kinetic energy is

$$\frac{\partial K}{\partial t} = P - \epsilon + B - \frac{\partial T}{\partial x_2}. \tag{2.14}$$

Here, K represents turbulent kinetic energy (TKE) defined as

$$K = \frac{1}{2}\left\langle u_i^{'} u_i^{'} \right\rangle, \tag{2.15}$$

P represents shear-generated production of turbulent kinetic energy defined as

$$P = -\left\langle u_1^{'} u_2^{'} \right\rangle \frac{\partial \left\langle u_1 \right\rangle}{\partial x_2}, \tag{2.16}$$

B represents the buoyancy flux or rate of exchange between turbulent kinetic and potential energies defined as

$$B = -Ri_{b,0}\left\langle \rho^{'} u_3^{'} \right\rangle, \tag{2.17}$$

and T represents the transport of turbulent kinetic energy through turbulent motions (T_t), pressure correlations (T_p), and viscous diffusion (T_v) defined as

$$T = T_t + T_p + T_v \tag{2.18}$$

$$= \frac{1}{2}\left\langle u_i^{'} u_i^{'} u_2^{'} \right\rangle + \left\langle p^{'} u_2^{'} \right\rangle - \frac{2}{Re_0}\left\langle u_i^{'} s_{i2}^{'} \right\rangle. \tag{2.19}$$

The TKE budgets for the cases A0, A3, and 2D are presented in Figure

2.8(a),(b),(c) respectively. In the unstratified (A0) budget the production, transport, and dissipation are all significant. Away from the centerline, turbulent production and transport exceed dissipation leading to TKE generation, while at the centerline there is an approximate balance. In the stratified (A3) budget the dominant balance is between production and transport; the dissipation and buoyancy flux have smaller values. The magnitude of integrated dissipation varies considerably between stratified cases, but the relatively small influence of dissipation on the energy budget helps explain why energetics, such as $\left\langle u_1' u_1' \right\rangle$, do not vary between cases for sufficiently large Ri_b, even though dissipation does vary. Lateral transport is significantly more effective in the stratified cases than case $A0$, owing to the well organized ω_3 field associated with the coherent structures. The dominant balance of the two-dimensional (2D) budget is also between turbulent production and turbulent transport with production and transport varying very similarly to A3 with repect to x_2/δ_ω. Dissipation plays an even less significant role in the 2D budget as expected from the results in the previous section.

The buoyancy flux is a relatively small term in the energy budget at late time. Shear instabilities in the mean flow do not directly contribute to the formation of $\omega_h = \sqrt{\omega_1^2 + \omega_2^2}$, which can only be generated through secondary instabilities. Buoyancy flux is positive at the centerline, where vortical structures tend to tilt away from the vertical due to baroclinic torque, resulting in an exchange from potential to kinetic energy. The lattice of tilted vortical structures advects fluid away from their equilibrium position as ambient flow is entrained, resulting in the negative buoyancy flux away from the centerline.

While internal waves are present outside of the coherent structures in the stratified cases, their amplitudes are small and they transport little energy away from the shear layer. In case $A3$, the energy flux $\langle p' u_2' \rangle$ evolves very similarly to the internal wave free $2D$ case.

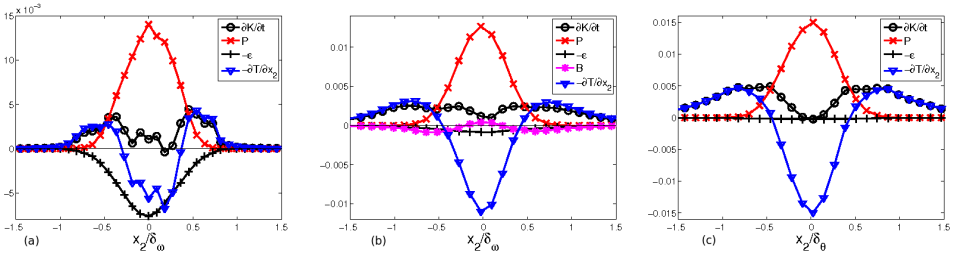

Figure 2.8: Turbulent kinetic energy budgets for (a) the unstratified case (A0) at time $t = 21.29$, (b) the strongly stratified case (A3) at time $t = 70.66$, and (c) 2D at time $t = 66.31$. The terms have been normalized with $\Delta U^3/\delta_\omega\,(t)$.

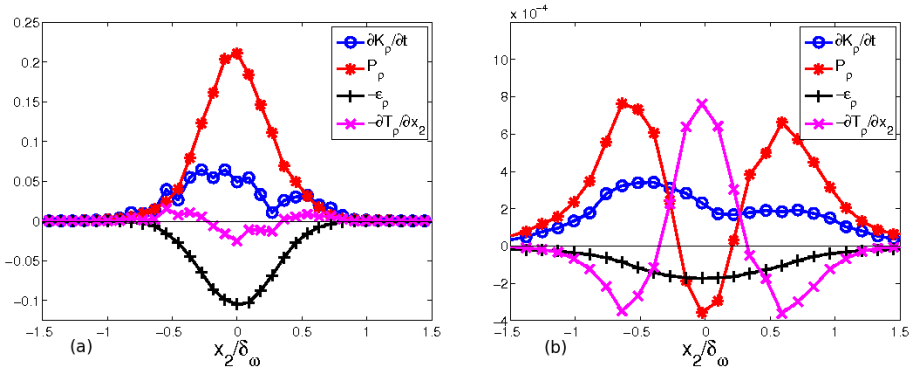

Figure 2.9: Scalar variance budgets for (a) the unstratified case (A0) at time $t = 21.29$ and (b) the strongly stratified case (A3) at time $t = 70.66$. Each term is normalized with $(d\bar{\rho}/dz)^2\Delta U\delta_\omega\,(t)$

2.6 Scalar Variance Budgets

The evolution of scalar variance is examined to understand scalar transport and mixing. The evolution equation for scalar variance is

$$\frac{\partial \left\langle \rho^{'} \rho^{'} \right\rangle}{\partial t} = P_{\rho} - \epsilon_{\rho} - \frac{\partial T_{\rho}}{\partial x_2}. \tag{2.20}$$

Since N^2 is uniform throughout the domain, turbulent potential energy, K_{ρ}, is directly proportional to scalar variance and has the following evolution equation,

$$\frac{\partial K_{\rho}}{\partial t} = \frac{Ri_b}{2} \left(P_{\rho} - \epsilon_{\rho} - \frac{\partial T_{\rho}}{\partial x_2} \right). \tag{2.21}$$

Here, P_{ρ} is the nondimensional production of scalar variance due to motion in the vertical direction defined as

$$P_{\rho} = 2 \left\langle \rho^{'} u_3^{'} \right\rangle . \tag{2.22}$$

Note that the dimensional production given by $-2 \left\langle \rho^{*'} u_3^{*'} \right\rangle d < \rho^{*} > /dx_3^{*}$ takes the above form owing to the nondimensionalization used here. The term T_{ρ} or scalar transport, which is split into turbulent scalar transport ($T_{\rho,t}$) and viscous scalar transport ($T_{\rho,v}$), is defined as

$$T_{\rho} = T_{\rho,t} + T_{\rho,v} \tag{2.23}$$

$$= \left\langle \rho^{'} \rho^{'} u_2^{'} \right\rangle - \frac{2}{Re_0 Pr} \frac{\partial \left\langle \rho^{'} \rho^{'} \right\rangle}{\partial x_2}. \tag{2.24}$$

It should be noted that for the unstratified budget we assume that the flow is actually vertically stratified, but density acts as a passive scalar since the buoyancy term is neglected for $Ri_b = 0$. This is equivalent to investigating a stratified fluid in the absence of a gravitational field.

Figure 2.9(a),(b) show distinct differences between the stratified and unstratified budgets. Greater lateral spread of profiles in the stratified cases is con-

sistent with previous results, such as the profiles in Figure 2.3. While the terms in the unstratified budget tend to subside where $|x_2| \gtrsim \frac{1}{2}\delta_\omega$, the terms from the stratified cases do not tend to zero until $|x_2| \gtrsim \delta_\omega$ indicating that shear induced scalar stirring and mixing occur over significantly larger horizontal length scales.

The distinct differences between the two budgets are also observed in the production and turbulent transport terms. In the unstratified case a relatively small down-gradient transport is present in 2.9(a), while in the stratified case larger counter-gradient transport is observed in 2.9(b). The difference in relative magnitudes of the transport terms between the budgets is a direct result of more effective lateral transport when coherent structures are present. Additionally, while density variance is produced near the centerline in the passive scalar case, one observes density variance destruction near the centerline and production outside of the vortical structures in the stratified cases.

The behavior of the production term, P_ρ in the scalar variance budget for case $A3$ can be explained as follows. The positive value of P_ρ at the flanks of the shear layer can be understood from the following argument inspired by previous investigation of a tilted columnar vortex (Meunier *et al.*, 2007). In the stratified cases, large quasi-vertical coherent structures emerge with tilt in both the streamwise and transverse directions resulting in small vertical velocities concentrated at the edges of the vortices. As flow is entrained from the ambient it tends to be displaced from its equilibrium position resulting in large positive P_ρ away from the structures. The negative value of P_ρ in the central region of the shear layer occurs because the fluid that has been stirred up at the peripheries and transported into the central region cannot be maintained out of static equilibrium by the suppressed vertical velocity. Thus P_ρ acts to transfer energy from potential to kinetic modes during the return of fluid particles to their equilibrium position.

2.7 Role of Coherent Structures

2.7.1 Identification

The method of feature extraction utilized in the current study is the λ_2 criterion, due to minimal presence of noise, clear physical interpretation, and ability to better isolate vortex cores and braid regions compared to both Q and Δ. λ_2 is considered a strong vortex identification scheme in the case of incompressible non-rotating systems (Chakraborty *et al.*, 2005; Haller, 2005). It is defined as the median eigenvalue of the symmetric tensor $(S_{ik}S_{kj} + \Omega_{ik}\Omega_{kj})$, where Ω_{ij} and S_{ij} represent the rate of strain and rate of rotation tensors defined as $S_{ij} = \frac{1}{2}(u_{i,j} + u_{j,i})$ and $\Omega_{ij} = \frac{1}{2}(u_{i,j} - u_{j,i})$.

2.7.2 Evolution of Coherent Structures

Figure 2.10 shows several snapshots of λ_2 isosurfaces to illustrate the evolution of coherent structures in the mixing layer. In Figure 2.10(a), at $t = 0$, the field is incoherent because of the initial high wavenumber fluctuations, but stratification quickly suppresses ω_h and quasi vertical structures emerge as in Figure 2.10(b). These structures experience strong vertical shear $(\partial u_2/\partial x_3)$ due to buoyancy induced instabilities such as the zigzag instabilty. The vertical shear distorts vortical structures causing them to dislocate and then separate leading to the formation of a field of dislocated vortex cores.

2.7.3 Zigzag Instability

Experiments performed by Billant & Chomaz (2000*a*) of a vertically oriented pair of counter-rotating columnar vortices in the presence of various levels of vertical stratification show the formation of the zigzag instability, which behaves differently from the elliptical instability commonly observed in the absence of stratification (Kerswell, 2002). An instability similar to the zigzag instability was also observed in the stratified simulations, e.g. case A3, shown in Figure 2.11(a). This instability plays an important role in introducing vertical variability and vertical

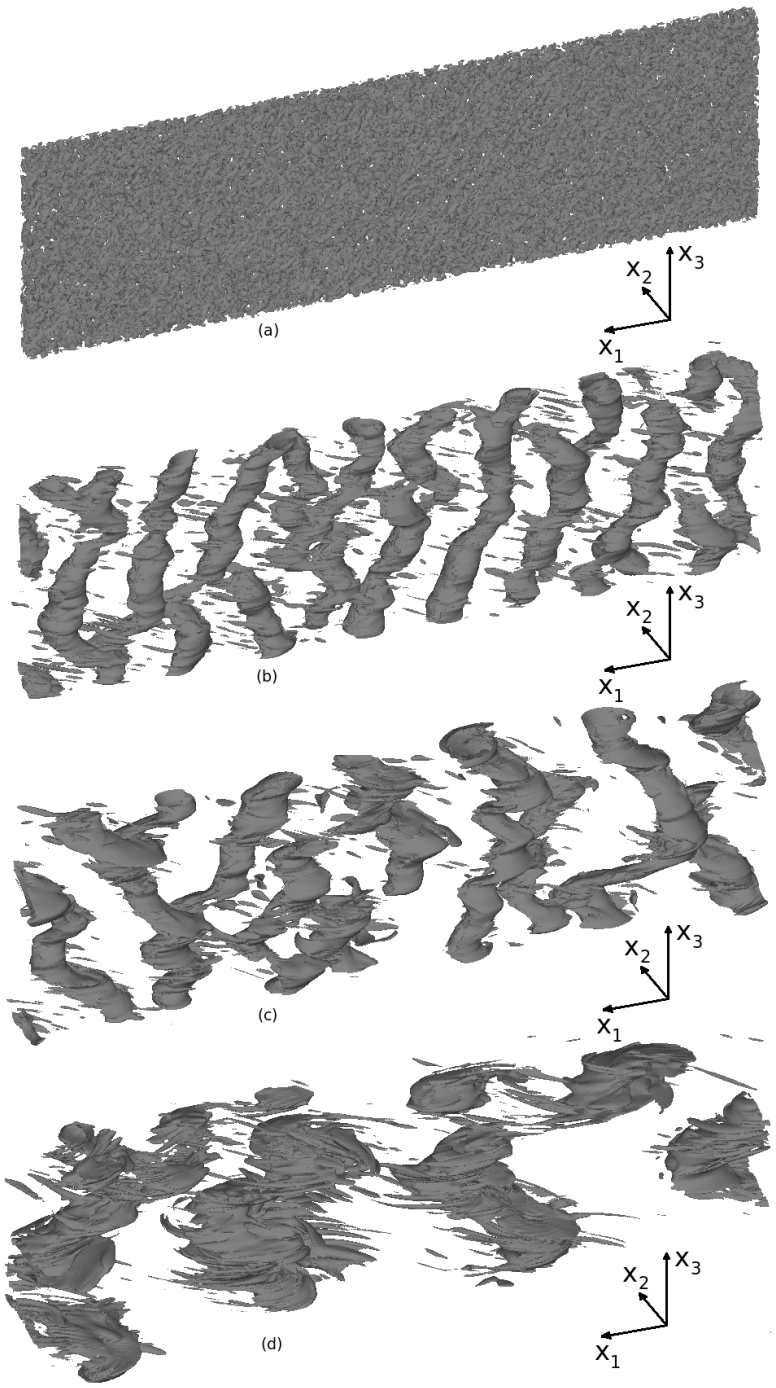

Figure 2.10: $\lambda_2 = -0.01$ isosurface contours from case A3 showing (a) initial fluctuations at $t = 0$, (b) formation of vortical structures at $t = 28.5$, (c) vertical shearing of the structures at $t = 58.4$, and finally (d) a field of vortex cores at $t = 121.6$.

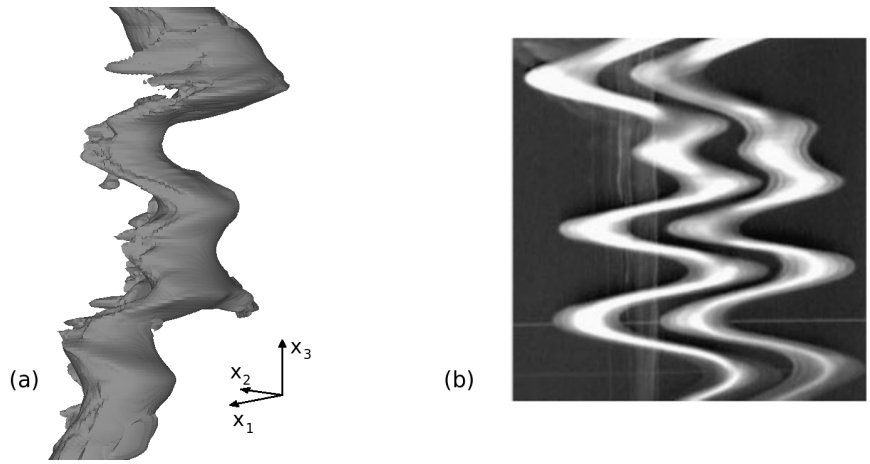

Figure 2.11: (a) Coherent structure isolated using an isocontour of $\lambda_2 = -0.01$ at $t = 58.4$ and (b) experimental observations of the zigzag instability (Billant & Chomaz, 2000*a*)

gradients into the flow field, by shearing apart columnar vortical structures.

The zigzag-like instability causes the transition of columnar vortices to pancake vortices by tilting segments of the vortices in the transverse direction. The segments of the vortices that have been displaced in the transverse direction then are advected downstream by the mean flow shearing apart the vortices until pancake vortices form. The vertical length scale associated with the instability, l_3 similarly corresponds to the length scales associated with $Fr \sim O(1)$, as in prior observations of the zigzag instability (Billant & Chomaz, 2000*a*; Waite & Smolarkiewicz, 2008).

A simulation was performed of a single quasi-vertically oriented Gaussian vortex with similar size and circulation to the vortices present in the shear layer and the coherent structures did not develop structure similar to that observed in Figure 2.11(a). This suggested that the interaction of multiple vortices plays a significant, if not necessary role in the development of the three-dimensional structures observed in the present case of horizontal, inflectional shear. Additionally, the deformation of the coherent structures is likely driven by a process similar to the zigzag instability or simply the growth of three-dimensional fluctuations with wavelength $k_3 < N/U_0$ as predicted in Deloncle *et al.* (2007) via the kine-

matic decorrelation mechanism of Lilly (1973). However, we conclude that the initial quasi-vertical orientation of the vortices alone cannot explain the evolution of coherent structures through mechanisms similar to those observed during the instability of a quasi-vertical vortex(Meunier *et al.*, 2007).

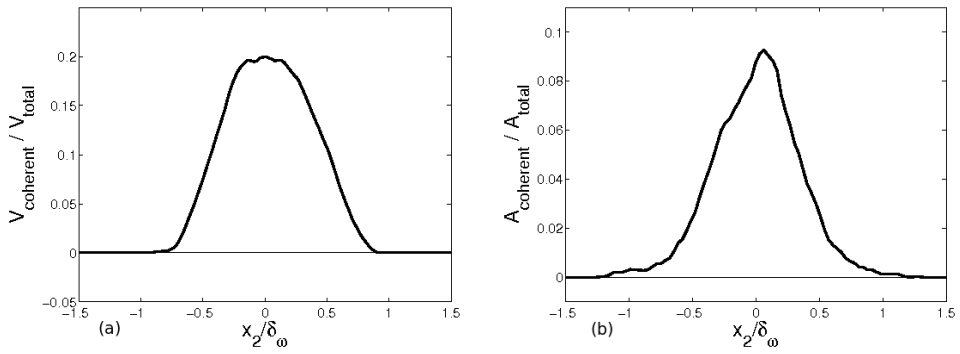

Figure 2.12: (a) Volume fraction of flow domain selected as coherent for vertical slices centered at the given values of x_2, where $\epsilon_{\text{th}} = -0.01$ and $Nt = 87.45$. (b) Area fraction of flow domain selected as coherent for slices at given values of x_2, where $t = 49.46$.

2.7.4 Statistics Conditioned on Vortical Structures

Statistics were computed on flow variables conditioned on the λ_2 criterion to determine the role of spatially sparse coherent structures in the statistical evolution of the model problem. Figure 2.12 shows the volume fraction of the coherent structures as a function of x_2, showing that structures are primarily confined in the region where $|x_2| < \delta_\omega/2$. A small negative threshold, $\epsilon_{\text{th}} = -0.01$, was chosen so that the regions of the flow field where $\lambda_2 < \epsilon_{\text{th}}$ could confidently be labeled coherent vortical structures. Case A3 was analyzed because of the high level of coherence in the vorticity field in this case, limiting the role of fine scale turbulent structure on dynamics. Figures 2.13, 2.15, and 2.16 show statistics computed on full flow fields, coherent regions where $\lambda_2 < \epsilon_{\text{th}}$, and incoherent regions where $\lambda_2 > \epsilon_{\text{th}}$.

Figure 2.13 shows the normal Reynolds stresses, $\langle u_1' u_1' \rangle$ and $\langle u_2' u_2' \rangle$, have greater magnitudes in the vortical structures than in the ambient surroundings.

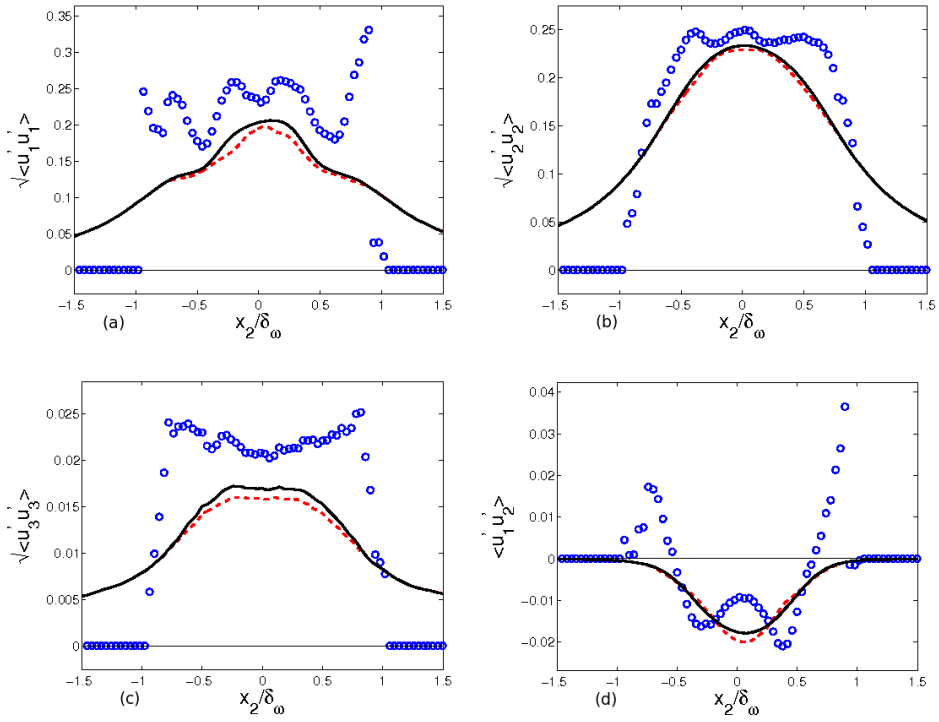

Figure 2.13: Conditioned energetics from the strongly stratified case (A3) at time $Nt = 87.45$ showing statistics conditioned on vortical structures (circles), full field statistics (solid lines), statistics for outside of vortical structures (dashed lines)

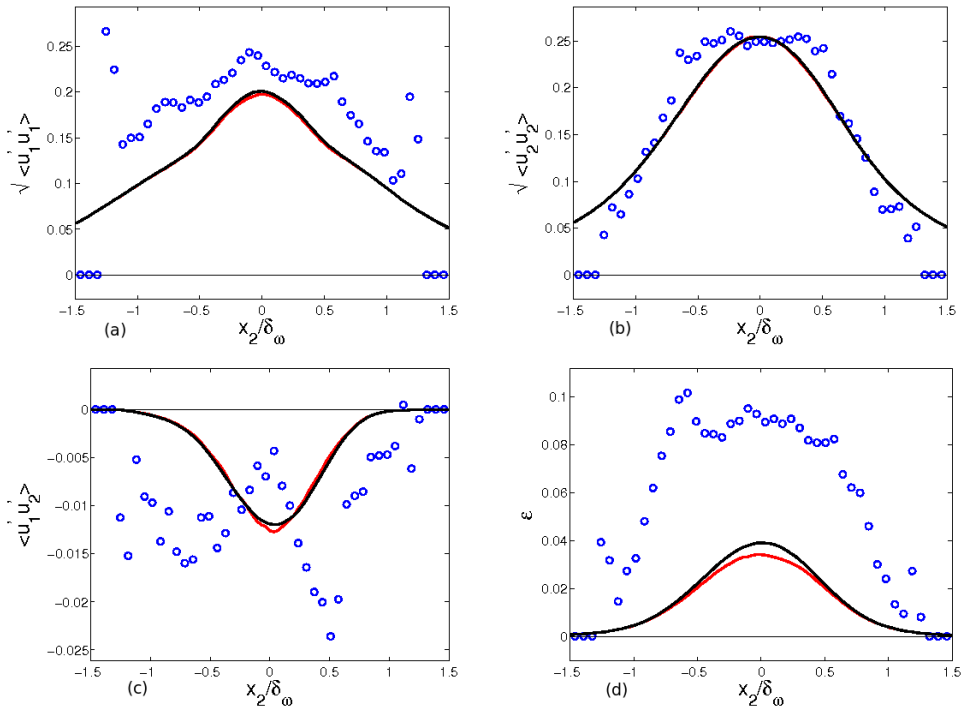

Figure 2.14: Conditioned energetics from the two dimensional case (2D) at time $t = 49.46$ showing statistics conditioned on vortical structures (circles), full field statistics (solid lines), statistics conditioned on regions outside of vortical structures (dashed lines)

$\langle u_1' u_1' \rangle$ takes large values around one vorticity thickness away from the center of the shear layer, far outside of the region containing coherent vorticity. This is due the the laterally propagating density intrusions which contain thin vortical structures in the braid region, that are captured by λ_2 as seen in 2.10(d). As the instrusions propagate away from the region of strong shear their streamwise velocity becomes relatively small compared to their surroundings giving rise to large deviations from the average velocity.

Additionally, we observe large $\langle u_3' u_3' \rangle$ inside of the vortical structures, which is due to the tilting of the segments of coherent structures away from vertical orientation via baroclinic torque. Vertical velocities were more strongly confined to the vortical structures in the small amplitude case $A3_{low}$ showing that the structures are responsible for generating vertical velocities in the shear layer. The change in sign of conditioned $\langle u_1' u_2' \rangle$, where $x_2 = \pm\delta_\omega/2$, corresponds to the regions outside of the vortex cores containing only braid structures. Figure 2.14 shows the conditioned Reynolds stresses and turbulent dissipation for the $2D$ case. Results are similar to case $A3$ with the exception of the fact that conditioned $\langle u_1' u_2' \rangle$ does not take large positive values, likely due to the fact that buoyancy does not affect the braids which tend to possess significant TPE in case $A3$.

In Figure 2.15(a), dissipation of turbulent kinetic energy is significantly larger within the vortical structures due to the large vertical gradients in the vorticity fields at dislocations which are captured by λ_2 as coherent regions of the flow field. The buoyancy flux is large within the structures, consistent with the collapse of tilting structures providing a mechanism for transfer from potential to kinetic energy near the x_2 midplane. Conditioned buoyancy flux has a similar shape to the buoyancy flux of the whole field except with a larger amplitude. This illustrates the importance of vortex dynamics to the exchange of kinetic and potential energies in this flow.

Figure 2.15(c) shows that lateral transport is large in the region outside of the coherent vortices. An approximate balance of turbulent and pressure transport is observed within the structures near the centerline. Conditioned transport strongly suggests that there is net transport of TKE into the coherent structures

from the ambient flow field, even when overall transport is directed away from the structures.

In Figure 2.16(a), conditioned $< \rho' \rho' >$ shows that density fluctuations, and hence fluctuating potential energy, gather in the vortical structures. Density variance is large inside of the vortical structures largely due to the presence of pressure minima at the center of the vortex cores which distort isopycnals vertically toward the low pressure region along the center axis of the structures. In Figure 2.16(b), greater values of scalar transport are observed in the coherent regions. Integrating the difference between the scalar transport of the full field and regions outside of the structures indicate that there is a net transfer of scalar fluctuations into the structures from the ambient flow. Figure 2.16(c) shows that scalar gradients are also concentrated within the coherent structures.

The coherent field occupies a small subset of the computational domain, roughly 2% by volume in case $A3$ at $Nt = 87.45$. Because of this, statistics conditioned on the incoherent field do not differ significantly from the statistics of the full field. Nevertheless, the vortical structures carry significant fluxes, playing an important role in the evolution of the shear layer.

In the interest of developing tractable models to describe the evolution of geophysical flows dominated by coherent vortical structures, the importance of vorticity contained within the coherent structures was quantified. Flow outside of coherent regions was assumed irrotational and velocities were computed using the Biot-Savart law. The resulting velocity field poorly matched the true field, yielding large relative errors in energetic and mean profiles.

The coherent regions contained only 16.6% of the integrated vorticity magnitude and 39.1% of the integrated enstrophy in the flow when $\epsilon_{\text{th}} = -0.01$. Relaxing the threshold by a factor of 100 increased these values to 36.4% and 60.1%, respectively. The vorticity outside of the structures is significant and dynamically important, which does not bode well for the use of simple vortex-based models in geophysical flows.

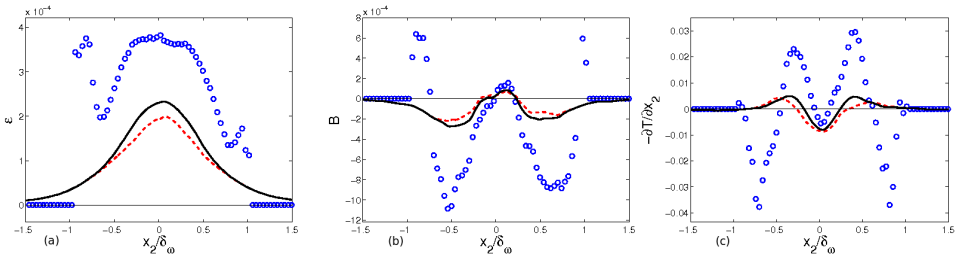

Figure 2.15: Conditioned energy budget terms from the strongly stratified case (A3) at time $Nt = 87.45$ showing statistics conditioned on vortical structures (circles), full field statistics (solid lines), statistics outside of vortical structures (dashed lines)

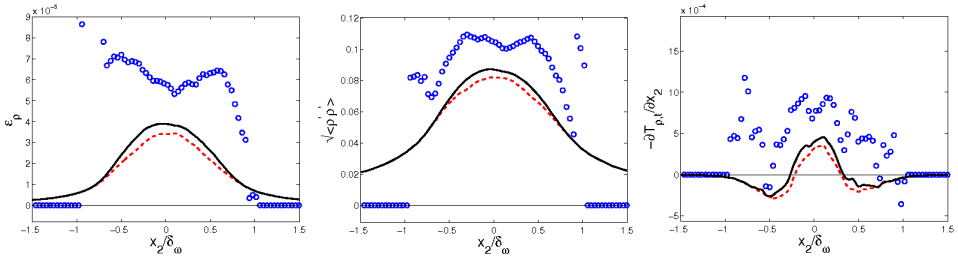

Figure 2.16: Conditioned scalar statistics from the strongly stratified case (A3) at time $Nt = 87.45$ showing statistics conditioned on vortical structures (circles), full field statistics (solid lines), statistics outside of vortical structures (dashed lines)

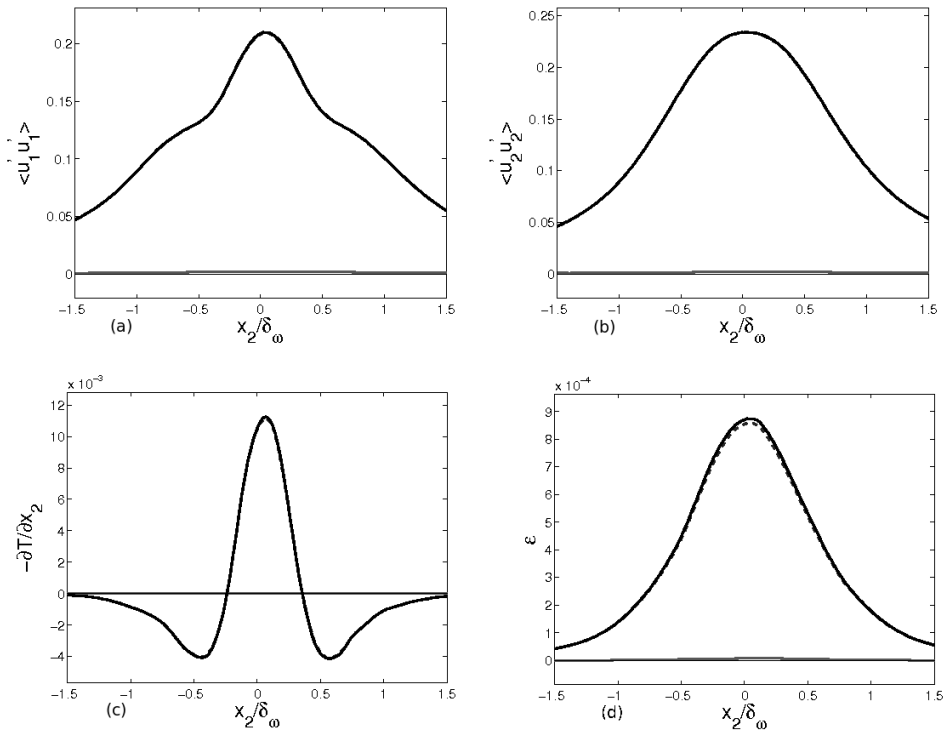

Figure 2.17: Statistics from the strongly stratified case (A3) at time $Nt = 76.76$ showing statistics corresponding to full vorticity (solid dark), coherent vorticity (dashed dark), and incoherent vorticity (solid light), where $\epsilon_D = 0.262$.

2.7.5 Wavelet Analysis

Wavelet-based feature extraction was also used to separate the vorticity field into a coherent field and random incoherent field. By coherent field, we do not imply spatially coherent vortical structures as identified by vortex eduction, but rather a denoised vorticity field. Coiflet wavelets were used with six vanishing moments. The vorticity field was decomposed into coherent and incoherent components as follows

$$\tilde{\omega}_i = \tilde{\omega}_{C,i} + \tilde{\omega}_{I,i} \ , \tag{2.25}$$

where coherent vorticity contains all wavelets with coefficients greater than the threshold ϵ_D, where $\epsilon_D = \sqrt{\frac{2}{3}\left\langle \omega_{I,i}^2 \right\rangle \ln \tilde{N}}$. Here, $\tilde{N}$ represents the number of computational points on which the wavelet transform is performed. This threshold is used in Jacobitz *et al.* (2008) and motivated by theorems related to denoising theory (Donoho & Johnstone, 1994). An iterative process is used in the computation of ϵ_D, since $\omega_{I,i}$ is dependent on ϵ_D and vice versa. Once the vorticity fields were split, velocity fields were computed by solving the Poisson equation below

$$\frac{\partial^2 u_i}{\partial x_j^2} = -\epsilon_{ijk}\frac{\partial \omega_k}{\partial x_j} \tag{2.26}$$

Figure 2.17 shows $\left\langle u_1' u_1' \right\rangle$, $\left\langle u_2' u_2' \right\rangle$, fluctuating transport, and fluctuating dissipation as computed on velocity fields corresponding to the full, coherent, and incoherent vorticity fields. The contribution of incoherent vorticity is negligible. The incoherent vorticity field induces a velocity field with fluctuations two orders of magnitude smaller than those induced by the full vorticity field, and peak turbulent transport magnitude in the incoherent field is five orders of magnitude smaller than the full field.

Prior investigations into homogeneous turbulence show that coherent vorticity is typically captured with approximately 3% of the total wavelet coefficients

(Jacobitz *et al.*, 2008; Farge *et al.*, 2001). In the inhomogeneous shear layer, a considerably smaller fraction of wavelet coefficients is needed. The fraction scales with δ_ω to reflect the effect of shear layer growth on degrees of freedom. In case $A3$ when $\delta_\omega = 5.48$, only 0.346% of wavelet coefficients is required to represent the coherent field. The fraction of coefficients deemed coherent decreases as stratification increases, with case $A0$ having an order of magnitude greater coherent coefficients than case $A3$ at comparable values of δ_ω.

Vortex eduction was performed on the coherent field in case A3 using the λ_2 criterion. The result was almost identical to that on the full field. The dissipation, including the patches with high value, was also represented accurately with the coherent field.

2.8 Conclusion

The statistical evolution of a horizontally oriented mixing layer where the mean shear, $\partial \langle u_1 \rangle / \partial x_2$, is horizontal was investigated for a range of stratifications and the role of coherent structures clarified. The statistics vary significantly between cases with different stratification. Many statistics could be collapsed between cases when times corresponding the same $Ri_b(t)$ were chosen. This dependence on $Ri_b(t)$ disappeared at late time in the strongly stratified cases where $Ri_b \gg 1$ leads to approximately self-similar evolution in some statistics such as turbulent stresses. In the self-similar state, the turbulent stresses were similar to those in two-dimensional shear layers. However, the turbulent dissipation rate was significantly larger in the stratified shear layer in comparison with the two-dimensional case. Buoyancy leads to important processes not observed in the unstratified and two-dimensional simulations such as density intrusions, tilting and collapsing vortical structures and the zigzag instability.

Stratification was found to decrease dissipation levels and increase lateral spread of turbulence leading to higher shear layer growth rates. When density behaved as an active scalar, significant counter-gradient transport of density was observed in the central region, which was fundamentally different from the passive

scalar case's co-gradient transport.

While in a vertical stratified shear layer intense vertical mixing can be accomplished during the mixing transition, which is short-lived, vertical mixing can occur in the horizontal shear layer over longer time periods. Strong vertical gradients are introduced through secondary instabilities that induce dislocations in coherent structures with vertical vorticity. The zigzag instability, shown earlier in the case of a counter-rotating vortex pair, occurs in the present problem with horizontal shear after coherent vortices emerge from the initial turbulence.

Spatially coherent vortical structures were identified using the λ_2 criterion. The influence of these vortical structures on the evolution of the mixing layer was discussed. Vortical structures play important roles in the coupling of scalar and velocity fields and contain concentrations of kinetic and potential energies. The exchange between coherent and ambient flow is significant and energy transport is primarily accomplished by the ambient flow. Irreversible losses to viscous and scalar dissipation are also concentrated within the coherent structures. However, the domain outside the identified vortex structures also contains significant vorticity. Therefore, statistics conditioned on the coherent structures do not agree with the full statistics. The importance of the ambient vorticity on statistical evolution is a surprising result of this work.

Wavelet analysis of the vorticity field shows that significant reduction in the number of degrees of freedom is possible when modeling or simulating stratified turbulence. The incoherent vorticity field is found to have negligible effect on the statistics and the coherent vortical structures, even though it contains well over 99% of the wavelet modes. The incoherent field plays a less significant role in the stratified cases then in the unstratified case.

The contents of this chapter are published in the *Physics of Fluids Journal*. E. Arobone and S. Sarkar. "The statistical evolution of a stratified mixing layer with horizontal shear invoking feature extraction", Phys. Fluids, 22, 115108, 2010. The authors are pleased to acknowledge partial support by the Jacobs School Graduate Fellowship (for E.A.) and the National Science Foundation CDI program through grant OCE-0835839 (for S.S. and E.A.).

Chapter 3

Linear Evolution of a Stratified Rotating Shear Layer with Horizontal Shear

3.1 Introduction

The effects of strong stratification, where $Fr_h = S/N \lesssim O(1)$, and moderate rotation rates, where $|Ro| = S/2|\Omega| \sim O(1)$, on shear flow is important for basic understanding of submesoscale ocean dynamics. We concentrate our study on a horizontally oriented hyperbolic tangent mixing layer including stratification and rotation effects. Isolated horizontal shear is prevalent in boundary currents and in the wake of isolated topography. Previous work has explored the three-dimensional linear stability of a horizontally oriented shear layer subjected to rotation or stratification alone, but not in combination. Figure 3.1 gives a schematic illustrating the rotating stratified horizontal shear layer and relevant parameters.

Deloncle *et al.* (2007) explored the influence of uniform stable stratification on the linear stability of a non-rotating horizontal hyperbolic tangent mixing layer with shear concentrated in a region with characteristic length scale L. When stratification was strong, with $Fr_h \lesssim 1$, self-similarity of growth rates with respect to vertical wavenumber was realized with associated scale $Fr_h k_3 L$, as opposed

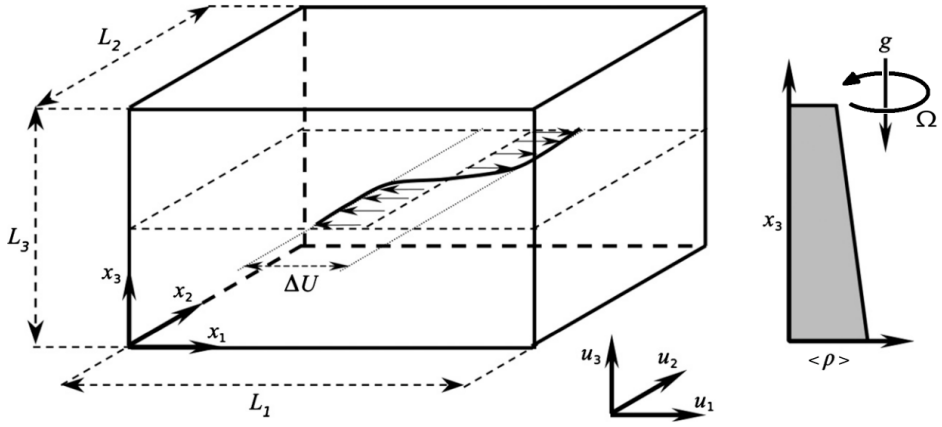

Figure 3.1: Schematic of the rotating stratified horizontal shear layer. Relevant parameters include the vorticity thickness, δ_ω, kinematic viscosity ν, mass diffusivity κ, and reference density ρ_0.

to the unstratified $k_3 L$ scale. This result is consistent with the self-similarity of strongly stratified flows proposed by Billant & Chomaz (2001) and implies that a wider range of vertical wavenumbers are unstable when stratification is strong.

Johnson (1963) explored the effects of vertical shear, $U_1(x_3)$, subjected to coordinate system rotation about an axis oriented at an arbitrary angle, θ, with respect to the streamwise direction. Neutral modes were computed for a hyperbolic tangent mean velocity profile for various values of θ. A horizontally oriented shear layer subjected to vertical rotation without stratification is equivalent to the $\theta = \pm 90^\circ$ cases investigated in Johnson (1963). Rotation was found to stabilize the flow, except for the anticyclonic case with $0 < 2\Omega < dU_1/dx_3$ where the effect of rotation was destabilizing. This result is consistent with the Rayleigh criterion for inertial instability, which states that $2\Omega(2\Omega + \omega_3) < 0$ implies instability. Here, ω_3 is the relative vertical vorticity and $2\Omega + \omega_3$ is the corresponding absolute vertical vorticity.

The stability of a viscous hyperbolic tangent mixing layer subjected to rigid-body rotation perpendicular to the plane of the mean flow was explored by Yanase *et al.* (1993). Two distinct instability regimes were observed. The first region corresponded to the barotropic (or Kelvin-Helmholtz) instability with its growth rate peaking when $k_1 = 0.43$ and $k_3 = 0$. The second region corresponded to the

inertial (or shear/Coriolis) instability with its growth rate peaking when $k_1 = 0$ and k_3 is large in comparison with barotropic modes. The neutral curves found in Johnson (1963) were determined to be incorrect and did not capture the inertial instability regime properly.

Smyth & Peltier (1994) explored the evolution of a rotating and unstratified barotropic shear layer and the stability of the temporally evolving two-dimensional flow with respect to three-dimensional perturbations. The evolution included Kelvin-Helmholtz vortex formation and pairing. Slow rotation rates either stabilized or destabilized the barotropic vortices depending on the sign of f, while rapid rotation stabilized the flow. When the absolute vorticity was small in comparison to the relative vorticity, the vortex core was destabilized. Later, Smyth & McWilliams (1998) explored the instability of a single columnar vortex in a rotating and stratified fluid. In the case of rapid rotation and strong stratification, instability was restricted to a band of vertical wavenumbers such that $k_3 L \sim |N/f|$, consistent with quasi-geostrophy. A surprising result was that this scaling was realized outside of the formal quasi-geostrophic regime, when coordinate system rotation rates were only a few times faster than vortex core rotation rates. Inertial instability was realized for moderate anticyclonic rotation rates.

Numerical simulations of the inertial instability for various wall-bounded and free-shear flows were explored by Kloosterziel *et al.* (2007*b*). Simulations were invariant in the stream-wise direction, so that the barotropic instability would not influence evolution. It was observed that the inertial instability redistributes linear momentum in a manner that yields a final state that is inertially stable, suppressing regions of negative potential vorticity.

Plougonven & Zeitlin (2009) investigated the development of inertial instability for a hyperbolic tangent mixing layer in a rotating stratified fluid. The barotropic instability was ignored by exploring modes that were invariant in the streamwise direction. Analytical solutions for the linear stability of the problem were derived in addition to exploration of nonlinear evolution of inertial instability and the fluctuating baroclinicity of the final state. An analytical expression was derived for growth rate showing that growth rate tends towards maximal values

when $k_3 \to \infty$ for inviscid flow. The expression also allowed for easy computation of the most unstable vertical wavenumber for inertially unstable viscous flows.

The three dimensional stability of a Kármán vortex sheet, symmetric double row, and single row of vortices was explored in a stratified and rotating fluid by Deloncle *et al.* (2011). For the non-rotating stratified Kármán vortex sheet, zigzag-type instabilities were realized for sufficiently close vortex rows. When rotational effects were included, cyclonic vortices were found have less bend than anticyclonic vortices. In the rapid rotation regime, growth rates were found scale like $Ro/(bFr_h)$ where b denotes spacing between adjacent vortices in the same row. The result is consistent with quasi-geostrophic scaling laws.

In this chapter, the stability of the horizontal mixing layer will be explored with the influence of both stratification and rotation for fully three-dimensional perturbations. Section 3.2 will formulate the eigenvalue problem. Section 3.3 will introduce theory related to horizontal vorticity fluctuations to aid in explaining the stability of the shear layer. Section 3.4 will explore the effects of stratification and rotation on eigenvalues to infer various asymptotic regimes of the flow. Lastly, section 3.5 will explore the effects of stratification and rotation on eigenmodes and their underlying vortex dynamics with a focus on buoyancy effects.

3.2 Formulation of Modal Stability Problem

The governing equations for Boussinesq incompressible flow in a rotating coordinate system are given here with dimensional quantities denoted by superscript * :

$$\frac{\partial u_i^*}{\partial t^*} + u_j^* \frac{\partial u_i^*}{\partial x_j^*} + \epsilon_{i3k} 2\Omega^* u_k^* = -\frac{1}{\rho_0^*}\frac{\partial p^*}{\partial x_i^*} - \frac{\rho^* g^*}{\rho_0^*}\delta_{i3} + \nu^* \frac{\partial^2 u_i^*}{\partial x_j^* \partial x_j^*}, \tag{3.1}$$

$$\frac{\partial u_i^*}{\partial x_i^*} = 0, \tag{3.2}$$

$$\frac{\partial \rho^*}{\partial t^*} + u_j^* \frac{\partial \rho^*}{\partial x_j^*} = \kappa^* \frac{\partial^2 \rho^*}{\partial x_j^* \partial x_j^*}. \tag{3.3}$$

The base state of interest is a hyperbolic tangent mixing layer of the form

$$\langle u_1^* \rangle = \frac{\Delta U^*}{2} \tanh\left(\frac{2x_2^*}{\delta_\omega^*}\right),$$

with linear vertical stratification $d\langle\rho^*\rangle/dx_3^*$, Coriolis parameter $f^* = 2\Omega^*$, vorticity thickness δ_ω^*, and velocity difference ΔU^* as seen in Figure 3.1. The mean pressure field is chosen to exactly balance the effects of the mean Coriolis terms and the mean buoyancy term from the momentum equations. The non-dimensional governing equations and associated non-dimensional parameters are as follows :

$$\frac{\partial u_i}{\partial t} + u_j \frac{\partial u_i}{\partial x_j} + \epsilon_{i3k} 2\Omega u_k = -\frac{\partial p}{\partial x_i} - Ri_b \rho \delta_{i3} + \frac{1}{Re}\frac{\partial^2 u_i}{\partial x_j \partial x_j}, \quad (3.4)$$

$$\frac{\partial u_i}{\partial x_i} = 0, \quad (3.5)$$

$$\frac{\partial \rho}{\partial t} + u_j \frac{\partial \rho}{\partial x_j} = \frac{1}{RePr}\frac{\partial^2 \rho}{\partial x_j \partial x_j}, \quad (3.6)$$

$$Ri_b = -\frac{g^*}{\rho_0^*}\frac{d\langle\rho^*\rangle}{dx_3^*}\frac{\delta_\omega^{*2}}{\Delta U^{*2}} = \frac{N^{*2}\delta_\omega^{*2}}{\Delta U^{*2}} = Fr_h^{-2}, \quad 2\Omega = Ro^{-1} = \frac{f^*\delta_\omega^*}{\Delta U^*}, \quad (3.7)$$

$$Re = \frac{\Delta U^* \delta_\omega^*}{\nu^*}, \quad Pr = \frac{\nu^*}{\kappa^*}. \quad (3.8)$$

Next, linearized evolution equations are derived for small amplitude perturbations and given here :

$$\frac{\partial u_i'}{\partial t} + \langle u_1 \rangle \frac{\partial u_i'}{\partial x_1} + u_2' \frac{d\langle u_i \rangle}{dx_2}\delta_{i1} + \epsilon_{i3k} 2\Omega u_k' = -\frac{\partial p'}{\partial x_i} - Ri_b \rho' \delta_{i3} + \frac{1}{Re}\frac{\partial^2 u_i'}{\partial x_j \partial x_j}, \quad (3.9)$$

$$\frac{\partial u_i'}{\partial x_i} = 0, \quad (3.10)$$

$$\frac{\partial \rho'}{\partial t} + \langle u_1 \rangle \frac{\partial \rho'}{\partial x_1} - u_3' = \frac{1}{RePr}\frac{\partial^2 \rho'}{\partial x_j \partial x_j}. \quad (3.11)$$

Solutions are assumed to be wavelike in the streamwise and vertical directions with the following functional form :

$$[u_i', p', \rho'](x_2) \exp(ik_1 x_1 + ik_3 x_3 + \sigma t).$$

Substituting into the linearized equations of motion and combining equations in a manner similar to Deloncle *et al.* (2007), we obtain a generalized eigenvalue problem of the form :

$$\boldsymbol{A} \begin{pmatrix} u_1' \\ u_2' \\ \rho' \end{pmatrix} = \sigma \boldsymbol{B} \begin{pmatrix} u_1' \\ u_2' \\ \rho' \end{pmatrix}.$$

The matrices $\boldsymbol{A}$ and $\boldsymbol{B}$ are shown below where $k^2 = k_1^2 + k_3^2$, $D = d/dx_2$, $\Delta = D^2 - k^2$, $U = \langle u_1 \rangle$, $\omega_a = -DU + 2\Omega$, $\nu = Re^{-1}$, and $\kappa = (RePr)^{-1}$ are used for compactness

$$A = \begin{bmatrix} -2\Omega k^2 & ik_1(U\Delta + D\omega_a) + \nu\Delta & -ik_3 Ri_b D \\ ik_1(UD - \omega_a) - \nu\Delta D & (D^2 + k_1^2)U - \omega_a D + \nu i k_1 \Delta & 0 \\ -ik_1 & -D & k_1 k_3 U + \kappa i k_3 \Delta \end{bmatrix}$$

$$B = \begin{bmatrix} 0 & k^2 - D^2 & 0 \\ -D & ik_1 & 0 \\ 0 & 0 & ik_3 \end{bmatrix}$$

Matrices $\boldsymbol{A}$ and $\boldsymbol{B}$ are discretized using rational Chebyshev basis functions. The generalized eigenvalue problem is solved using the Intel MKL library and Fortran. Since k_3 appears in the equations only as k_3^2 or $k_3\rho'$ (which can be absorbed by definition into a new variable $k_3\rho'$) it is clear that the sign of k_3 does not affect growth rate, σ. On the other hand, examining $\det(A - \sigma B) = 0$ shows that changing the sign of k_1 changes the sign of σ. Also, Johnson (1963) established

that unstable modes cannot exist for $|k_1| > 1$. These points imply that we may study the stability of the flow field in the domain of $k_1 \in [0,1]$ and $k_3 \in [0,\infty)$ without a loss of generality.

3.3 Evolution of Horizontal Vorticity Fluctuations

The linearized inviscid fluctuating vorticity equations for the given base flow are as follows :

$$\begin{aligned}\frac{\bar{D}\omega_i'}{\bar{D}t} &= -u_2'\frac{\partial\langle\omega_i\rangle}{\partial x_2}\delta_{i3} + \left(\omega_2'\delta_{i1} + \omega_1'\delta_{i2}\right)\langle s_{12}\rangle + \left(\langle\omega_3\rangle + 2\Omega\right)s_{i3}' \\ &\quad +\epsilon_{ik3}\Omega\omega_k' - Ri_b\epsilon_{ij3}\frac{\partial\rho'}{\partial x_j}. \end{aligned} \tag{3.12}$$

The behavior of the inertial instability in either a strongly stratified or a homogeneous fluid can be explained by looking at the inviscid linearized evolution equations for the horizontal fluctuating vorticity components. They are given below, letting $S(x_2)$ denote local mean shear, and noting that $\langle\omega_3\rangle(x_2) = -S(x_2)$:

$$\frac{\bar{D}\omega_1'}{\bar{D}t} = \frac{\omega_2'}{2}\left(S(x_2) + 2\Omega\right) + \left(2\Omega - S(x_2)\right)s_{13}' - Ri_b\frac{\partial\rho'}{\partial x_2} \tag{3.13}$$

$$\frac{\bar{D}\omega_2'}{\bar{D}t} = \frac{\omega_1'}{2}\left(S(x_2) - 2\Omega\right) + \left(2\Omega - S(x_2)\right)s_{23}' + Ri_b\frac{\partial\rho'}{\partial x_1} \tag{3.14}$$

The first term on the right hand side of both equations above physically represents the tilting of vorticity fluctuations by the mean velocity gradient combined with the 'fictitious' effect of coordinate system rotation on horizontal vorticity components. The second term in both equations represents the tilting of mean flow absolute vorticity by strain fluctuations. The third term represents vorticity generation via baroclinic torque. The right hand side can also be expressed in a

more mathematically convenient form in terms of fluctuating velocity gradients.

$$\frac{\bar{D}\omega_1'}{\bar{D}t} = -S(x_2)\frac{\partial u_3'}{\partial x_1} + 2\Omega\frac{\partial u_1'}{\partial x_3} - Ri_b\frac{\partial \rho'}{\partial x_2} \tag{3.15}$$

$$\frac{\bar{D}\omega_2'}{\bar{D}t} = (2\Omega - S(x_2))\frac{\partial u_2'}{\partial x_3} + Ri_b\frac{\partial \rho'}{\partial x_1} \tag{3.16}$$

For small k_1 (relative to k_3) or nearly streamwise invariant modes we can simplify these equations :

$$\frac{\bar{D}\omega_1'}{\bar{D}t} \approx 2\Omega\omega_2' - Ri_b\frac{\partial \rho'}{\partial x_2}, \tag{3.17}$$

$$\frac{\bar{D}\omega_2'}{\bar{D}t} \approx -(2\Omega - S(x_2))\omega_1' + Ri_b\frac{\partial \rho'}{\partial x_1}. \tag{3.18}$$

Taking the material derivative of both sides gives :

$$\frac{\bar{D}^2\omega_1'}{\bar{D}t^2} \approx 2\Omega\frac{\bar{D}\omega_2'}{\bar{D}t} - Ri_b\frac{\bar{D}}{\bar{D}t}\left[\frac{\partial \rho'}{\partial x_2}\right], \tag{3.19}$$

$$\frac{\bar{D}^2\omega_2'}{\bar{D}t^2} \approx -(2\Omega - S(x_2))\frac{\bar{D}\omega_1'}{\bar{D}t} + Ri_b\frac{\bar{D}}{\bar{D}t}\left[\frac{\partial \rho'}{\partial x_1}\right]. \tag{3.20}$$

Substituting the linearized evolution equations for horizontal density gradient and vorticity we find :

$$\frac{\bar{D}^2\omega_1'}{\bar{D}t^2} \approx -2\Omega(2\Omega - S(x_2))\omega_1' + Ri_b(2\Omega + S(x_2))\frac{\partial \rho'}{\partial x_1} - Ri_b\frac{\partial u_3'}{\partial x_2}, \tag{3.21}$$

$$\frac{\bar{D}^2\omega_2'}{\bar{D}t^2} \approx -2\Omega(2\Omega - S(x_2))\omega_2' + Ri_b(2\Omega - S(x_2))\frac{\partial \rho'}{\partial x_2} + Ri_b\frac{\partial u_3'}{\partial x_1}. \tag{3.22}$$

The first terms on the right hand sides of equations (3.21) and (3.22) represent the inertial instability and give its maximal growth rate $\sigma = [-2\Omega(2\Omega - S)]^{1/2}$. The remaining terms correspond to buoyancy effects. In particular, the second terms represent the shearing and rotation of vorticity induced by density gradi-

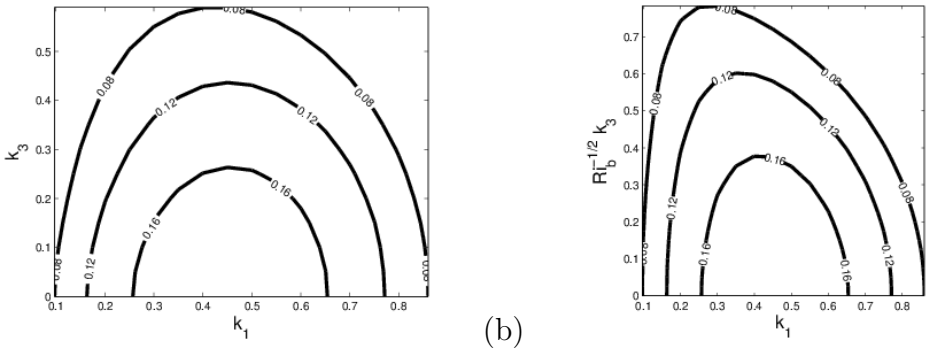

Figure 3.2: Plots of growth rate for the inviscid non-rotating homogeneous case (a) and non-rotating strongly stratified case where $Ri_b = 4$ (b).

ents, and the third term represents the influence of isopycnal deformation.

3.4 Effect of Stratification on Growth Rates

The following analysis is inviscid. The effects of viscosity and diffusion are included for reference in appendices A and B. Growth rates for a strongly stratified non-rotating shear layer are shown in Figure 3.2 (b) and agree well with figure 3 (b) of Deloncle *et al.* (2007) and their result that $Ri_b^{-1/2} k_3 = Fr_h k_3$ is the appropriate vertical self-similar scaling. The growth rates for the homogenous case are included in Figure 3.2 (a) for comparison. Weakly stratified cases, where $Ri_b < O(1)$, are found to be qualitatively similar to the unstratified cases as in Deloncle *et al.* (2007) and will not be discussed.

3.4.1 Moderate Rotation Regime

Plots (b) and (c) from Figure 3.3 show the effect of stratification on growth rates when $2\Omega = 0.1$. These plots suggest that for $Ri_b \gtrsim 1$, self-similarity of the form $\sigma(k_1, k_3, Ri_b, 2\Omega) = \sigma\left(k_1, Ri_b^{-1/2} k_3, 2\Omega\right)$ is observed. This result is consistent with the analysis of Billant & Chomaz (2001), which states that self-similarity of strongly stratified flows holds in a rotating coordinate system. Similar collapse when $Ri_b > 1$ was observed at all other values of 2Ω explored in this analysis.

In Figure 3.3, the inertial instability corresponds to the growth rates near

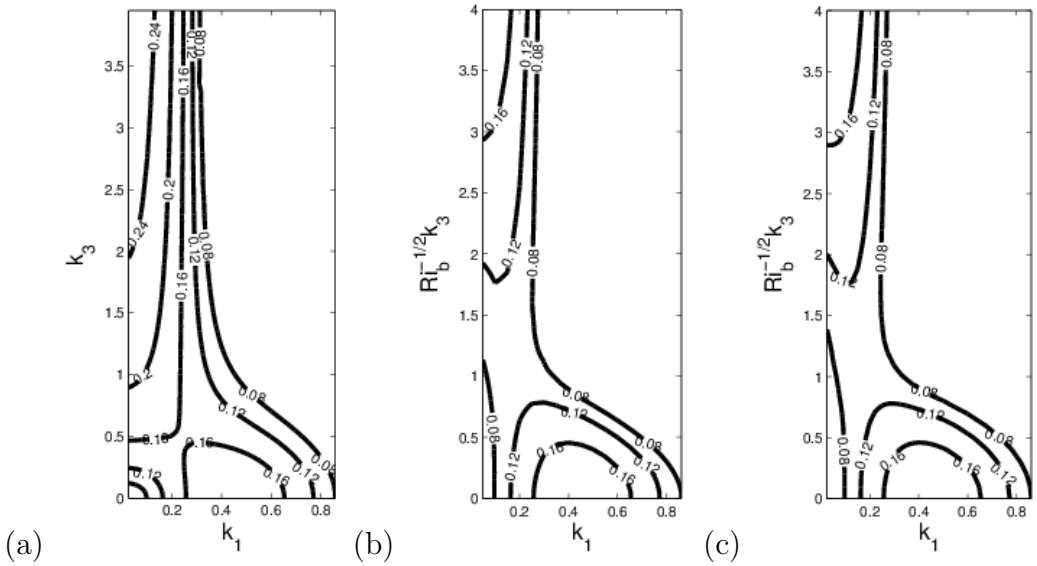

(a) (b) (c)

Figure 3.3: Contour plots of growth rate for the $Ri_b = 0$, $2\Omega = .1$ case (a), the $Ri_b = 1$, $2\Omega = .1$ case (b), and the $Ri_b = 10$, $2\Omega = .1$ case (c).

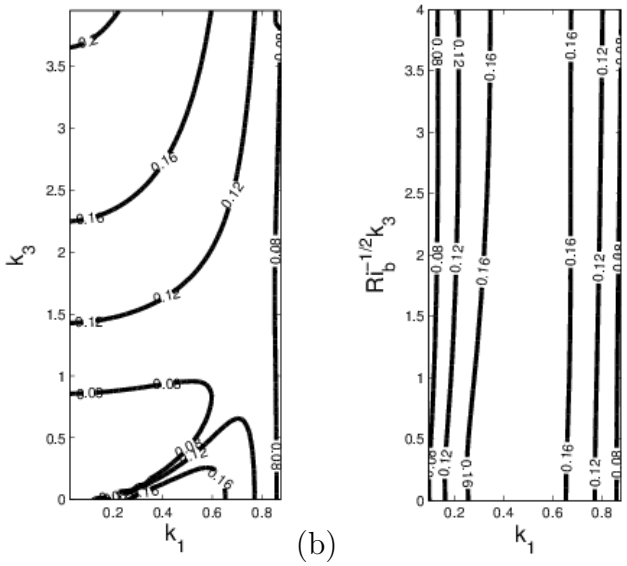

(a) (b)

Figure 3.4: Contour plots of growth rate for the $Ri_b = 0$, $2\Omega = .9$ case (a), and the $Ri_b = 10$, $2\Omega = .9$ case (b).

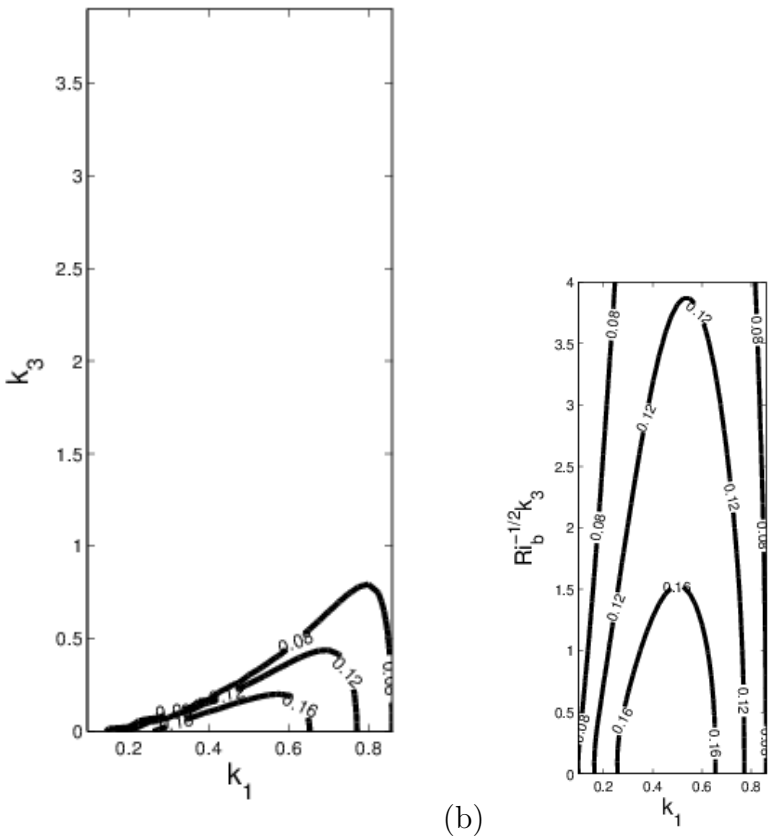

(a) (b)

Figure 3.5: Contour plots of growth rate for the $Ri_b = 0$, $2\Omega = 1$ case (a), and the $Ri_b = 10$, $2\Omega = 1$ case (b).

the k_3 axis, but away from the k_1 axis. In the limit of $k_3 \to \infty$, growth rates approach the maximal inertial growth rate of $\sqrt{-2\Omega\,(2\Omega - 1)} = 0.3$. Stratification reduces the intensity of growth rates associated with the inertial instability for moderate values of $Ri_b^{-1/2}k_3$. In the limit of $k_3 \to \infty$, the cases with and without stratification are equivalent, but this limit is not realized until very large values of $Ri_b^{-1/2}k_3$, where the influence of stratification becomes negligible. Figures 3.4 (a) and (b) show growth rates for unstratified and strongly stratified cases, respectively, with stronger anticyclonic rotation ($2\Omega = 0.9$). In the unstratified case there are distinct regions corresponding to the inertial and barotropic instabilities. In the stratified case this distinction is far less apparent, with growth rates showing little variation with respect to $Ri_b^{-1/2}k_3$.

Stratification leads to a strong qualitative change in the zero absolute vorticity case ($2\Omega = 1$), a key result of this chapter. Figures 3.5 (a) and (b) show the growth rates associated with unstratified and strongly stratified flow, respectively, for $2\Omega = 1$. The zero absolute vorticity state tends to stabilize the unstratified case, which can be seen through comparison of figures 3.2 (a) and 3.5 (a). The inertial instability also disappears when $2\Omega = 1$. Even though the inertial instability is suppressed in the stratified case too as shown by Figure 3.5(b), rotation is destabilizing in the sense that a far greater range of vertical wavenumbers is unstable than when there is no rotation. In the strongly stratified case, some modes remain unstable even when $Ri_b^{-1/2}k_3 \approx 20$.

Looking at figures 3.3, 3.4, and 3.5 we see that increasing anticyclonic rotation rates toward the zero absolute vorticity state increases the range of k_1 values associated with inertial instability for both unstratified and strongly stratified cases. In the strongly stratified cases, near the zero absolute vorticity state, the barotropic instability is greatly modified. The distinction between growth rates associated with intertial and barotropic modes are much less apparent for strongly stratified flow.

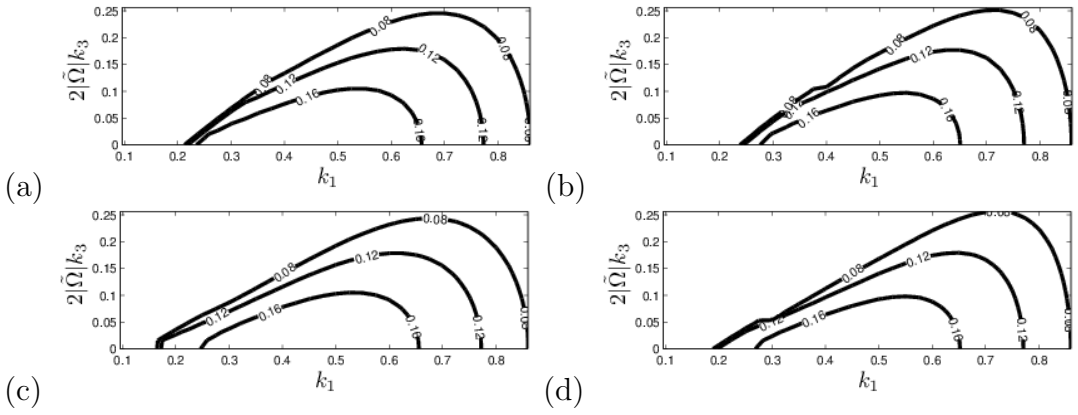

Figure 3.6: Contour plots of growth rate for the $Ri_b = 0$, $2\Omega = -4$ case (a), the $Ri_b = 0$, $2\Omega = 5$ case (b), the $Ri_b = 0$, $2\Omega = -2$ case (c), and the $Ri_b = 0$, $2\Omega = 3$ case (d).

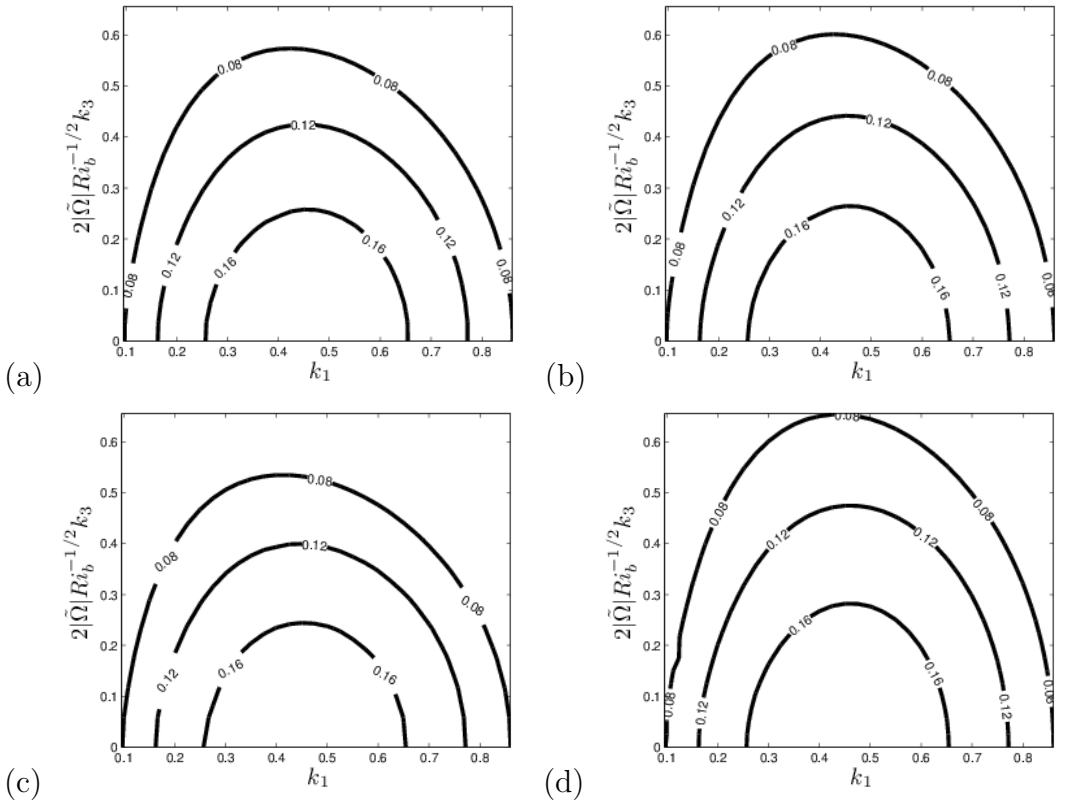

Figure 3.7: Contour plots of growth rate for the $Ri_b = 10$, $2\Omega = -14$ case (a), the $Ri_b = 10$, $2\Omega = 15$ case (b), the $Ri_b = 10$, $2\Omega = -3$ case (c), and the $Ri_b = 10$, $2\Omega = 4$ case (d).

3.4.2 Rapid Rotation Regime

Plots (a) - (d) in Figure 3.6 show growth rates for various rapid rotation rates. Figures 3.6 (a) and (b) show well-collapsed growth rates with respect to vertical scale $2|\tilde{\Omega}|k_3 = 2|(\Omega - 1/4)|k_3$ when rotation rates are $2\Omega = -4$ and $2\Omega = 5$ respectively. While slight differences are seen in figures 3.6 (c) and (d) at slower rotation rates, collapse is still reasonably good. Scaling was found to be better when vertical wavenumbers were scaled using $2|\tilde{\Omega}|$ instead of $2|\Omega|$. This scaling is the difference in angular velocity with respect to $\Omega = 1/4$, which is the most destabilizing rotation rate as seen in equations (3.21) and (3.22) for $S = 1$. Plots (a) - (d) in Figure 3.7 show similar collapse for strongly stratified flow, although not realized until higher rotation rates than in the unstratified cases. It is worth noting the associated vertical scale, $2|\tilde{\Omega}|Ri_b^{-1/2}k_3 \sim (f/N)\,k_3$, which agrees with the results of Smyth & McWilliams (1998) when $\tilde{\Omega}$ is large. Some asymmetry with respect to the sign of $\tilde{\Omega}$ is observed for the cyclonic case (c) and anticyclonic case (d) from Figure 3.7. As the rapidly rotating regime is approached, the anticyclonic case has a wider range of unstable vertical wavenumbers than the cyclonic case with equivalent $|\tilde{\Omega}|$. As in Smyth & McWilliams (1998), we find that rotation rates do not have to be very rapid to be well approximated by the rapidly rotating strongly stratified regime. Rapid rotation leads to equations (3.21) and (3.22) taking the following form for small k_1 modes :

$$\frac{\bar{D}^2\omega_1'}{\bar{D}t^2} \approx -4\Omega^2\omega_1' + Ri_b 2\Omega\frac{\partial\rho'}{\partial x_1} - Ri_b\frac{\partial u_3'}{\partial x_2}, \tag{3.23}$$

$$\frac{\bar{D}^2\omega_2'}{\bar{D}t^2} \approx -4\Omega^2\omega_2' + Ri_b 2\Omega\frac{\partial\rho'}{\partial x_2} + Ri_b\frac{\partial u_3'}{\partial x_1}. \tag{3.24}$$

Equations (3.23) and (3.24) imply that when stratification is negligible, horizontal vorticity is attenuated and, correspondingly, Figure 3.6 shows that strong stabilization is observed for modes with $k_1 \lesssim 2|\tilde{\Omega}|k_3$ for a rapidly rotating homogeneous fluid. No such effect is observed in the presence of strong stratification as seen in Figure 3.7 implying that the second and/or third terms in equations (3.23) and (3.24) offset the strongly stabilizing effect of the first term.

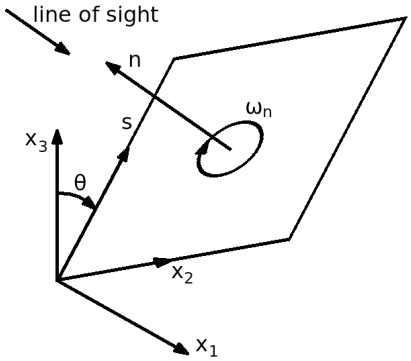

Figure 3.8: The phase variable s. Planes are displayed in a manner such that the normal vector has a positive vertical component so that visualization is more straightforward.

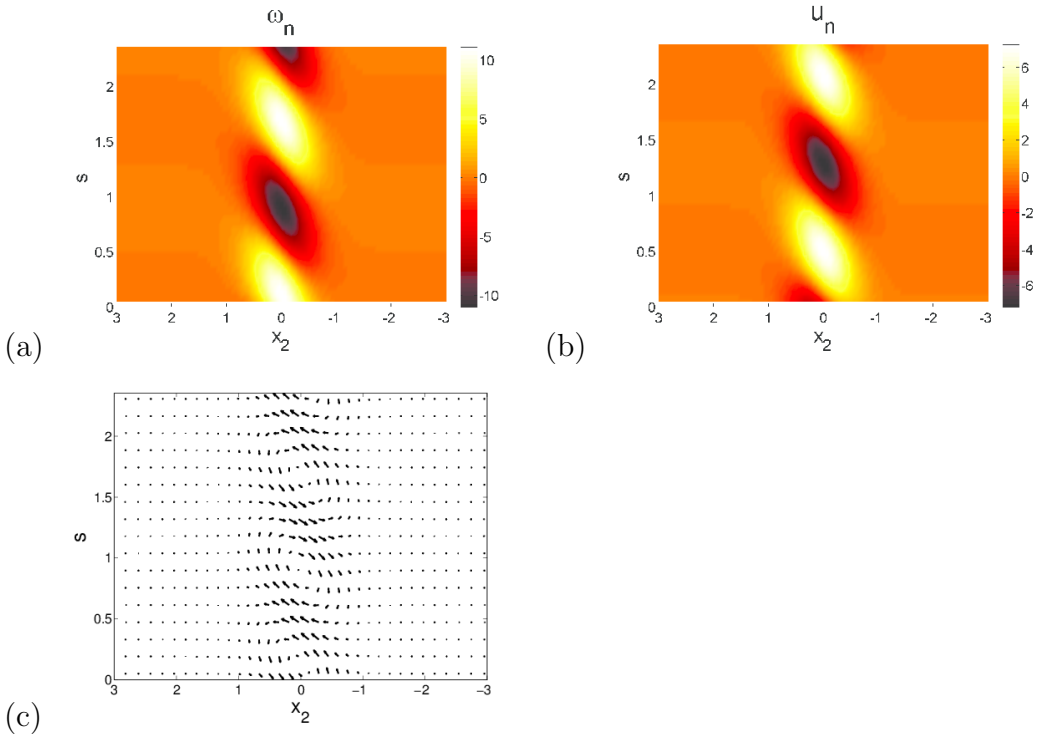

Figure 3.9: Plots of ω_n' (a), u_n' (b), and velocity vectors (c) for an inertial mode in a weak anticyclonic case without stratification, $Ri_b = 0$, $2\Omega = 0.1$, $k_1 = 0.1$, $k_3 = 4$, and $\theta = 1.43°$.

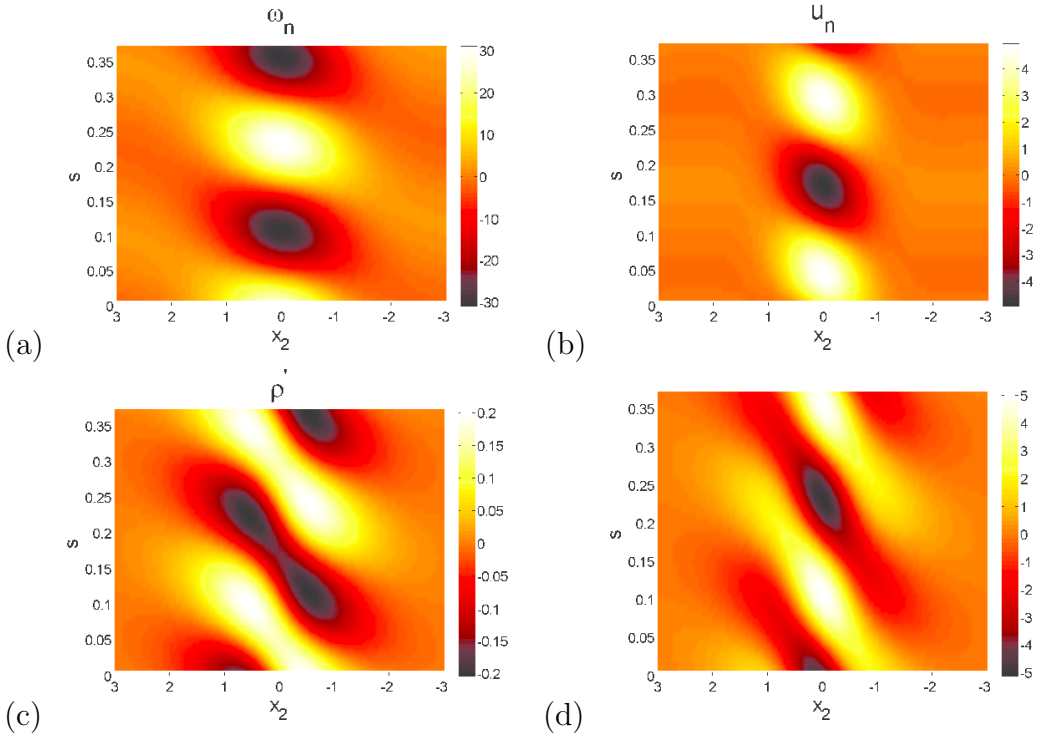

Figure 3.10: Plots of ω_n' (a), u_n' (b), ρ' (c), and the normal component of the baroclinic term from equation 3.12 (d) for an inertial mode in a weak anticyclonic case with stratification, $Ri_b = 10$, $2\Omega = 0.1$, $k_1 = 0.1$, $k_3 = 25.3$, and $\theta = 0.23°$.

3.5 Eigenmodes

Figure 3.8 shows new variables n, s, and θ and their relationship to the physical coordinate system presented in Figure 3.1. These variables simplify visualization of eigenmodes. Introducing characteristic variable $Ks = k_1 x_1 + k_3 x_3$ allows solutions to be represented in two-dimensional form where a flow variable ϕ has the functional form $\phi(x_2, s) = \mathrm{Re}[\phi(x_2)\exp(iKs)]$. Solutions are wavelike with wavenumber $K = \sqrt{k_1^2 + k_3^2}$ and oriented with an angle $\theta = \tan^{-1}(k_3/k_1)$ between the x_3 direction and the wavenumber vector, $\boldsymbol{s} = k_1\boldsymbol{e}_1 + k_3\boldsymbol{e}_3$, where $\boldsymbol{e}_1$ and $\boldsymbol{e}_3$ are unit vectors in x_1 and x_3 directions, respectively. Because k_1 and k_3 are non-negative, increasing s corresponds to increasing x_1 and/or x_3. The vector normal to the wavenumber vector in the x_1-x_3 plane is denoted by $\boldsymbol{n}$. Two new flow variables, normal vorticity fluctuations, $\omega_n' = \omega_i' n_i = -\omega_1' \cos\theta + \omega_3' \sin\theta$, and normal velocity fluctuations, $u_n' = u_i' n_i = -u_1' \cos\theta + u_3' \sin\theta$, are introduced to visualize unstable modes in the new coordinates. For inertial modes, k_1 is small in comparison to k_3, meaning $\boldsymbol{n} \sim -\boldsymbol{e}_1$ and $\boldsymbol{s} \sim \boldsymbol{e}_3$.

The base state contains no available potential energy, therefore the overall effect of buoyancy on vertical fluctuations is stabilizing. However, certain physical mechanisms, one example is the zigzag instability of Billant & Chomaz (2000*b*), can result in faster growing modes than possible in an unstratified fluid. It is worth noting that $u_3' = u_s' \cos\theta + u_n' \sin\theta$ so that, for an inclination θ, the normal velocity u_n' leads to vertical motion. Even if ρ' has the same sign as u_3', implying that the buoyancy term in the vertical momentum equation has a stabilizing effect on vertical fluctuations, ρ' can have a different sign than u_s' or u_n'. Thus, buoyancy may have a stabilizing effect on u_s' and destabilizing effect on u_n' or vice versa, while still stabilizing vertical motion.

Figure 3.9 shows an inertial mode in a homogeneous fluid with fairly weak anticyclonic rotation ($2\Omega = 0.1$). Since $\theta = 1.43°$ the plane is quasi-vertical, therefore we can make the approximations $\omega_n' \sim -\omega_1'$ and $\partial u_n'/\partial s \sim -\omega_2'$ to infer horizontal vorticity fluctuations from Figure 3.9 (a) and (b). Parcels of fluid with like-signed ω_1' and ω_2' occupy the region where $|x_2| < 0.5$. For $0 < 2\Omega < S(x_2)$, the condition of inertial instability, equations (3.17) and (3.18) show that ω_1' and

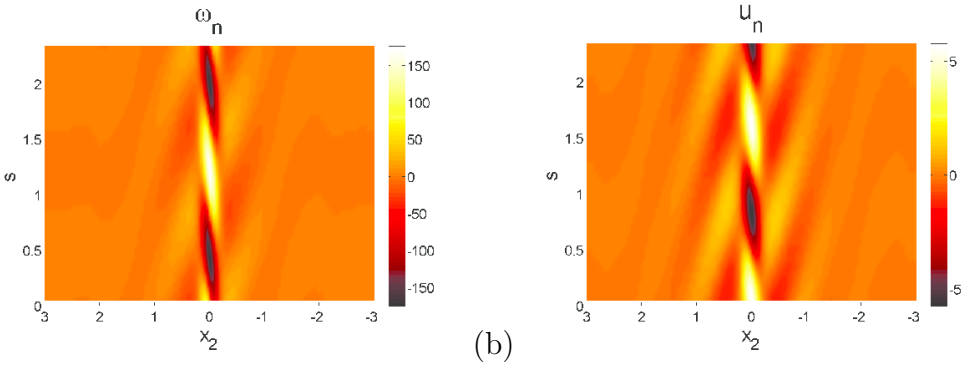

Figure 3.11: Plots of ω_n' (a) and u_n' (b) for a near zero absolute vorticity case without stratification, $Ri_b = 0$, $2\Omega = 0.95$, $k_1 = 0.444$, $k_3 = 4$, and $\theta = 6.33°$.

ω_2' must have the same sign for growth of the instability, otherwise mean shear cannot intensify horizontal vorticity fluctuations via vortex stretching. Figure 3.9 (c) shows velocity vectors corresponding to the ω_n' field from 3.9 (a) to aid in visualization. It is seen that positive (negative) ω_n' corresponds to counterclockwise (clockwise) rotation in the (x_2, s) plane. In later figures, velocity vectors are included for eigenmodes when it is more difficult to infer velocities from ω_n' plots.

Figure 3.10 shows an inertial mode with the same anticyclonic rotation rate but in a strongly stratified fluid. The lateral spread of vorticity fluctuations has increased considerably for inertial modes in a strongly stratified fluid compared to the homogeneous case in Figure 3.9. Looking at the region of positive ω_n' from Figure 3.10 (a) and corresponding density fluctuations from Figure 3.10 (c) it is clear that the vertical motion induced by ω_n' has the same sign as the density field such that buoyancy stabilizes ω_n' fluctuations. The normal component of the baroclinic term of equation 3.12 is shown in Figure 3.10 (d), further illustrating the stabilizing effect of buoyancy on ω_n'. Similarly, looking at regions of positive u_n' from Figure 3.10 (b) and corresponding density fluctuations from Figure 3.10 (c) the stabilizing effect of buoyancy on u_n' can be deduced. Density fluctuations are generated by both ω_n' and u_n' implying that buoyancy plays a stabilizing role, inhibiting generation of horizontal vorticity fluctuations via baroclinic torque.

Figure 3.11 shows an inertial mode in a homogeneous fluid with nearly zero absolute mean vorticity at the inflection point ($2\Omega = 0.95$). As with the weak

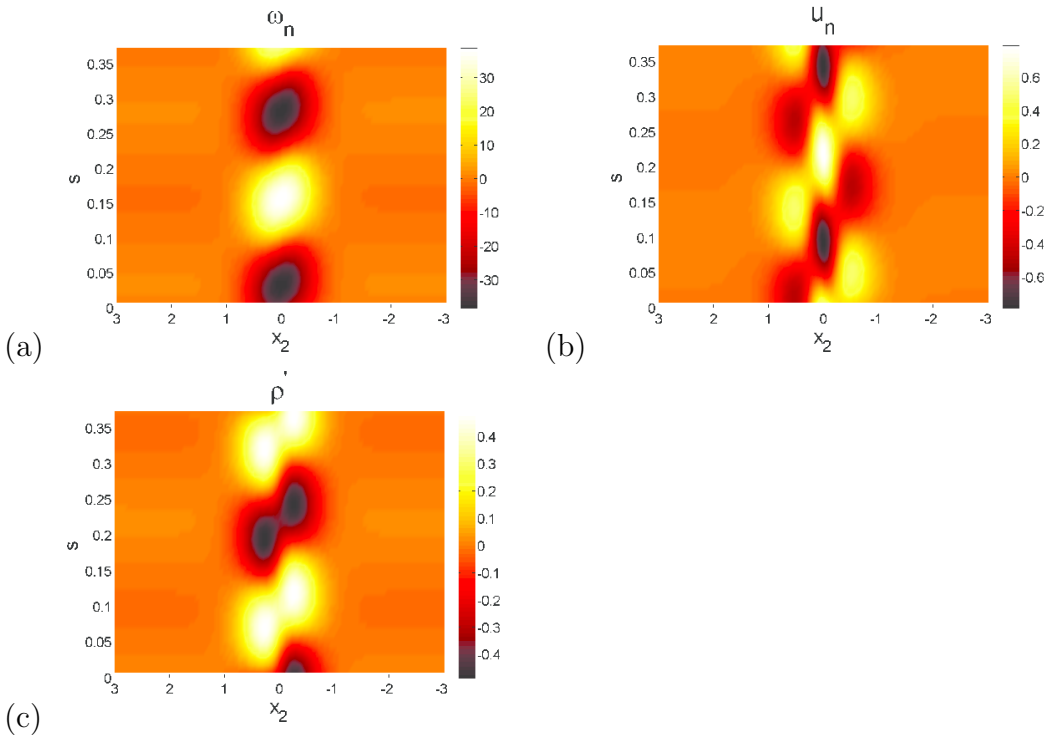

Figure 3.12: Plots of ω_n' (a), u_n' (b), and ρ' (c) for a barotropic mode from a zero absolute vorticity case with stratification, $Ri_b = 10$, $2\Omega = 1$, $k_1 = 0.444$, $k_3 = 25.3$, and $\theta = 1.0°$.

anticyclonic cases presented in figures 3.9 and 3.10, we observe regions of like-signed ω_1' and ω_2'. The lateral spread of the vorticity fluctuations is small because the local value of $-2\Omega\left(2\Omega - S\left(x_2\right)\right)$ has positive values only at $x_2 \sim 0$ where $S > 2\Omega > 0$. Figure 3.12 shows a large k_3 mode from the strongly stratified case with zero absolute mean vorticity at the inflection point. A dramatic difference in dynamics is observed between this mode and the inertial mode from Figure 3.11. Density fluctuations are generated by ω_n', but the u_n' field in Figure 3.12 (b) has the opposite sign of the ρ' field in Figure 3.12 (c). Therefore, u_n' fluctuations are aligned with the buoyancy force rather than opposed to it for the inertial mode in Figure 3.10. This destabilizing effect of buoyancy on u_n' is in contrast to the stabilizing effect seen earlier in the weak anticyclonic case. When $2\Omega = S$, the linearized fluctuating vorticity equations take the following form at the inflection point where $U_1 = 0$,

$$\frac{\partial \omega_1'}{\partial t} = \left(\frac{S}{2} + \Omega\right)\omega_2' - Ri_b\frac{\partial \rho'}{\partial x_2}, \tag{3.25}$$

$$\frac{\partial \omega_2'}{\partial t} = Ri_b\frac{\partial \rho'}{\partial x_1}. \tag{3.26}$$

Thus, for this base state, unstratified flow with zero absolute vorticity contains no mechanism to generate ω_2', which is why the zero absolute vorticity state tends to stabilize barotropic modes in homogeneous fluids as noted in section 3.4.

The buoyancy-driven instability in the case of zero absolute vorticity can be explained as follows. Quasi-streamwise vortices indicated by ω_n' in Figure 3.12 (a) distort isopycnals such that positively buoyant fluid is on one side of the vortices and negatively buoyant fluid is on the other, as observed in Figure 3.12 (c). Slight inclination of the quasi-streamwise vortices in the vertical direction, due to the small vertical component of $\boldsymbol{n}$, leads to the associated density gradient having a slight streamwise component, $\partial\rho'/\partial x_1$, which in turn leads to baroclinic formation of lateral vorticity, ω_2'. This is the only mechanism which can modify ω_2' fluctuations as seen in equation (3.26). The formation of ω_2' is reflected by $\partial u_n'/\partial s \sim -\partial u_1'/\partial x_3$ in Figure 3.12 (b). This lateral vorticity is then transferred to the quasi-streamwise vortices via coordinate system rotation and strain-induced

tilting according to equation (3.25).

For $|x_2| \gtrsim 0.3$ in figure 3.12, we see vertical shear ($\partial u_1'/\partial x_3 \sim -\partial u_n'/\partial s$) correlating with lateral density variation in the opposite manner than predicted by thermal wind balance, which is given below in equations (3.27) and (3.28). This is somewhat surprising, considering local values of $|Ro\,(x_2)\,| = S\,(x_2)\,/2|\Omega|$ are small away from the inflection point.

$$2\Omega\frac{\partial u_1}{\partial x_3} = Ri_b\frac{\partial \rho'}{\partial x_2}\,, \tag{3.27}$$

$$-2\Omega\frac{\partial u_2}{\partial x_3} = Ri_b\frac{\partial \rho'}{\partial x_1}\,. \tag{3.28}$$

Figure 3.13 shows the form of barotropic modes with non-zero k_3 for a non-rotating strongly stratified case. Figure 3.13 (c) shows quasi-streamwise parcels of buoyant fluid with large lateral spread. Density fluctuations in these parcels are maintained by vertical fluctuations due to jets of u_n' in the shear region as seen in Figure 3.13 (b). In is apparent that u_n' and ρ' are of the same sign so that the effect of stratification is stabilizing on u_n' fluctations. Figure 3.13 (a) and (d) show an array of alternating jets that are oriented in the lateral direction (x_2) outside of the shear region, but inclined with respect to the vertical and streamwise directions within the shear region. The physics driving this instability can be illustrated through the following arguments. A flow field begins with alternating layers of heavy and light fluid on top of one another that are not infinite, but spread far beyond the shear region as observed in Figure 3.13 (c). Lateral variation in density within the layers of buoyant fluid results in currents with u_2' directed towards and away from the shear region as seen in Figure 3.13 (d). Heavy parcels approach the shear region with slight negative vertical velocity, while light parcels approaches the shear region with slight positive vertical velocity. As the currents induced by ω_n' enter the shear region they encounter buoyant quasi-streamwise currents increasing their density anomaly, resulting in larger vertical velocity magnitudes until exiting the shear region on the opposite side of the buoyant layer. These quasi-lateral currents induce vertical shear ($\partial u_2'/\partial x_3 \sim \partial u_2'/\partial s$), as seen in Figure

3.13 (d), which then acts to generate ω_2' through tilting of mean vertical vorticity. Tilting of the ω_1' contained in the currents by the mean shear also leads to ω_2' formation. The generated ω_2' coincides with the quasi-streamwise jets observed in Figure 3.13 (b).

The density structures observed in Figure 3.13 are reminiscent of density intrusions observed in the experiments of Browand *et al.* (1987), Thorpe (1982), Liu *et al.* (1987), and Ivey & Corcos (1982) and the numerical simulations of Basak & Sarkar (2006). The mechanism proposed in these works involves vertical mixing that leads to tongues of downward propagating heavier fluid encountering tongues of upward propagating lighter fluid and then spreading laterally similarly to gravity currents. The arguments provided in the previous paragraph referring to the eigenmode described in Figure 3.13 offer an illustration of a linear mechanism that generates layers of buoyant fluid. These density structures could lead to a periodic array of non-turbulent density intrusions outside of the shear region where vertical mean vorticity is negligible.

Figure 3.14 shows modes from a rapidly rotating and strongly stratified case. Thermal wind balance explains much of the differences between this case and the non-rotating strongly stratified modes with horizontal density variations correlating appropriately with the observed vertical shear. From Figure 3.14 (b) and (d) we observe that regions of positive u_n' (or negative u_n') correlate with regions of negative u_s' (or positive u_s') implying that associated regions contain negative u_1' (or positive u_1'). By examining Figure 3.14 (b) - (d), the signs of both $\partial u_1'/\partial x_3$ and $\partial \rho'/\partial x_2$ can be determined near the inflection point. Positive values of $\partial u_1'/\partial x_3$ are found to correlate with negative values of $\partial \rho'/\partial x_2$ and vice versa as expected from equation (3.27) for $\Omega < 0$.

3.6 Conclusion

The three-dimensional instability of a stratified and rotating horizontally oriented hyperbolic shear layer has been investigated. Rapid rotation and/or strong stratification was found to result in self-similarity of growth rates with respect

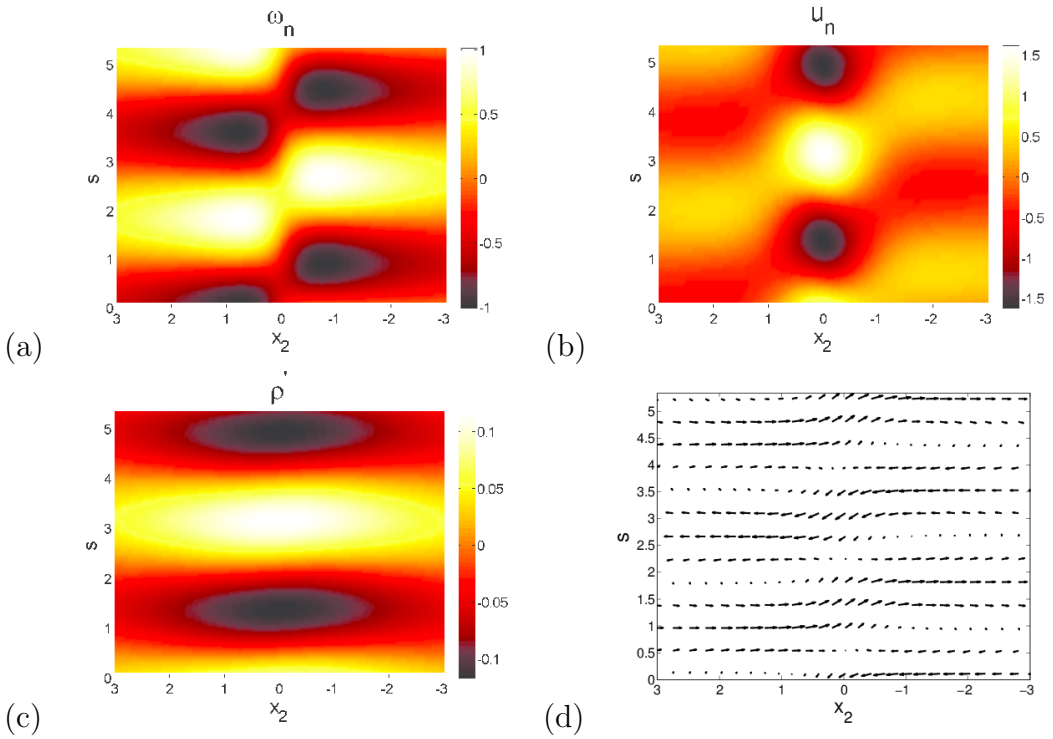

Figure 3.13: Plots of ω_n' (a), u_n' (b), ρ' (c), and velocity vectors (d) for a barotropic mode from a non-rotating case with strong stratification, $Ri_b = 10$, $2\Omega = 0$, $k_1 = 0.3$, $k_3 = 1.7$, and $\theta = 10.0°$.

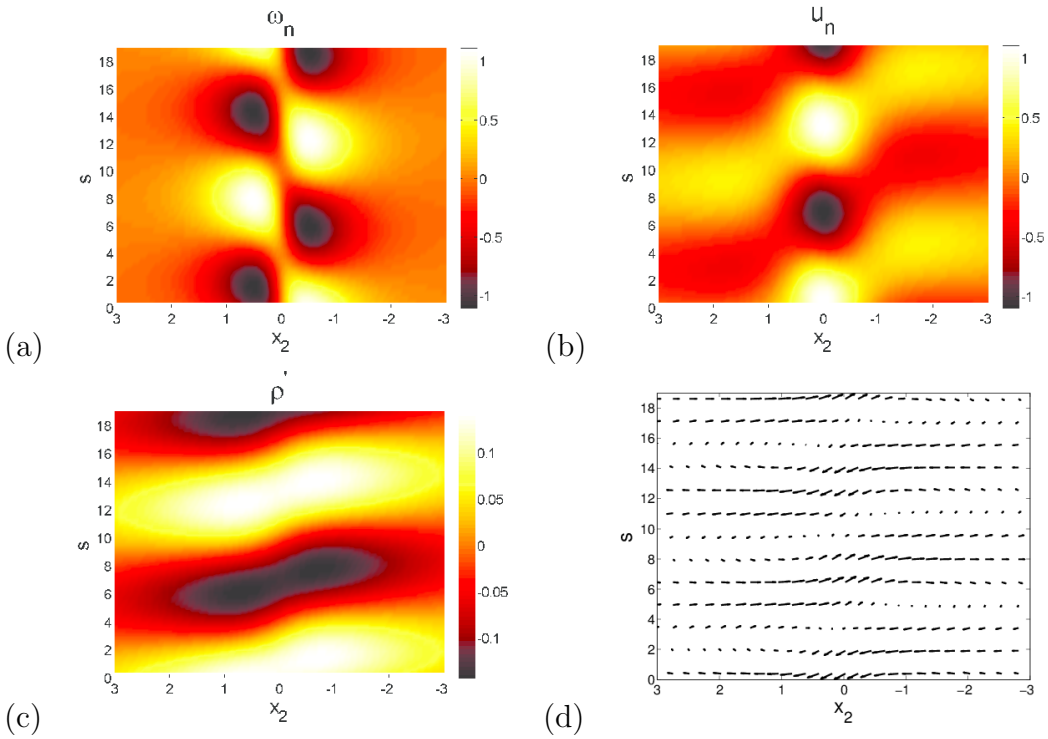

Figure 3.14: Plots of ω_n' (a), u_n' (b), ρ' (c), and velocity vectors (d) for a barotropic mode from a rapidly rotating case with strong stratification, $Ri_b = 10$, $2\Omega = -2$, $k_1 = 0.3$, $k_3 = 0.4$, and $\theta = 36.9°$.

to vertical wavenumber of perturbations. For unstratified rapidly rotating cases, vertical wavenumbers were found to scale as $2|\tilde{\Omega}|k_3 L/S$ where $2\tilde{\Omega} = 2\,(\Omega - 1/4)$ corresponds to the deviation with respect to the most destabilizing rotation rate. While the difference between Ω and $\tilde{\Omega}$ is not significant in geostrophic flows, the difference is appreciable for less rapidly rotating cases such as submesoscale shear flows where $2\,|\Omega|\,/S$ is not particularly large. This scaling is consistent with the Taylor-Proudman theorem in the limit of $|\Omega| \to \infty$, where only $k_3 = 0$ modes are unstable. For strongly stratified rapidly rotating cases, vertical wavenumbers were found to scale as $2|\tilde{\Omega}|k_3 L/N$. This result is consistent with quasi-geostrophy for very large $2|\Omega|/S$ and N/S, but the distinction between Ω and $\tilde{\Omega}$ is still non-negligible in the submesoscale regime.

For weak to moderate rotation rates, stratification was found to stabilize the inertial instability. The distinction between growth rates associated with inertial and barotropic modes lessened as the zero absolute vorticity state was approached. Rapid rotation stabilizes low k_1, high k_3 modes in an unstratified fluid. Such stabilization is not observed in the presence of strong stratification.

Analysis of eigenmodes provided insight regarding the underlying physics of the inertial instability and barotropic instability in a rotating strongly stratified fluid for small amplitude perturbations. Quasi-streamwise vortices associated with the inertial instability were suppressed via baroclinic torque when stratification was strong. Analysis of a non-rotating strongly stratified barotropic mode showed a potential linear mechanism for generation of density intrusions. Adding rapid rotation modified the barotropic mode in a manner consistent with thermal wind balance.

For strongly stratified flow with zero absolute vorticity at the inflection point, the vertical scale associated with barotropic instability was significantly modified. Density anomalies generated by quasi-streamwise vortices with a small vertical inclination led to baroclinic formation of lateral vorticity which, through tilting by system rotation and strain, sustains the quasi-streamwise vortices. This mechanism is fundamentally different than the mechanism driving barotropic modes when only rotation or stratification effects are included. In chapter 4 the non-linear

evolution of the stratified and rotating horizontal shear layer will be explored using direct numerical simulation and comparisons will be made between linear and non-linear physics.

The contents of this chapter are published in the *Journal of Fluid Mechanics*. E. Arobone and S. Sarkar. "Evolution of a stratified rotating shear layer with horizontal shear. Part I. Linear stability", J. Fluid Mech., 703, 29-48, 2012. The authors are pleased to acknowledge support by the Jacobs School Graduate Fellowship for E.A. and the National Science Foundation CDI program through Grant No. OCE-0835839 for S.S. and E.A. The authors also are grateful for computational resources through the Triton Affiliations and Partners Program at San Diego Supercomputing Center.

Chapter 4

Nonlinear Evolution of a Stratified Rotating Shear Layer with Horizontal Shear

4.1 Introduction

The effects of strong stratification and moderate coordinate system rotation rates, where $Fr_h = S/N \lesssim O(1)$ and $Ro = S/2\Omega \sim O(1)$, on shear flow is important for basic understanding of submesoscale ocean dynamics. This study explores a horizontally oriented hyperbolic tangent mixing layer including stratification and rotation effects. Isolated horizontal shear is prevalent in boundary currents and in the wake of isolated topography. Previous work has explored the nonlinear evolution of horizontally oriented shear layers subjected to rotation (Métais *et al.*, 1995; Potylitsin & Peltier, 2003) or stratification (Basak & Sarkar, 2006; Arobone & Sarkar, 2010) alone, but not in combination. Figure 4.1 gives a schematic illustrating the rotating stratified horizontal shear layer and relevant dimensional parameters.

In Arobone & Sarkar (2012) the effect of rotation and stratification on growth rates for linear evolution of exponentially growing modes was explored for a horizontal shear layer. The unstratified rotating shear layer is known to

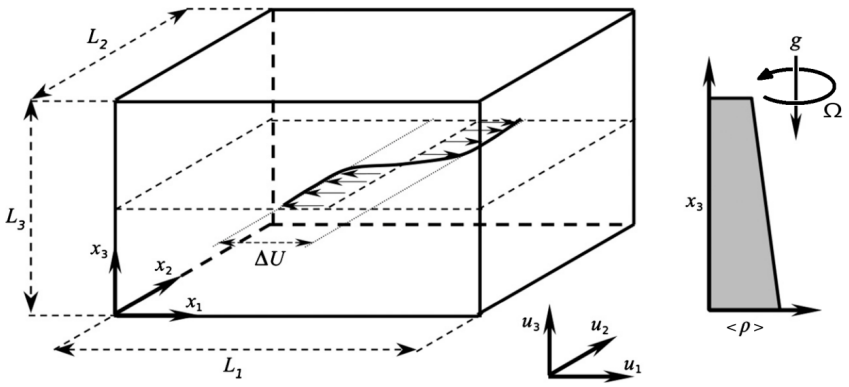

Figure 4.1: Schematic of the rotating stratified horizontal shear layer. Additional relevant parameters include the vorticity thickness, δ_ω, kinematic viscosity ν, scalar diffusivity κ and reference density ρ_0.

be susceptible to inertial (i.e. centrifugal) instability, that typically manifests as overturning motions with low streamwise wave number, and the barotropic instability associated with horizontal shear that is manifested as vortex trains such as Kelvin-Helmholtz (KH) billows. Stratification acted to stabilize the inertial instability for moderate values of $Ri_b^{-1/2}k_3$, where $Ri_b = N^2/S^2$, and increased the range of vertical wavenumbers associated with both inertial and barotropic instability. When the absolute vertical vorticity, $\langle\omega_3\rangle + 2\Omega = -S + 2\Omega$, was nearly zero at the centerline, a new instability was found to occur whereby a much larger range of vertical scales was destabilized relative to the non-rotating case as seen in Figure 4.2. Note that the inertial instability of rotating flows is inoperative for $-S + 2\Omega \geq 0$. Lastly, self-similar regimes were observed when stratification was strong ($Ri_b \geq 1$) and/or the rotation rate was rapid ($|2\Omega/S| \gg 1$). In this chapter, we assess the role of buoyancy during the *nonlinear* evolution of the stratified, rotating shear layer through direct numerical simulation (DNS).

The horizontally oriented shear layer under the influence of rotation alone and without stratification was explored by Métais *et al.* (1995) using direct and large-eddy simulations. The Reynolds number based on free stream velocity difference and initial vorticity thickness was $Re = 100$ and a 64^3 grid was used. In cases with cyclonic rotation (and anticyclonic rotation when $|Ro\,(t)| \leq 1$) three-dimensionality was inhibited, consistent with the Taylor-Proudman theorem. For

weaker anticyclonic rotation, the flow was strongly destabilized with maximum destabilization achieved when $Ro \approx -2.5$, consistent with the linear theory of Yanase *et al.* (1993). In the strongly destabilized cases, the vorticity in the shear layer evolved to a collection of strong longitudinal vortex tubes, slightly inclined with respect to vertical. KH rollers were suppressed, yet more enstrophy resulted than in the non-rotating case. The weak anticyclonic cases approached a state of near constant shear with approximately zero absolute vorticity. Vertical vorticity was proposed to be destroyed via the weak absolute vorticity stretching mechanism of Lesieur *et al.* (1991).

The effect of stratification alone without system rotation on a horizontally oriented shear layer was explored by Basak & Sarkar (2006) and Arobone & Sarkar (2010) using DNS. The structural organization of vorticity and density fields was the focus of Basak & Sarkar (2006). In strongly stratified cases, columnar vortex cores emerged from an initially turbulent state and subsequently dislocated forming a lattice of 'pancake' eddies with large vertical shear and density gradients between the pancakes. The vertical length of vortex cores was found to be proportional to $\Delta U/N$ where ΔU denotes the imposed velocity difference and N the uniform stratification. Density intrusions and internal gravity waves were observed away from the sheared region. Arobone & Sarkar (2010) extended this work, focusing on statistics and the role of coherent vortical structures. Many statistics, such as turbulent stresses, approached self-similar profiles once $Ri_b\,(t) \gg 1$. For large Ri_b, transport of density fluctuations was strongly counter-gradient in sharp contrast with the co-gradient transport of a passive tracer observed in the unstratified case. In strongly stratified cases coherent structure evolution exhibited vortical structure reminiscent of the zigzag instability (Billant & Chomaz, 2000*b*).

There are observations of asymmetry between cyclonic and anticyclonic vortices in geophysical flows, e.g. figure 1 of Potylitsin & Peltier (1998) which shows asymmetry of the von Karman vortex street in the lee of mountains on the island of Jan Mayen. Flament *et al.* (2001) observed a horizontal shear layer, containing anticylonic vortices having $\omega_3 \sim -f$, forming in the westward North Equatorial Current past the island of Hawaii. The shear layer grew in thickness owing to

paring of these anticylonic vortices. It was suggested that stronger vortices were not observed due to inertial instability. Anticyclones are quite difficult to generate in the laboratory in a homogeneous fluid, e.g. Kloosterziel & van Heijst (1991) and Afanasyev & Peltier (1998). In the latter publication the inertial instability was clearly demonstrated for various values of Ro through novel experimental techniques.

Numerical experiments have also shown asymmetry between cyclones and anticyclones at moderate rotation. Bartello *et al.* (1994) used numerical simulation to examine the three-dimensionalization of initially quasi-two-dimensional flow along with the two-dimensionalization of initially isotropic three-dimensional flow in an unstratified background. Without rotation, three dimensionalization of all initially quasi-two-dimensional vortices was observed. When the Coriolis parameter matched $[\omega_{2D}]_{\mathrm{rms}}$ a rapid destabilization of anticyclones occurred, however both cyclones and anticyclones remained stable for more rapid rotation rates. Forced three-dimensional rotating stratified isotropic turbulence was investigated numerically by Smith & Waleffe (2002). Forcing was localized at a large wavenumber. When Fr was less than a critical value, energy transferred from small to large scales. For $N/f \gg 2$, large scale flow arose as vertically sheared horizontal flow with PV modes playing a secondary role. For $1/2 \leq N/f \leq 2$, PV modes dominated and inertial-gravity waves were insignificant. Lastly, for $N/f \ll 1/2$ it was suggested, but not demonstrated, that flow would be dominated by large-scale cyclonic vortices as in the unstratified rapidly rotating cases. Experiments exploring grid turbulence in a rotating stratified tank were carried out by Praud *et al.* (2006). For large magnitude of Ro, a significant decay of kinetic energy was observed with respect to the lower Ro cases, irrespective of the stratification strength. In the low Ro regime, the intense vortices were all cyclonic. At late times, they took the form of lens-like eddies with an aspect ratio proportional to f/N.

The final state of an initially inertially unstable distribution of vorticity is of interest. Kloosterziel *et al.* (2007*a*) studied the unfolding of the inertial instability in initially barotropic vortices in a uniformly stratified fluid. The simulations were

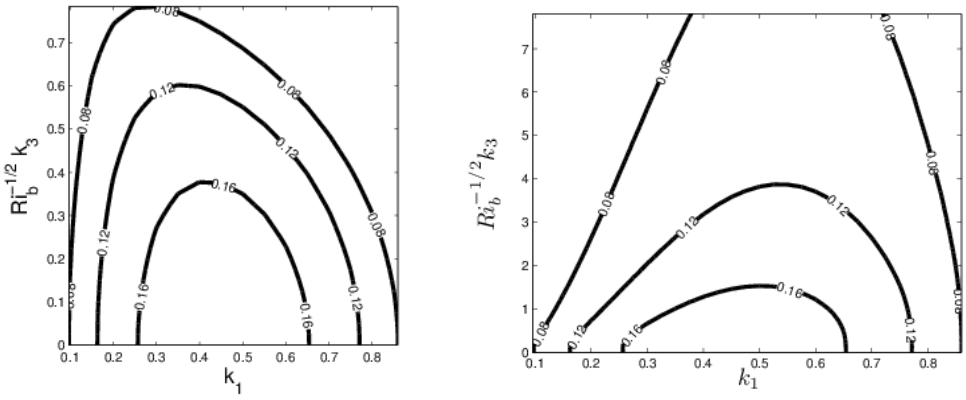

(a) $Ri_b = 4$, $2\Omega = 0$ (b) $Ri_b = 10$, $2\Omega = -1$

Figure 4.2: Contours of growth rate for linear stability of the stratified horizontal shear layer for the (a) non-rotating case and (b) zero absolute vorticity case based on the results of Arobone & Sarkar (2012).

axisymmetric such that the effects of inertial instability were isolated. Barotropic vortex dipoles emerged mixing momentum such that flow evolved to a state that was no longer inertially unstable. A theoretical construction was also provided to infer the final state of angular momentum at high Reynolds number given the initial distribution. Interestingly, the arguments of Kloosterziel *et al.* (2007*a*) implied that the inertial instability would mix the rotating shear layer to a state with nearly zero absolute vorticity as was indeed found by Métais *et al.* (1995), Kloosterziel *et al.* (2007*b*) and Plougonven & Zeitlin (2009) through DNS of anticyclonic cases with weak system rotation rate. Carnevale *et al.* (2011) provided a method to predict the aftermath of vortex breakup in unstratified rotating flow taking into account both inertial and barotropic instability of vortices.

Observations of asymmetry between cyclonic and anticyclonic vortices in nature as well as in laboratory/numerical experiments have prompted stability analysis of barotropic vortices under the influence of stratification and rotation. Potylitsin & Peltier (1998) explored the effect of stratification and rotation on the three-dimensional stability of barotropic vortices with elliptic cross-sections resulting from the KH instability of a hyperbolic tangent shear layer. Maximum destabilization in the unstratified case was observed for anticyclonic rotation with

$Ro^{-1} = -\Omega/S = -0.2$, with the edge mode growth rate being dominant, and the inertial instability mechanism underlying this instability being absent in the non-rotating case. Stratification was found to suppress the stationary edge mode, while only slightly attenuating the first harmonic edge mode. No additional modes were found to emerge in the presence of stratification. The elliptical mode is least influenced by stratification and is largely dominant for stronger anticyclonic rotation, $-0.5 < -\Omega/S < -0.3$. No modes were significantly unstable for $Ro^{-1} \geq 0.5$, but the stability of this regime was not explored for $Fr^{-2} = N^2/S^2 > 0.2$. The effect of ellipticity on three-dimensional instabilities of Stuart vortices was explored in Potylitsin & Peltier (1999). For low ellipticity the inertial instability dominated, while for high ellipticity a rotation augmented elliptical instability was most unstable. The nonlinear evolution of columnar vortices subject to rotational effects alone was explored in Potylitsin & Peltier (2003). Here, the distinctions between non-linear inertial and elliptical instabilities are clearly presented using isosurfaces of perturbation vorticity.

The zigzag instability of a counter-rotating vertical vortex pair in a stratified fluid introduced by Billant & Chomaz (2000*b*) was explored by Otheguy *et al.* (2006*b*) for a co-rotating vortex pair, as emerge in a shear layer. Perturbations changed from antisymmetric to symmetric when vortices were co-rotating, and their wavelength depended on the separation distance rather than vortex radius as was the case for counter-rotating vortices. The effect of planetary rotation on the co-rotating zigzag instability was investigated by Otheguy *et al.* (2006*a*). Anticyclonic rotation with $Ro < -3.67$ was found to decrease the vertical length scale associated with zigzag instability, while weaker anticyclonic rotation rates increased the length scale. For $Ro \to 0$, the quasi-geostrophic scaling of vertical length scale proportional to vortex spacing multiplied by f/N was observed.

In the present chapter, we follow up the linear stability analysis for a horizontally oriented rotating and stratified shear layer from Part 1 with a DNS study that includes a series of simulations with nearly 1 billion points simulating a shear layer with an initial Reynolds number of 2400. Section 2 introduces and motivates the mathematical model and simulation parameter regime. The overall evolution

of the mean flow is summarized in section 3 and the approach towards a final state of zero absolute vorticity is assessed for anticyclonic rotation. The preceding literature survey shows that rotation influences the emergence of various instabilities including the inertial instability, barotropic shear instability, zigzag instability and the buoyancy-induced instability at zero absolute vorticity found in Part 1. The manifestation of these instabilities in coherent vortex dynamics is discussed in section 4 and the qualitative difference in the cases with moderate anticyclonic rotation rates are highlighted. Visualizations of vorticity are presented in section 5 to illustrate how the vortical signature of the inertial instability differs from that of the buoyancy instability which occurs when the flow passes through zero absolute vorticity. Section 6 explores the fluctuating enstrophy budget terms, paying particular attention to nonlinear vortex stretching and changes in the baroclinic torque when centerline absolute vorticity is nearly zero. In section 7, statistics to quantify the turbulent nature of fluctuations such as buoyancy Reynolds number, skewness of velocity derivative, spectra, and mixing efficiency are discussed. Conclusions are drawn in section 8.

4.2 Formulation

The dimensional equations for conservation of mass, momentum, and density for a Boussinesq fluid in a frame of reference rotating about the vertical axis are given below with dimensional variables denoted by * (centrifugal acceleration is neglected) :

$$\frac{\partial u_i^*}{\partial x_i^*} = 0$$

$$\frac{\partial u_i^*}{\partial t^*} + \frac{\partial \left(u_i^* u_j^*\right)}{\partial x_j^*} + \epsilon_{i3k} 2\Omega^* u_k^* = -\frac{1}{\rho_0^*}\frac{\partial p^*}{\partial x_i^*} + \nu^* \frac{\partial^2 u_i^*}{\partial x_j^* \partial x_j^*} - g^* \delta_{i3}$$

$$\frac{\partial \rho^*}{\partial t^*} + \frac{\partial \left(\rho^* u_j^*\right)}{\partial x_j^*} = \kappa^* \frac{\partial^2 \rho^*}{\partial x_j^* \partial x_j^*}$$

The density and pressure fields are decomposed in the following manner,

$$\rho^*\left(x_i^*, t^*\right) = \rho_0^* + \overline{\rho}^*(x_3^*) + \rho'^*\left(x_i^*, t^*\right),$$
$$p^*\left(x_i^*, t^*\right) = \overline{p}^*\left(x_2^*, x_3^*\right) + p'^*\left(x_i^*, t^*\right),$$

where $\overline{\rho}^*$ represents the background stratification and $\overline{p}^*$ is in hydrostatic and geostrophic balance with the initial density profile $(\rho_0^* + \overline{\rho}^*)$ and initial mean velocity profile. The initial mean velocity corresponds to a barotropic hyperbolic tangent mixing layer of the form

$$\langle u_1^* \rangle = \frac{\Delta U^*}{2} \tanh\left(\frac{2x_2^*}{\delta_\omega^*}\right),$$

with linear vertical stratification $d\langle\rho^*\rangle/dx_3^*$, Coriolis parameter $f^* = 2\Omega^*$, vorticity thickness δ_ω^*, and velocity difference ΔU^* as introduced in Figure 4.1.

The non dimensional variables for this problem are given as

$$t = \frac{t^*\Delta U^*}{\delta_{\omega,0}^*}, \quad x_i = \frac{{x_i}^*}{\delta_{\omega,0}^*}, \quad u_i = \frac{{u_i}^*}{\Delta U^*}, \quad \rho' = \frac{-\rho'^*}{\delta_{\omega,0}^*\left(d\overline{\rho}^*/dx_3^*\right)}, \quad p' = \frac{p'^*}{\rho_0^*{\Delta U^*}^2}.$$

The following non-dimensional equations for continuity, momentum conservation, and density are obtained along with relevant non-dimensional parameters

$$\begin{aligned}
&\frac{\partial u_i}{\partial x_i} = 0, \\
&\frac{\partial u_i}{\partial t} + \frac{\partial\left(u_i u_j\right)}{\partial x_j} + \epsilon_{i3k} 2\Omega u_k = -\frac{\partial p'}{\partial x_i} + \frac{1}{Re_0}\frac{\partial^2 u_i}{\partial x_j \partial x_j} - Ri_{b,0}\rho'\delta_{i3}, \\
&\frac{\partial \rho'}{\partial t} + \frac{\partial\left(\rho' u_j\right)}{\partial x_j} - u_3 = \frac{1}{Re_0 Pr}\frac{\partial^2 \rho'}{\partial x_j \partial x_j}, \\
Re_0 = \frac{\Delta U^* \delta_{\omega,0}^*}{\nu^*}, \quad &Ri_{b,0} = -\frac{g^*}{\rho_0^*}\frac{d\overline{\rho}^*}{dx_3^*}\frac{{\delta_{\omega,0}^*}^2}{{\Delta U^*}^2} \approx \frac{N^{*2}}{S^{*2}}, \\
2\Omega_0 = Ro_0^{-1} = -\frac{2\Omega^*\delta_{\omega,0}^*}{\Delta U^*}, \quad &Pr = \frac{\nu^*}{\kappa^*}.
\end{aligned} \tag{4.1}$$

Table 4.1: Simulation parameters and case names. L_i and N_i represent the length of domain and number of computational points, respectively, in each direction. In all cases Pr is set to unity.

case	Re_0	$Ri_{b,0}$	Ro_0	$2\Omega_0$	L_1	L_2	L_3	N_1	N_2	N_3
$Ri1A1$	2400	1	-1	-1	100	50	50	1536	768	768
$Ri1A2$	2400	1	-2	-0.5	100	50	50	1536	768	768
$Ri1A10$	2400	1	-10	-0.1	100	50	50	1536	768	768
$Ri1N$	2400	1	∞	0	100	50	50	1536	768	768
$Ri1C10$	2400	1	10	0.1	100	50	50	1536	768	768
$Ri1C2$	2400	1	2	0.5	100	50	50	1536	768	768
$Ri0A10$	2400	0	-10	-0.1	100	50	50	1536	768	768
$Ri0C10$	2400	0	10	0.1	100	50	50	1536	768	768
$Ri1A1Re600$	600	1	-1	-1	80	40	40	512	256	256
$Ri1A2Re600$	600	1	-2	-0.5	80	40	40	512	256	256
$Ri1A5Re600$	600	1	-5	-0.2	80	40	40	512	256	256
$Ri1A10Re600$	600	1	-10	-0.1	80	40	40	512	256	256
$Ri0A5Re600$	600	0	-5	-0.2	80	40	40	512	256	256

Here, Pr is taken to be unity for the sake of reasonable computational cost. 2Ω is defined such that positive (negative) values imply cyclonic (anticyclonic) rotation, note that this convention differs from part I. Dirichlet boundary conditions are enforced for all flow variables at the transverse boundaries where flow variables are set to zero except for streamwise velocity u_1 which takes the value associated with the mean velocity of the shear layer. Periodicity is enforced in the streamwise and vertical directions through Fourier collocation. Boundary influence increases with time as the shear layer grows laterally.

Initial conditions contain both two- and three-dimensional fluctuations. The 2D fluctuations are invariant in the vertical direction, and both fluctuating fields are triply-periodic with a prescribed spectrum. Fluctuations are confined to the shear region through multiplication by a Gaussian curve. The 2D fluctuations have a spectrum of the following form, $E_{2\mathrm{D}}(k) \propto k^8 \exp\left[-4\left(k/k_0\right)^2\right]$. 3D fluctuations, on the other hand, have a shallower spectrum of the form $E_{3\mathrm{D}}(k) \propto k^4 \exp\left[-2\left(k/k_0\right)^2\right]$. The 2D fluctuations are approximately 20 times more energetic than the 3D fluctuations and $k_0 = \pi$. After initialization, $\langle u_i' u_i' \rangle = 0.021$ at

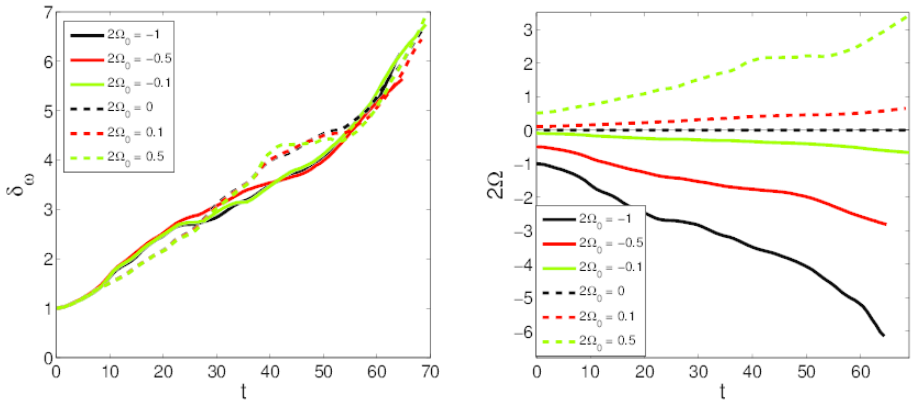

(a) (b)

Figure 4.3: Temporal evolution of (a) vorticity thickness δ_ω and (b) non-dimensional rotation rate $2\Omega\,(t) = 2\Omega^* \delta_\omega\,(t)\,/\Delta U$ for each stratified case at $Re_0 = 2400$. Note that positive (negative) Ω_0 corresponds to cyclonic (anticyclonic) rotation.

the centerline.

4.2.1 Computational Method

The numerical algorithm is different from Arobone & Sarkar (2010) which employed Fourier collocation in the streamwise and vertical directions and second-order staggered finite differencing in the transverse direction. Here, instead, fourth-order compact differencing on a collocated grid is performed in the transverse direction. The following details are the same as in Arobone & Sarkar (2010) and included for completeness. The Navier-Stokes and density equations are marched using a third order Runge-Kutta time scheme. A Rayleigh damping function is used near the $x_2 = \pm L_2/2$ boundaries, with a width of approximately $3\delta_{\omega,0}$, to prevent spurious reflections. The Poisson equations for pressure and removal of velocity divergence are solved using the Thomas algorithm. Parallelization is accomplished using MPI. Case specific computational details are shown in Table 4.1.

4.2.2 Case Study

A total of eight computationally-intensive simulations at $Re_0 = 2400$ were performed as listed in Table 4.1. Six simulations included stable stratification, while the other two were effectively unstratified with a vertical density gradient but no gravitational force. Three anticyclonic rotation rates were explored in the stratified cases, while one was explored in the unstratified cases. The $Ri1A10$, $Ri1A2$, and $RiA1$ cases explore the inertially unstable regime and zero absolute vorticity state with $Ri1A10$ running entirely in the inertially unstable regime, $RiA1$ starting with zero absolute vorticity, and $Ri1A2$ passing through both inertially unstable and the zero absolute vorticity states. The selection of $Ri_{b,0} = 1$ for the stratified cases is motivated by the observation of statistics showing a strong dependence on $Ri_b(t)$ for $Ri_b(t) \gtrsim 1$ and self-similar statistical behavior for $Ri_b(t) \gtrsim 10$ in Arobone & Sarkar (2010). The value of $Ri_b(t)$ increases by a factor of nearly 50 in our simulations owing to the almost sevenfold increase in shear layer thickness. Therefore the choice of initial stratification corresponding to $Ri_{b,0} = 1$ is likely sufficient to explore the strongly stratified regime. Approximately, 1 billion points are employed for the $Re_0 = 2400$ cases leading to excellent resolution with at least 5 decades drop in energy spectra during the evolution of the flow. Five smaller simulations with one third as many grid points in each direction were also performed at lower Reynolds number. These cases are used to aid in understanding the far more complex higher Re simulations.

4.3 Overall Evolution of the Mean Flow

Figure 4.3 (a) shows that the shear layer width, measured by the vorticity thickness, grows with increasing time. The difference of shear layer width among the various cases is not large but, as will be shown later in detail, the evolution of the fluctuations differs qualitatively in many aspects. Figure 4.3 (b) shows that the magnitude of non-dimensional rotation rate, $2\Omega(t) = 2\Omega^* \delta_\omega(t) / \Delta U^*$, increases with time since $\delta_\omega(t)$ increases. Thus, rotation exerts increasing control during the course of the simulations. The stratified case with $2\Omega_0 = -0.5$ exhibits

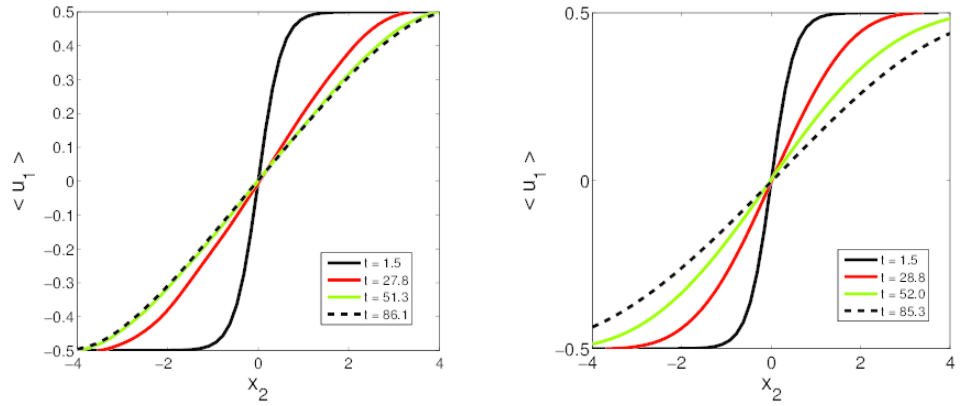

(a) $2\Omega_0 = -0.2$ and $Ri_{b,0} = 0$, Ri0A5Re600

(b) $2\Omega_0 = -0.2$ and $Ri_{b,0} = 1$, Ri1A5Re600

Figure 4.4: Figures showing the temporal evolution of the mean flow in the shear layer (a) without and (b) with stratification for cases with $Re_0 = 600$ and with weak anticyclonic rotation.

a reduction of growth rate at intermediate time, passes through the zero absolute vorticity state, and continues to thicken.

Figure 4.4 shows the evolution of mean velocity in the shear layer for low Re cases with $2\Omega_0 = -0.2$ without and with stratification, respectively. Figure 4.4 (a) shows the mean flow in the case without stratification evolves to a quasi-steady state, this state corresponds to $\langle\omega_3\rangle + 2\Omega_0 \approx -0.04$. The results are consistent with the mixing of angular momentum to a zero absolute vorticity state found by Métais *et al.* (1995) and suggested by Kloosterziel *et al.* (2007*b*) to be the high-Re limit of inertially unstable flows. Correspondingly, the vorticity thickness stops increasing at late time. In the stratified $2\Omega_0 = -0.2$ case of Figure 4.4 (b), the flow does not become quasi-steady. The value of δ_ω shows a slight plateau near zero absolute vorticity, but then exhibits unabated increase.

The reasons for the stratified flow to continue mixing momentum beyond the zero mean value of absolute vorticity, $\omega_a = \omega_3 + 2\Omega_0$, are examined. An evolution equation for mean absolute vertical enstrophy, $\langle\omega_a\rangle^2/2$, is given below in equation (4.3) and its domain-integrated terms are plotted in Figure 4.5. Mean absolute enstrophy is analyzed as opposed to mean relative enstrophy, $\langle\omega_3\rangle^2/2$, due to the latter's explicit dependence on rotation rate. The nonlinear stretching and tilting

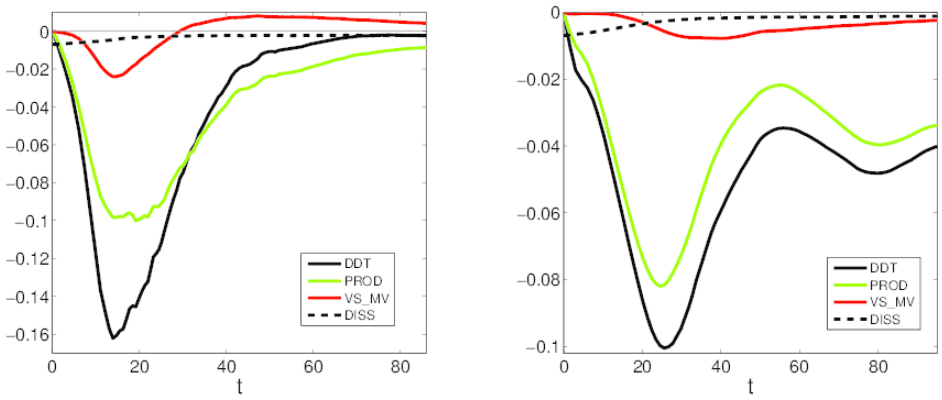

(a) $2\Omega_0 = -0.2$ and $Ri_{b,0} = 0$, Ri0A5Re600

(b) $2\Omega_0 = -0.2$ and $Ri_{b,0} = 1$, Ri1A5Re600

Figure 4.5: Figures showing the temporal evolution of integrated enstrophy budget terms (a) without and (b) with stratification for cases with $Re_0 = 600$ and with weak anticyclonic rotation.

term, VS_MV, is also present in the equation for fluctuating vertical enstrophy, $\langle \omega_3'^2 \rangle /2$, evolving differently between stratified and unstratified cases. In strongly turbulent flows, this term is a source of both mean and fluctuating enstrophy, but in the presence of strong stratification $\langle \omega_k' s_{k3}' \rangle$ is significantly suppressed as the flow becomes quasi-two-dimensional. The PROD term is an exchange between mean and fluctuating components of vertical enstrophy. Figure 4.5 (a) shows that, in the unstratified case, an approximate balance between increase of $\langle \omega_a \rangle^2$ by VS_MV and reduction by PROD is found for $t > 50$ leading to an asymptotic state with DDT approximately zero. Quasi-two-dimensional flow also acts to increase the magnitude of PROD through enhanced lateral stirring of vertical vorticity. Additionally, the zero absolute vorticity instability of Arobone & Sarkar (2012) only emerges in the presence of strong stratification and may be responsible for the increase in magnitude of PROD when $t \approx 55$ in Figure 4.5 (b). It is worth nothing that $2\Omega(t = 55) = -1.09$ and the centerline absolute vorticity is zero when $t \approx 46$. As will be shown in section 6, the baroclinic production of lateral vorticity (ω_2) helps maintain fluctuating enstrophy beyond the zero absolute vorticity state.

$$\overbrace{\frac{\partial}{\partial t}\left[\frac{1}{2}\left\langle\omega_a\right\rangle^2\right]}^{\text{DDT}} = \overbrace{\left\langle u_2'\omega_3'\right\rangle\frac{\partial\left\langle\omega_a\right\rangle}{\partial x_2}}^{\text{PROD}} - \frac{\partial}{\partial x_2}\left[\left\langle\omega_a\right\rangle\left\langle u_2'\omega_3'\right\rangle\right] \tag{4.2}$$

$$+\overbrace{\left\langle\omega_a\right\rangle\left\langle\omega_k's_{k3}'\right\rangle}^{\text{VS\_MV}} + \overbrace{\frac{1}{Re}\left\langle\omega_a\right\rangle\frac{\partial^2\left\langle\omega_a\right\rangle}{\partial x_2\partial x_2}}^{\text{DISS}} \tag{4.3}$$

4.4 Dynamics of Coherent Structures

Coherent vortical structures are isolated using the λ_2 criterion of Jeong & Hussain (1995), defined as the median eigenvalue of the symmetric tensor $S_{ik}S_{kj} + \Omega_{ik}\Omega_{kj}$. S_{ij} and Ω_{ij} are the rate of strain and rotation tensors, respectively. λ_2 enables straightforward three-dimensional visualization of coherent vortex dynamics by rendering surfaces where $\lambda_2 = \epsilon$, with a small negative threshold $\epsilon = -0.01$ as in Arobone & Sarkar (2012). The authors have selected λ_2 over Δ or Q, which from experience generate significant false positives in the shear layer, especially in the braid region. Due to the large size of datasets, Lagrangian methods of coherent vortex extraction are prohibitively expensive and were not employed.

4.4.1 Non-Rotating Stratified Case

λ_2 isocontours were used by Arobone & Sarkar (2010) to explore coherent vortex dynamics in a stratified horizontal shear layer. A transition from three-dimensional incoherent turbulence to coherent quasi-vertical structures to dislocated vortex cores was observed in the strongly stratified case, $A3$, with $Ri_{b,0} = 1.13$. A mechanism qualitatively similar to the zigzag instability was found to be responsible for slicing and breaking apart these quasi-vertical coherent vortices that emerged from the soup of turbulence. Case $A3_{\text{low}}$ of Arobone & Sarkar (2010) had very small amplitude initial fluctuations, did not develop three-dimensional incoherent turbulence, but did result in quasi-vertical coherent

vortices, the zigzag instability, and vertical slicing at late time similar to case $A3$. The evolution of case $Ri1NRe600$ is similar to case $A3_{\mathrm{low}}$. This is likely due to quasi-2D initial conditions used here that favor the early formation of coherent structures as opposed to fully 3D as in Arobone & Sarkar (2010). In case $Ri1N$, with the same stratification but higher $Re_0 = 2400$, coherent dynamics are quite similar with vertical length scale associated with slicing remaining unchanged, but with far greater fine-scale structure in the braid region.

4.4.2 Rotating Unstratified Cases

Both high Re unstratified simulations with weak rotation ($Ri0A10$ and $Ri0C10$) exhibit a rapid transition to turbulence, with the anticyclonic case appearing considerably more unstable. The lower Re unstratified cases show clearer qualitative differences between cyclonic and anticyclonic cases. The $2\Omega_0 = -0.1$ case begins with quasi-vertical vortical structures, which shed coherent longitudinal structures until being completely destroyed by turbulent fluctuations. For $2\Omega_0 = -0.2$, the quasi-vertical vortices are almost immediately pinched off forming longitudinal structures, as in Métais *et al.* (1995), which then go turbulent and the flow gradually transitions into a fully turbulent state. The cyclonic $2\Omega_0 = 0.1$ case contains quasi-vertical structures that still shed longitudinal vortices, albeit they are far less commonplace than in the anticyclonic cases. Most shedding and destabilization in the cyclonic case occur later during vortex merging, perhaps indicative of elliptic instability.

4.4.3 Anticyclonic Rotation with Stratification

The coherent structures evolve differently among the stratified anticyclonic cases and even more so with respect to the non-rotating stratified case. Figure 4.6 shows a section of the coherent structures in four stratified cases with increasing anticyclonic rotation. In all cases, the barotropic instability develops leading to columnar vortex cores that subsequently deform. While (a) through (c) contain snapshots from roughly the same time into the simulation, (d) has a much earlier

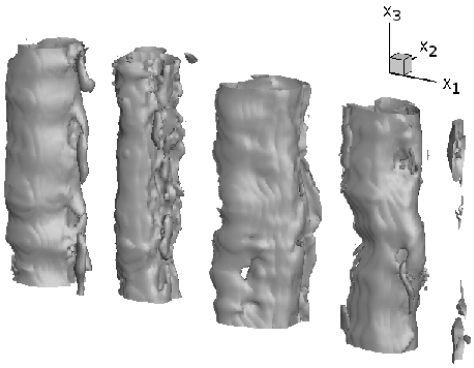

(a) Non-rotating case $Ri1N$ at t=12.3

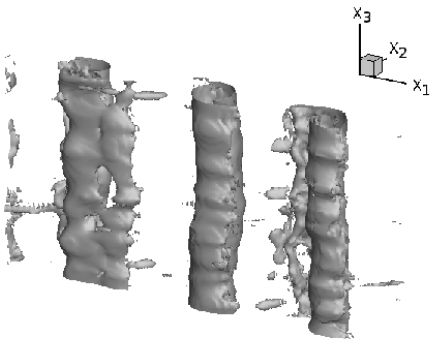

(b) $2\Omega_0 = -0.1$ case Ri1A10 shown where $2\Omega\,(t = 12.9) = -0.19$

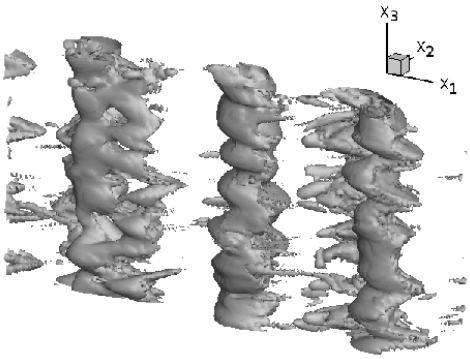

(c) $2\Omega_0 = -0.5$ case Ri1A2 shown where $2\Omega\,(t = 12.6) = -0.96$

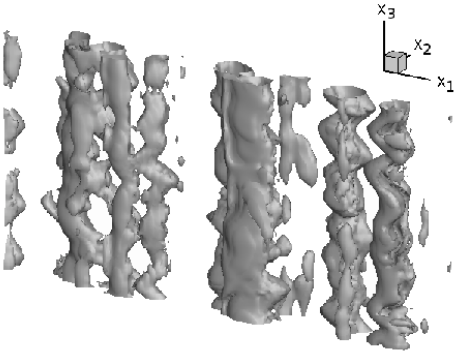

(d) $2\Omega_0 = -1$ case Ri1A1 shown where $2\Omega\,(t = 6.85) = -1.31$

Figure 4.6: Snapshots of vertical variation showing the early-time deformation of coherent, columnar structures in the stratified non-rotating and anticyclonic rotation cases. Isosurfaces of λ_2 for the subdomain $x_1 \in [0, 25]$, $x_2 \in [-12.5, 12.5]$, $x_3 \in [0, 12.5]$.

snapshot due to the more rapid deformation of the barotropic modes in the $2\Omega_0 = -1$ case. The fact that the initial deformation is largest in the $2\Omega_0 = -1$ case points to the importance of the *zero-absolute vorticity instability* identified in Part I. Figure 4.7 and 4.8 show coherent structures via horizontal and vertical snapshots, respectively, from the end of each simulation whose early-time structures were presented in Figure 4.6.

For $Ri1A10$, quasi-vertical structures form and quickly develop high vertical wavenumber deformations ($k_3 \approx 2.75$) as seen in Figure 4.6(b). The corrugated edges of the vortices, the so-called rib vortices of Kloosterziel *et al.* (2007*a*), interact

with nearby vortex cores and are then shed off as coherent braid structures that surround the quasi-vertical modes. The network of braid vortices grows throughout the remainder of the simulation obfuscating extraction of the behavior underneath from the λ_2 visualizations. Figure 4.7(b) is a horizontal snapshot that reveals fine-scale behavior throughout the coherent structures. In the lower Reynolds number case, $Ri1A10Re600$, deformations of the vortex cores are also observed with a similar wavenumber ($k_3 \approx 2.67$), but coherent braid structures do not emerge after the vortex edges are shed. It is important to note that the $k_1 = 0.44$ (dominant KH wavelength) inertial mode isn't excited until $2\Omega\,(t) \approx -0.2$. This may explain the low deformation of the vortices in Figure 4.6(b) compared to (c) and (d) which have more rapid rotation rates. The range of unstable k_1 values increases as the anticyclonic rotation rate increases as shown in figure 3 (b) and (e) from part I. Even though the $k_1 = 0$ mode is unstable for $-1 < 2\Omega < 0$, higher streamwise wavenumbers (in the shear layer high k_1 modes arise owing to the initial barotropic instability or later vortex interactions) require more rapid rotation for vertical destabilization.

The $Ri1A2$ case exhibits deformations in the quasi-vertical vortices, with a higher wavenumber ($k_3 \approx 4$). These deformations distort the quasi-vertical modes more than in the weaker anticyclonic rotation case, especially near the zero-absolute vorticity state, after which incoherent vorticity fluctuations appear around the 'zigzagging' vortex modes. Figure 4.6(c) shows the $Ri1A2$ case shortly before the zero absolute vorticity state, when $2\Omega\,(t) = -0.96$. Interestingly, coherent longitudinal braid structures emerge in case $Ri1A2$ shortly later, although not nearly as intensely as in $Ri1A10$, even though $2\Omega\,(t) < -1$ signifying that the flow is globally inertially stable. This is surprising given the fact that these structures have been traditionally associated with the inertial instability (Métais *et al.*, 1995; Kloosterziel *et al.*, 2007*a*). Case $Ri1A2Re600$ shows similar behavior as the higher Re case at early time, but incoherent fluctuations are less prevalent and the flow is quickly stabilized *without* the formation of coherent braid vortices. The resulting network of vortices interact minimally except when the separation distance is small enough that local shear is of comparable order to the coordinate system rotation

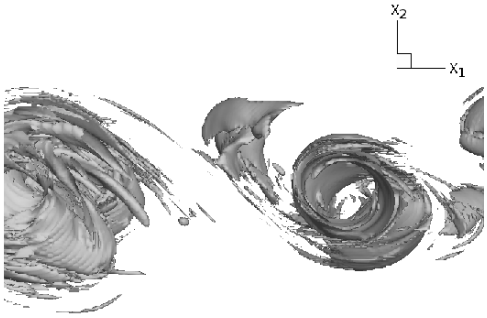

(a) Non-rotating case $Ri1N$ at t=68.9

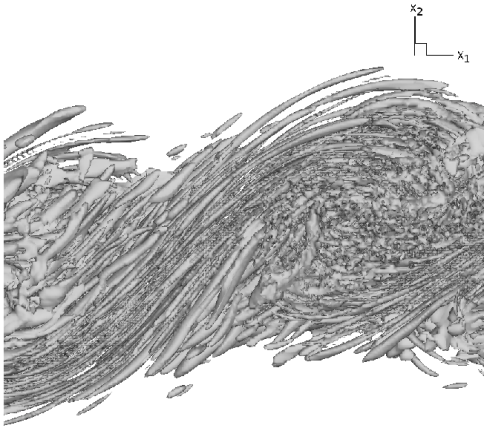

(b) $2\Omega_0 = -0.1$ case Ri1A10 shown where $2\Omega\,(t = 69.2) = -0.67$

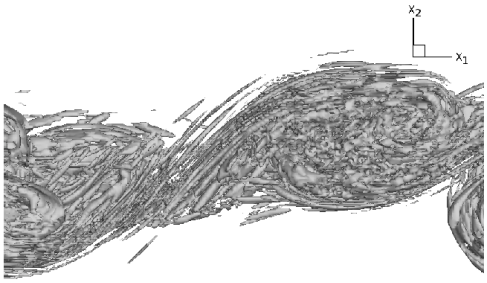

(c) $2\Omega_0 = -0.5$ case Ri1A2 shown where $2\Omega\,(t = 64.8) = -2.82$

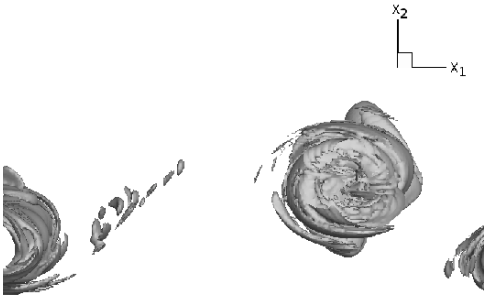

(d) $2\Omega_0 = -1$ case Ri1A1 shown where $2\Omega\,(t = 65.2) = -6.28$

Figure 4.7: Isosurfaces of λ_2 for the subdomain $x_1 \in [0, 25]$, $x_2 \in [-12.5, 12.5]$, $x_3 \in [0, 12.5]$ show the final coherent structures viewed in the negative x_3 direction.

rate.

High vertical wavenumber ($k_3 \approx 2.5$) deformations are also observed earlier in the $Rib1A1$ case (figure 4.6(d)), which deform the quasi-vertical modes quickly compared to the weaker anticyclonic cases. No significant small-scale incoherent structure emerges and vortex evolution is similar to that of $Ri1A2Re600$ at late time, where vortices advect passively and only interact significantly once they are in very close proximity with one another. The qualitative similarities between $Ri1A1$ (high rotation and high Re) and $Ri1A2Re600$ (moderate rotation and low Re) cases are likely due to the fact that the increased destabilization owing to moderate rotation in case $Ri1A2Re600$ is nearly offset by the increased stabilization of viscosity. At higher initial rotation, $2\Omega_0 = -1$, the coherent vortex cores in the lower Re case, $RibA1Re600$, evolved similarly as at higher Re except with smoother vorticity isocontours and less small scale content.

The structures tend to deform in the x_1-x_3 plane near the zero absolute vorticity state, $2\Omega(t) = -1$, for both $Ri1A2$ and $Ri1A1$. This corresponds to formation of small scale ω_2', consistent with the linearized inviscid evolution equations at the centerline for the zero absolute vorticity state, given in equation (5.2) of part I and here in equation (4.4). Streamwise density gradients efficiently generate ω_2' near this state due to the lack of influence of mean shear on the evolution equation for lateral vorticity fluctuations. Alternating filaments of ω_2' surround the columnar vortices and shear them rather quickly.

$$\frac{\partial \omega_1'}{\partial t} = \left(\frac{\langle s_{12} \rangle}{2} + \Omega_0 \right) \omega_2' - Ri_{b,0} \frac{\partial \rho'}{\partial x_2} \qquad \frac{\partial \omega_2'}{\partial t} = Ri_{b,0} \frac{\partial \rho'}{\partial x_1} \tag{4.4}$$

Vertical sections at later times show that coherent structures in the weakly and moderate anticyclonic cases $RiA10$ and $Ri1A2$ evolve quite differently from one another, but with a few key similarities. Both cases result in a network of thin coherent longitudinal vortices as seen in figures 4.8 (b) and (c), with the network being more prevalent in the weaker anticyclonic case with $2\Omega_0 = -0.1$. Initially, in both cases, vortices deform in a similar manner with a small vertical length scale. Later, however, the large quasi-vertical structures do not break apart

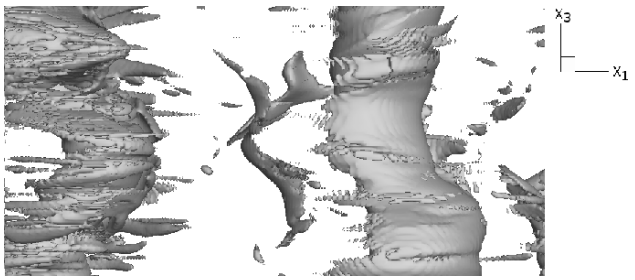

(a) Non-rotating case $Ri1N$ at t=68.9

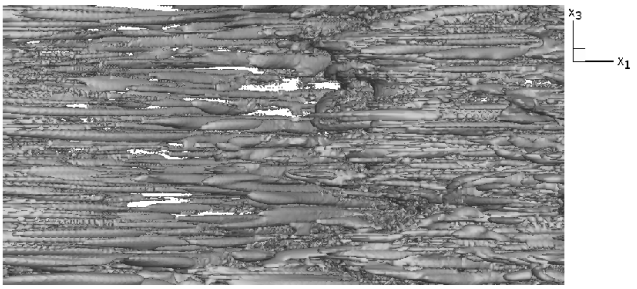

(b) $2\Omega_0 = -0.1$ case Ri1A10 shown where $2\Omega\,(t = 69.2) = -0.67$

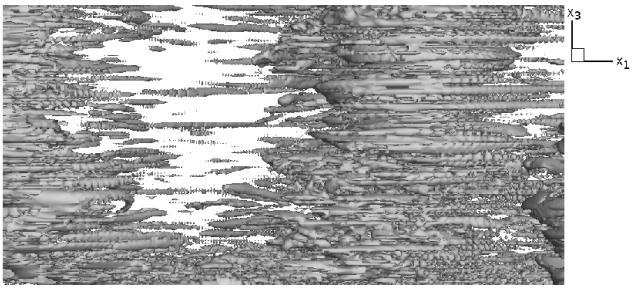

(c) $2\Omega_0 = -0.5$ case Ri1A2 shown where $2\Omega\,(t = 64.8) = -2.82$

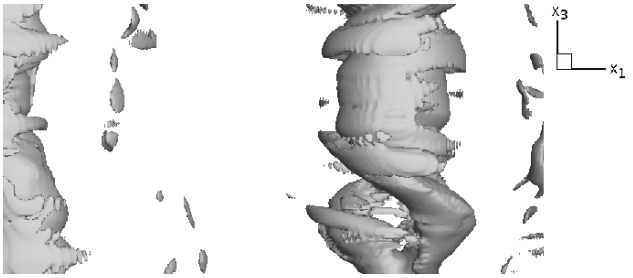

(d) $2\Omega_0 = -1$ case Ri1A1 shown where $2\Omega\,(t = 65.2) = -6.28$

Figure 4.8: Isosurfaces of λ_2 for the subdomain $x_1 \in [0, 25]$, $x_2 \in [-12.5, 12.5]$, $x_3 \in [0, 12.5]$ showing coherent structures in the stratified cases viewed in the positive x_2 direction.

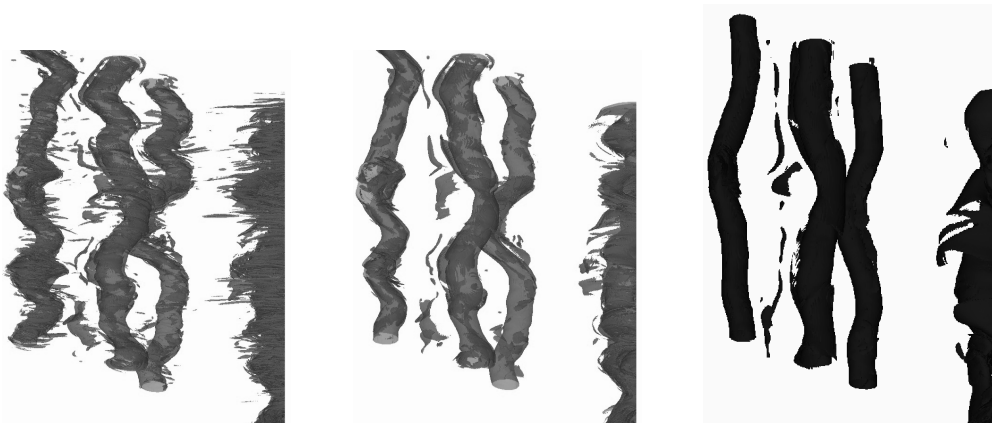

(a) $2\Omega_0 = 0$ case Ri1N where $2\Omega\,(t = 68.9) = 0$

(b) $2\Omega_0 = 0.1$ case Ri1C10 where $2\Omega\,(t = 69.1) = 0.65$

(c) $2\Omega_0 = 0.5$ case Ri1C2 where $2\Omega\,(t = 69.1) = 3.46$

Figure 4.9: Isosurfaces of λ_2 for the subdomain left of the x_2-x_3 midplane showing the effect of cyclonic rotation on coherent structures in the stratified cases.

in the weakly anticyclonic case, remaining columnar, while breaking apart in the moderate anticyclonic case with $2\Omega_0 = -0.5$.

4.4.4 Cyclonic Rotation with Stratification

The evolution of coherent vortices is very similar between the non-rotating stratified case and the cyclonic stratified cases, and strongly contrast against the anticyclonic cases. Vertical slicing is slightly less dramatic in the cyclonic cases than in the non-rotating case, but there is a clear one-to-one matching of vortical structures between the three cases throughout the duration of the simulations. Figure 4.9 (a), (b) and (c) illustrate these points, clearly showing coherent structures at the end of each simulation. The cleaner nature of the coherent structures in the cyclonic cases is also noteworthy.

4.5 Vortical Signature of Instabilities

The linear analysis of part I suggests that the inertial instability and zero absolute vorticity mechanism generate horizontal vorticity fluctuations in distinct

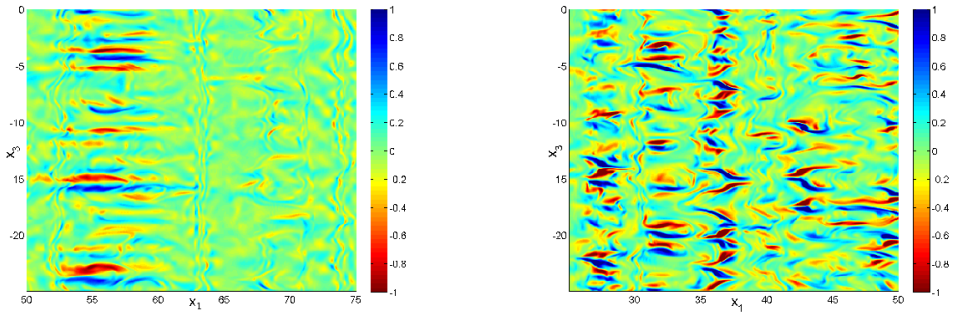

(a) $2\Omega_0 = -0.1$ case Ri1A10 where $2\Omega\,(t = 21.89) = -0.26$

(b) $2\Omega_0 = -0.5$ case Ri1A2 where $2\Omega\,(t = 13.6) = -1.01$

Figure 4.10: Laplacian filtered ω_2 fluctuations given for a segment of the x_1-x_3 mid-plane illustrating differences between instabilities in the (a) weak anticyclonic and (b) moderate anticyclonic cases.

manners. Figure 4.10 (a) and (b) illustrate the differences between the non-linear evolution of the inertial instability and the zero absolute vorticity instability. Figure 4.10 (a) contains only thin sheet-like vortex structures associated with the inertial instability, while 4.10 (b) contains both thin sheet-like structures and arrays of alternating vorticity which are prevalent near the zero-absolute vorticity state. The sheet-like structures take more time to induce local shear instability than the vortex arrays which quickly overturn generating small-scale vorticity.

Case $Ri1A10$ experiences significant destabilization owing to the nonlinear evolution of the inertial instability as illustrated in Figure 4.11. The inertial instability manifests as coherent longitudinal vortices in the braid region, as seen in the previous section, and thin sheet-like vortex structures in the core region. These sheet-like vortex structures are susceptible to roll-up at later times as seen in Figure 4.11, which shows the transition from sheet-like structures of ω_2 to KH billows in several locations, which are circled. Figure 4.11 (a) and (b) correspond to $2\Omega\,(t) = -0.43$ and $2\Omega\,(t) = -0.56$, respectively, implying that rollup occurs near the most linearly unstable state of $2\Omega\,(t) = -0.5$.

The horizontal vorticity components show dramatic differences with respect to system rotation in the stratified simulations, and are by far the most active in the $Ri1A2$ and $Ri1A10$ cases. Vertical layering is most dramatic in $Ri1A2$ at later

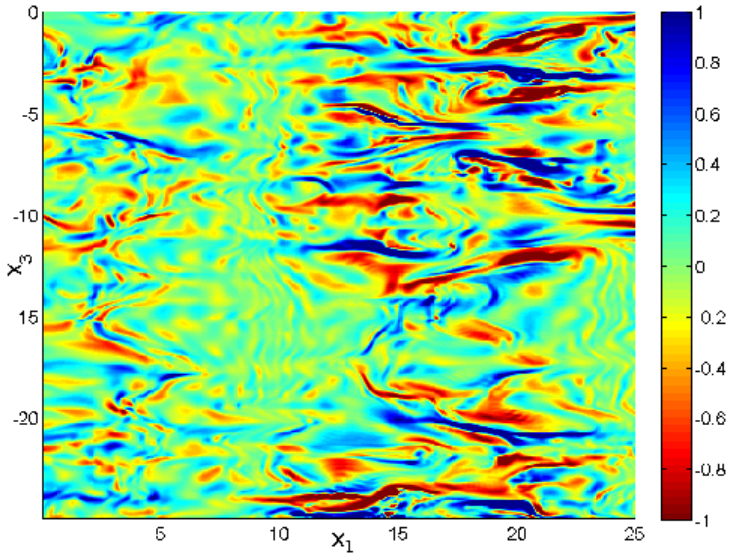

(a) $2\Omega\,(t = 48.94) = -0.40$

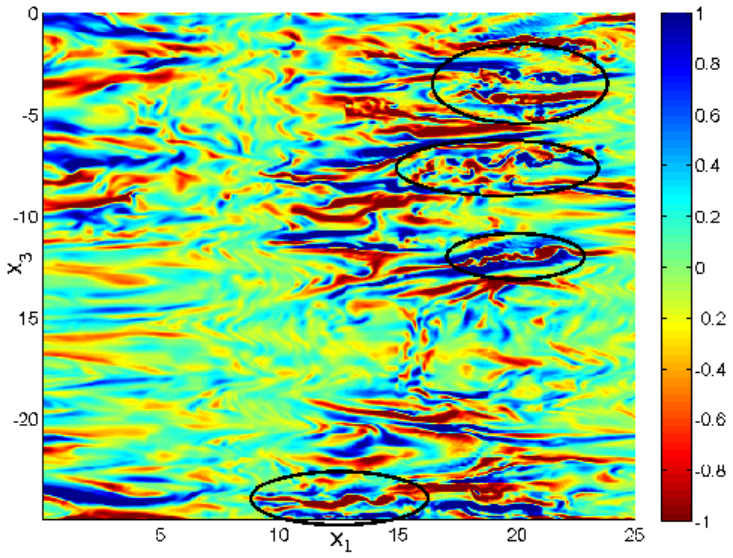

(b) $2\Omega\,(t = 61.22) = -0.56$

Figure 4.11: Plots of Laplacian filtered ω_2 from the Ri1A10 case with $2\Omega_0 = -0.1$ showing development of fine-scale KH instabilities and vortical structure as the flow passes through the most inertially unstable regime ($2\Omega\,(t) = -0.5$).

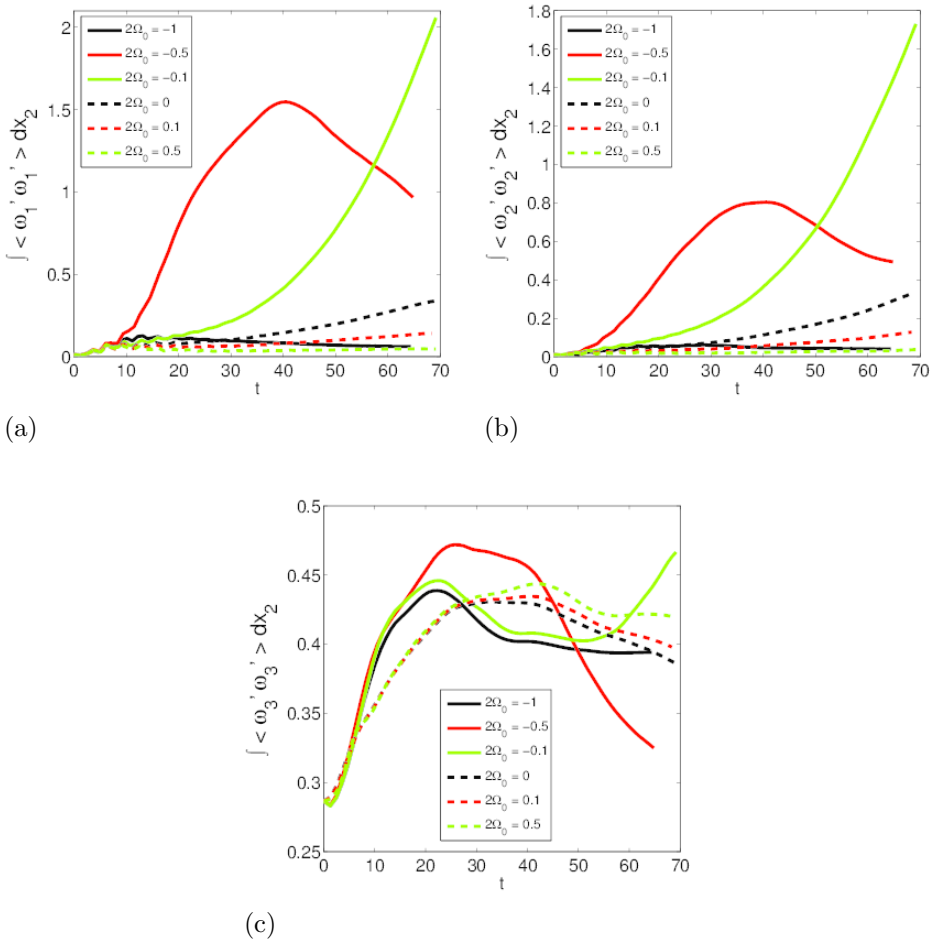

Figure 4.12: Temporal evolution of integrated enstrophy components in stratified cases where $Ri_{b,0} = 1$ and $Re_0 = 2400$.

times, even though the effect of rotation is stabilizing, while the vorticity fields appear most disordered in $Ri1A10$.

4.6 Fluctuating Enstrophy Evolution

Figure 4.12 shows the evolution of fluctuating enstrophy components in each of the high Re stratified cases. When $2\Omega_0 = 0.1$, 0.5 and -1, enstrophy is primarily vertical, while horizontal enstrophy dominates for $2\Omega_0 = -0.1$ and -0.5. In order to quantify the processes responsible for modifying enstrophy components, fluctuating enstrophy budgets are computed. Equations are derived for the evo-

lution of x_1-x_3 plane-averaged fluctuating enstrophy components and given below for the horizontal shear layer (no summation over Greek indices).

$$\begin{aligned}\frac{\partial \langle \omega'_\alpha \omega'_\alpha \rangle}{\partial t} &= -2 \langle \omega'_\alpha u'_2 \rangle \frac{\partial \langle \omega_\alpha \rangle}{\partial x_2} - \frac{\partial \langle \omega'_\alpha \omega'_\alpha u'_2 \rangle}{\partial x_2} + 2 \left(\langle \omega_3 \rangle + 2\Omega_0 \right) \langle \omega'_\alpha s'_{\alpha 3} \rangle \\ &\quad +2 \left\langle \omega'_\alpha \omega'_j \right\rangle \langle s_{\alpha j} \rangle + 2 \left\langle \omega'_\alpha \omega'_j s'_{\alpha j} \right\rangle + \epsilon_{\alpha j 3} 2\Omega_0 \left\langle \omega'_\alpha \omega'_j \right\rangle \\ &\quad + \frac{1}{Re} \frac{\partial^2 \langle \omega'_\alpha \omega'_\alpha \rangle}{\partial x_j \partial x_j} - \frac{2}{Re} \left\langle \frac{\partial \omega'_\alpha}{\partial x_j} \frac{\partial \omega'_\alpha}{\partial x_j} \right\rangle - \epsilon_{\alpha j 3} 2 Ri_b \left\langle \omega'_\alpha \frac{\partial \rho'}{\partial x_j} \right\rangle \end{aligned} \quad (4.5)$$

The physical meaning of each term is explained below.

Rate of change of fluctuating enstrophy (DDT) :

$$\frac{\partial\langle\omega'_\alpha\omega'_\alpha\rangle}{\partial t}$$

Production of fluctuating enstrophy (PROD) :

$$-2\left\langle\omega'_\alpha u'_2\right\rangle\frac{\partial\langle\omega_\alpha\rangle}{\partial x_2}$$

Transport of fluctuating enstrophy by velocity fluctuations (TR) :

$$-\frac{\partial\left\langle\omega'_\alpha\omega'_\alpha u'_2\right\rangle}{\partial x_2}$$

Stretching/tilting of mean absolute vorticity by fluctuating strain (VS_MV) :

$$2\left(\langle\omega_3\rangle+2\Omega_0\right)\left\langle\omega'_\alpha s'_{\alpha 3}\right\rangle$$

Stretching/tilting of fluctuating vorticity by mean strain (VS_MS) :

$$2\left\langle\omega'_\alpha\omega'_j\right\rangle\left\langle s_{\alpha j}\right\rangle$$

Stretching/tilting of fluctuating vorticity by fluctuating strain (VS_F) :

$$2\left\langle\omega'_\alpha\omega'_j s'_{\alpha j}\right\rangle$$

Effect of coordinate system rotation (ROT) :

$$\epsilon_{\alpha j3}2\Omega_0\left\langle\omega'_\alpha\omega'_j\right\rangle$$

Viscous diffusion of enstrophy fluctuations (DIFF) :

$$\frac{1}{Re}\frac{\partial^2\langle\omega'_\alpha\omega'_\alpha\rangle}{\partial x_j\partial x_j}$$

Viscous dissipation of enstrophy fluctuations (DISS) :

$$-\frac{2}{Re}\left\langle\frac{\partial\omega'_\alpha}{\partial x_j}\frac{\partial\omega'_\alpha}{\partial x_j}\right\rangle$$

Fluctuating baroclinic term (BC) :

$$-\epsilon_{\alpha j3}2Ri_b\left\langle\omega'_\alpha\frac{\partial\rho'}{\partial x_j}\right\rangle$$

The transport of fluctuating enstrophy and viscous diffusion terms integrate over the domain to zero when there are no boundary fluxes and are not discussed. In our analysis we often combine the stretching of fluctuating vorticity by mean strain term (VS_MS) with the coordinate system rotation term (ROT) to reduce clutter in the enstrophy component budgets. VS_MS is a source term while ROT transfers fluctuating enstrophy between horizontal components. In some cases the

nonlinear vortex stretching (VS_F) term is merged with DISS, also to reduce clutter, this term can be thought of as the imbalance between dissipation and enstrophy transfers from larger to smaller scales. Large magnitudes of VS_F and DISS are suggestive of strong non-linearity, a forward enstrophy cascade, and turbulence.

Initially, we focus our attention on vertical fluctuating enstrophy budgets, which are not directly influenced by buoyancy. Vertical enstrophy budgets are plotted in Figure 4.13 for stratified cases with $2\Omega_0 = 0$, -0.1, -0.5 and -1. Common features are observed at late time between the $2\Omega_0 = -1$ case and the non-rotating and cyclonic (not shown, but similar to non-rotating) cases. Here, the dominant balance is between PROD and DISS. This partially explains why snapshots of vertical vorticity (not shown) are significantly cleaner in these cases than in the anticyclonic cases with weaker rotation. Nonlinear stretching and tilting play a far greater role in the evolution of vertical enstrophy fluctuations in the weak and moderate anticyclonic stratified cases, even at later time when $2\Omega\,(t) < -1$. Thus, for cases $Ri1A10$ and $Ri1A2$ there are time periods when the budget is dominated by VS_F and DISS terms, but in the $Ri1A1$, $Ri1C10$ and $Ri1N$ cases VS_F never dominates.

The $2\Omega_0 = -0.5$ case passes through $2\Omega(t) = -1$ corresponding to zero absolute vorticity. Through figures 4.14-4.16 we demonstrate that the baroclinic term (BC) plays an important role in maintaining vorticity fluctuations beyond the zero absolute vorticity state despite the inertial stability of the flow during this stage.

Figure 4.14 shows local lateral fluctuating enstrophy ($\langle\omega_2'\omega_2'\rangle$) budgets from the low and high Re_0 stratified $2\Omega_0 = -0.5$ cases at the inflection point, focusing on early time evolution. Both plots show the BC term out of phase with the linear VS_MV and VS_MS (actually VS_MS + ROT) terms, transport advecting enstrophy away from the centerline, and VS_F (actually VS_F + DISS) implying a cascade of enstrophy from large scales to small. The zero absolute vorticity state is reached in the high Re case (Figure 4.14 (b)) when $t \approx 13.4$. Shortly after, when $t \approx 14$, baroclinic torque (BC) changes sign in the $\langle\omega_2'\omega_2'\rangle$ budget, implying destabilization of lateral fluctuating enstrophy by density fluctuations.

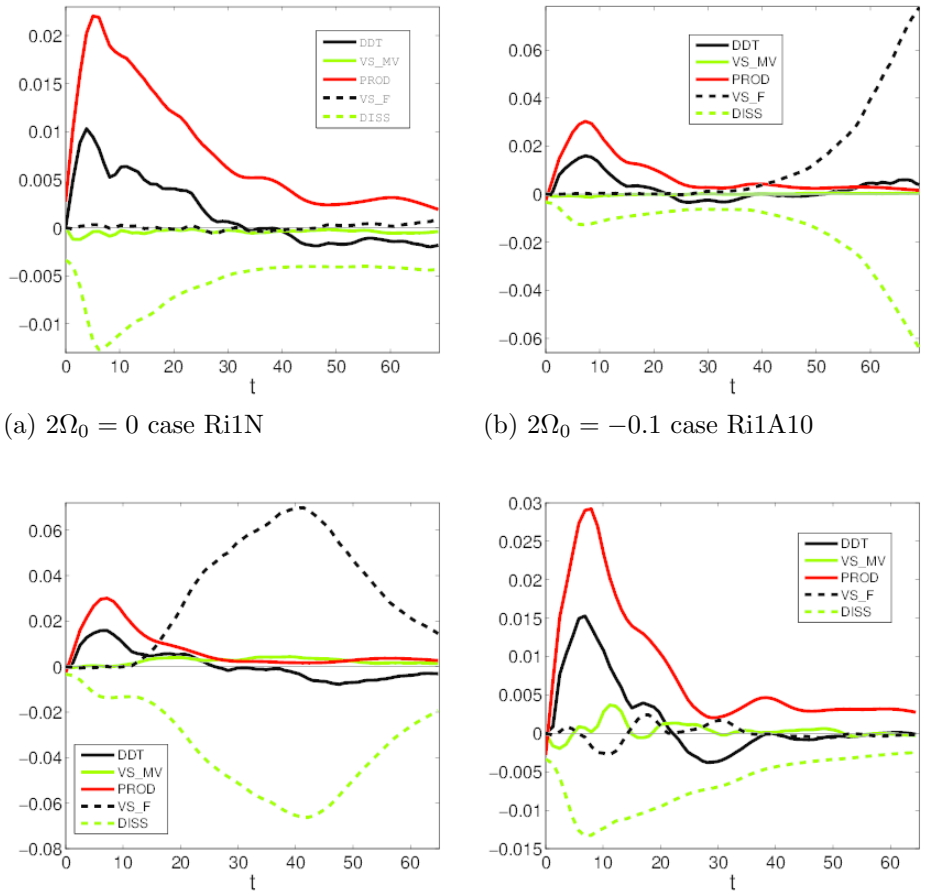

(a) $2\Omega_0 = 0$ case Ri1N

(b) $2\Omega_0 = -0.1$ case Ri1A10

(c) $2\Omega_0 = -0.5$ case Ri1A2

(d) $2\Omega_0 = -1$ case Ri1A1

Figure 4.13: Temporal evolution of integrated vertical enstrophy budgets in stratified cases where $Ri_{b,0} = 1$. The $2\Omega_0 = 0.1$ and $2\Omega_0 = 0.5$ cases are very similar to (a) and not shown.

This is consistent with the dynamics of the zero absolute vorticity mode in figure 11 of part I, where density gradients act against ω_1' while acting to strengthen ω_2'. Interestingly, we see the BC, VS_MV and VS_MS (actually VS_MS + ROT in Figure 4.14) terms change signs in the local $\langle \omega_2' \omega_2' \rangle$ budget at almost the same time ($t \approx 13.4$ in Figure 4.14 (b)). The VS_MV and VS_MS (VS_MS + ROT in Figure 4.14) terms are exactly zero when local absolute vorticity is zero because $\langle s_{12} \rangle - \Omega_0 = -\frac{1}{2} \left(\langle \omega_3 \rangle + 2\Omega_0 \right) = 0$. The DDT term of Figure 4.14 (b) shows a considerable delay in crossing the zero value relative to Figure 4.14 (a), i.e., stabilization of lateral enstrophy is delayed at higher Reynolds number. Perhaps at still higher Re, destabilization could be delayed even further into the inertially stable regime.

In Figure 4.15, lateral profiles of $\langle \omega_1' \omega_1' \rangle$ and $\langle \omega_2' \omega_2' \rangle$ budgets are shown for the stratified $2\Omega_0 = -0.5$ case shortly after the zero absolute vorticity state. Although the nonlinear vortex stretching term (VS_F) is dominant in the budget for $\langle \omega_2' \omega_2' \rangle$, it is almost cancelled by the other non-baroclinic terms, particularly the dissipation. Consequently, the rate of change curve (DDT) in Figure 4.15 for lateral fluctuating enstrophy nearly follows the baroclinic (BC) term, which was predicted by equation (4.4), which was derived assuming small horizontal gradients, zero absolute vorticity, and neglected nonlinearity and viscosity.

Interestingly, in Figure 4.16 (a) and (b), nonlinear vortex stretching and tilting are far more important in lateral enstrophy evolution than streamwise enstrophy, where stretching and tilting is nearly zero around and before the zero absolute vorticity state. For weak and moderate anticyclonic rotation rates there are times when baroclinicity is a net source of horizontal enstrophy, specifically throughout much of the $2\Omega_0 = -0.5$ case. The DDT term in the lateral enstrophy budget in Figure 4.16 (b) suggests peak destabilization occurring in the stratified $2\Omega_0 = -0.5$ case when $35 \lesssim t \lesssim 40$ or $2\Omega(t) \sim -1.75$. In an attempt to better understand why enstrophy fluctuations grow so far into the inertially stable regime, equation (4.4) is manipulated to obtain the following evolution equation for fluctuating lateral enstrophy, neglecting the influence of stratification :

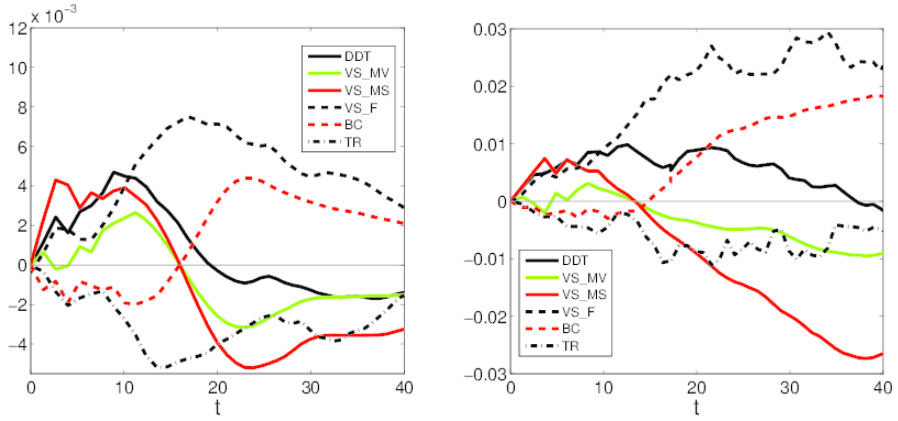

(a) $Re_0 = 600$ case Ri1A2Re600 (b) $Re_0 = 2400$ case Ri1A2

Figure 4.14: Temporal evolution of the $\langle \omega_2' \omega_2' \rangle$ budget from the anticyclonic cases with $2\Omega_0 = -0.5$, $Ri_{b,0} = 1$. The budget is calculated at the centerline and the plot zooms in on the early evolution.

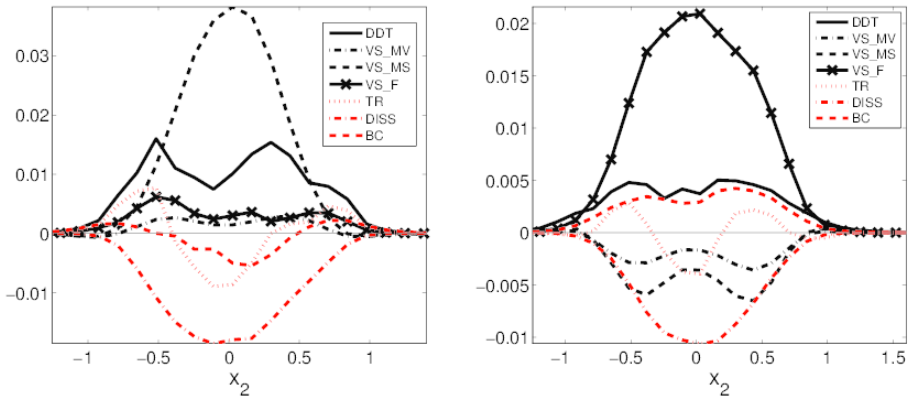

(a) $\langle \omega_1' \omega_1' \rangle$ budget (b) $\langle \omega_2' \omega_2' \rangle$ budget

Figure 4.15: Enstrophy component budgets from the $2\Omega_0 = -0.5$, $Ri_{b,0} = 1$ case Ri1A2 shown shortly after the zero absolute vorticity state. Here, $t = 18.08$ and $2\Omega(t) \approx -1.12$.

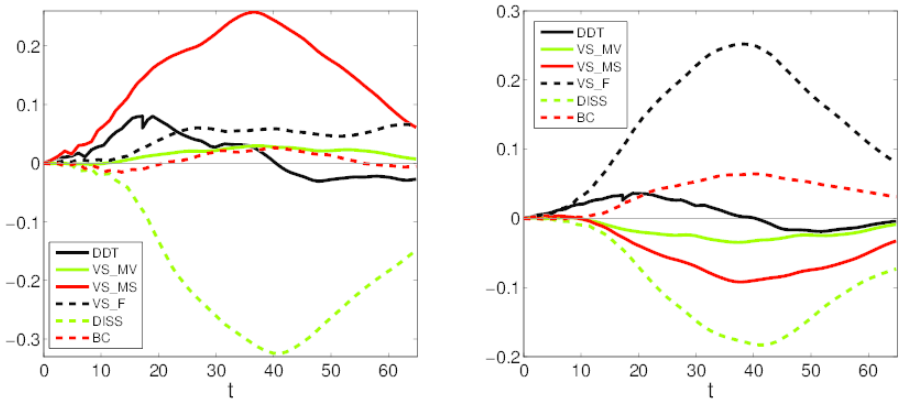

(a) $\langle \omega_1' \omega_1' \rangle$ budget (b) $\langle \omega_2' \omega_2' \rangle$ budget

Figure 4.16: Temporal evolution of integrated horizontal enstrophy budgets for the moderate anticyclonic case Ri1A2 with $2\Omega_0 = -0.5$ and $Ri_{b,0} = 1$. The rate of change and baroclinic torque terms have been filtered to lessen the influence of N oscillations.

$$\frac{\bar{D}^2}{\bar{D}t^2}\left[\langle \omega_2' \omega_2' \rangle\right] \quad = \quad -4\Omega_0 \left(2\Omega_0 + \langle \omega_3 \rangle\right) \langle \omega_2' \omega_2' \rangle \tag{4.6}$$

We concentrate on fluctuating lateral enstrophy because it begins to decay before both the fluctuating streamwise enstrophy and the $\langle \omega_1' \omega_2' \rangle$ correlation. Understanding the mechanism responsible for delayed decay of lateral fluctuating enstrophy may explain why dissipation and nonlinearity remain strong so long after passing through the absolute zero vorticity state. Based on the present simulation data, mean centerline vorticity may be approximated by $\langle \omega_3 \rangle (t) \approx (t/13 + 1)^{-1}$, and lateral fluctuating enstrophy may be approximated as growing linearly with time. Integrating equation (4.6) from the beginning of the simulation until time t^* and setting the result equal to zero gives the time when $\langle \omega_2' \omega_2' \rangle$ reaches peak magnitude.

$$\int_0^{t^*} 2\left(-\frac{1}{2} + \frac{1}{t/13+1}\right) t dt = 0 \tag{4.7}$$

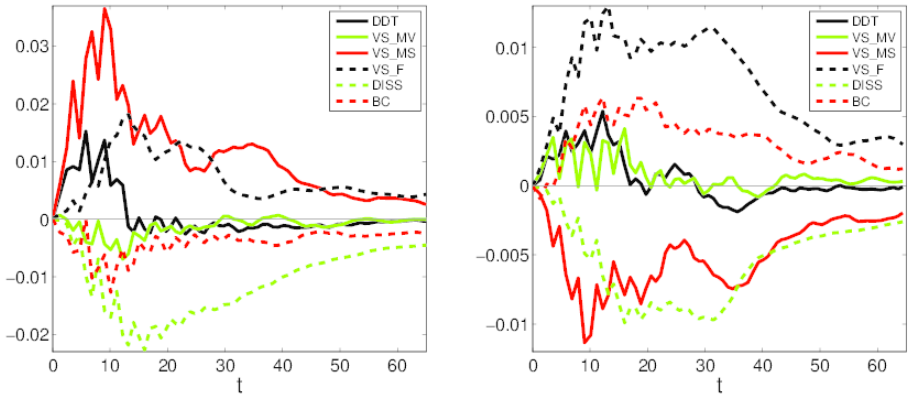

(a) $\langle \omega_1' \omega_1' \rangle$ budget (b) $\langle \omega_2' \omega_2' \rangle$ budget

Figure 4.17: Temporal evolution of integrated horizontal enstrophy budgets in the rapid anticyclonic case Ri1A1 where $2\Omega_0 = -1$ and $Ri_{b,0} = 1$. The rate of change and baroclinic torque terms have been filtered to lessen the influence of N oscillations.

Equation (4.7) is satisfied when $t^* \approx 21.1$, long before the $t^* \approx 37$ when $\langle \omega_2' \omega_2' \rangle$ is found to achieve its peak in case $Ri1A2$ as discerned by where the rate of change curve crosses the time axis in Figure 4.14 (b). Thus, destabilization continues beyond the time predicted by linear, unstratified analysis. An interesting point to note is that the baroclinic and rate of change terms in the lateral fluctuating enstrophy budget in Figure 4.14 (b) cross when $t \approx 21$, i.e., at this time, the increase in horizontal enstrophy is entirely due to the production by baroclinicity (BC). The BC term continues to be positive and grow after $t = 21$ while the sum of all the other terms continues to be negative and a sink. Clearly, the generation of ω_2 via baroclinic torque once $2\Omega\,(t) \gtrsim -1$ helps explain the delayed stabilization of horizontal enstrophy.

4.6.1 Rapid Rotation Regime

Figure 4.17 shows the streamwise and lateral fluctuating enstrophy budgets throughout the duration of case $Ri1A1$ with initial $2\Omega_0 = -1$. The nondimensional rotation rate, $2\Omega(t)$, increases by a factor of 7 during the simulation. Relative to the moderate rotation rate case with initial $2\Omega_0 = -0.5$, the terms in the

enstrophy budget are smaller in this case by almost an order of magnitude. When rotation is strong ($2\left|\Omega\left(t\right)\right| \gg 1$) the baroclinic terms are out of phase with the terms corresponding to stretching by mean strain and coordinate rotation. This is a consequence of flow in thermal wind (geostrophic and hydrostatic) balance, which when applied to the momentum equations gives

$$2\Omega_0 \frac{\partial u_1'}{\partial x_3} \sim Ri_{b,0} \frac{\partial \rho'}{\partial x_2}, \qquad -2\Omega_0 \frac{\partial u_2'}{\partial x_3} \sim Ri_{b,0} \frac{\partial \rho'}{\partial x_1},$$

$$2\Omega_0 \left(s_{13}' + r_{13}'\right) \sim Ri_{b,0} \frac{\partial \rho'}{\partial x_2}, \qquad 2\Omega_0 \left(s_{23}' + r_{23}'\right) \sim -Ri_{b,0} \frac{\partial \rho'}{\partial x_1},$$

$$\underbrace{2\Omega_0 \omega_1' s_{13}'}_{A1} + \underbrace{\Omega_0 \omega_1' \omega_2'}_{B1} \sim \underbrace{Ri_{b,0} \omega_1' \frac{\partial \rho'}{\partial x_2}}_{C1}, \qquad \underbrace{2\Omega_0 \omega_2' s_{23}'}_{A2} - \underbrace{\Omega_0 \omega_1' \omega_2'}_{B2} \sim \underbrace{-Ri_{b,0} \omega_2' \frac{\partial \rho'}{\partial x_1}}_{C2}.$$

When rotation is rapid, the tilting of planetary vorticity terms (A1 and A2) tend to be small relative to the coordinate system rotation terms (B1 and B2). The rotation term acts to transfer enstrophy from one horizontal component to another, but does not generate or destroy enstrophy. Due to balance with the rotation term in rapidly rotating strongly stratified flow, baroclinic torque also acts to transfer enstrophy from one horizontal component to the other. In the present flow, $\omega_1'\omega_2'$ tends to be positive because mean strain increases horizontal enstrophy via vortex stretching, as in term VS_MS in equation (4.5). Baroclinicity therefore should transfer from streamwise to lateral enstrophy as observed here, consistent with figure 12 of part I with negative rotation rate.

4.7 Quantifying Fluctuations

The dynamics of the stratified cases differ greatly from one another owing to differences in system rotation. Significant disorder is observed in the vorticity and scalar (not shown) fields when rotation is moderate and anticyclonic. In this section, the primary focus will be on quantitative differences between the stratified high *Re* cases with an emphasis on metrics that quantify the nature of turbulence. For the stratified cases, the centerline buoyancy Reynolds number,

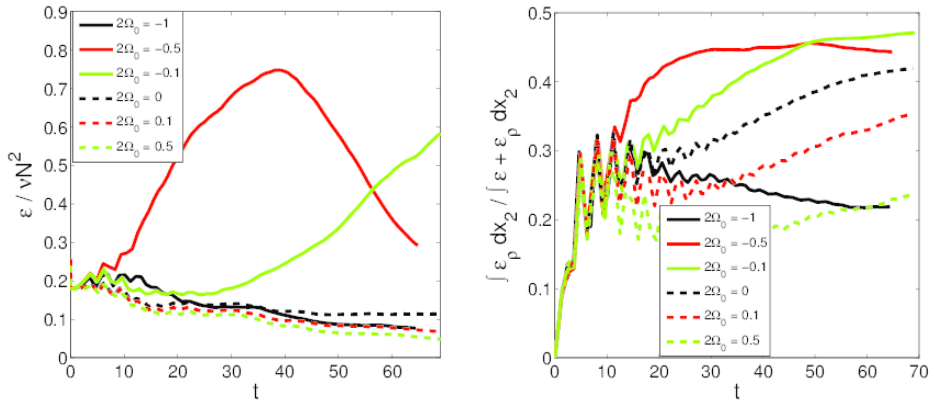

(a) (b)

Figure 4.18: Plot of (a) buoyancy Reynolds number and (b) the ratio of dissipation of potential energy to dissipation of both kinetic and potential energies versus time for the stratified cases.

$Re_B = \varepsilon(x_2 = 0)/\nu N^2$ where $\epsilon = 2\nu\left\langle s'_{ij}s'_{ij}\right\rangle$, is plotted in Figure 4.18. The $2\Omega_0 = -0.1$ and $2\Omega_0 = -0.5$ cases are much more dissipative, but the buoyancy Reynolds number does not exceed unity. The $2\Omega_0 = -1$, $2\Omega_0 = 0.1$ and $2\Omega_0 = 0$ cases have similar magnitudes of Re_B with the $2\Omega_0 = -1$ and $2\Omega_0 = 0.1$ cases being remarkably similar. The low values of Re_B in the weak and moderate anticyclonic cases contrast with evidence presented in the prior sections that the flow in these cases has a plethora of small scale activity and that nonlinear terms are very important in enstrophy budgets.

Although values of Re_B are quite low, in Figure 4.18 (b) we see that dissipation of potential energy, ε_ρ, is the same order as dissipation of kinetic energy, ε, for the weak and moderate anticyclonic stratified cases. The high values are suggestive of high mixing efficiency for these flows, while lower mixing efficiency is expected for cyclonic and/or rapid rotation. The values for the non-rotating, stratified case at $Re_0 = 2400$ are greater than the lower Re_0 stratified case of Basak & Sarkar (2006) as well as case $Ri1NRe600$ with $Re_0 = 600$ simulated here. Evidently, strongly stratified non-rotating flows can also have strong vertical mixing if the Reynolds number is sufficiently large as hypothesized previously (Riley & de Bruyn Kops, 2003). We also explored the behavior of Sk, the skewness of

$\partial u_1'/\partial x_1$, which gives information relating to vortex stretching and energy transfer between scales. Note that isotropic, unstratified turbulence has $Sk \sim -0.45$. For $Ri0A10$ and $Ri1A10$ the skewness is observed to be -0.44 and -0.29, respectively, at the end of the simulation. Skewness of $Ri1N$ and $Ri1A1$ are very different taking the values 0.16 and 0.38, respectively. Therefore it is reasonable to conclude from the specific metric of skewness of $\partial u_1'/\partial x_1$ that, at the high stratifications considered here, the high rotation cases are not turbulent in the sense of three-dimensional turbulence in a homogenous fluid. The anticyclonic cases with weak rotation, however, are most likely turbulent in that sense.

The quasi-two-component nature of the fluctuations in the stratified cases is shown in Figure 4.19 (a)-(b). Vertical turbulent kinetic energy (TKE) is typically about two orders of magnitude smaller than horizontal TKE. The largest vertical TKE is observed for the weakly and moderately anticyclonic cases, while the rapidly rotating anticyclonic case exhibits the least vertical TKE. Other quantities suggestive of turbulence are viscous dissipation and vortex stretching which are not shown, but give a general trend of strong destabilization initially for the anticyclonic cases with strong stabilization later in the $2\Omega_0 = -1$ case.

Figure 4.20 shows the streamwise spectra at the end of each simulated case. As stated in section 2, initial spectra are identical in all cases. In general, the unstratified cases have the most energy at the smallest scales and the stratified non-rotating, cyclonic and strongly anticyclonic cases contain the least. The weaker anticyclonic stratified cases have small scale energy at levels between the unstratified and other stratified cases. Case $Ri1A2$ shows less energy in the intermediate wavenumbers than the more stable cases while still having significant energy in the smallest scales. This is likely due to the stabilizing effect of rotation on larger scales once $t \gtrsim 13$ and active fine scales maintaining energy at the expense of the intermediate scales.

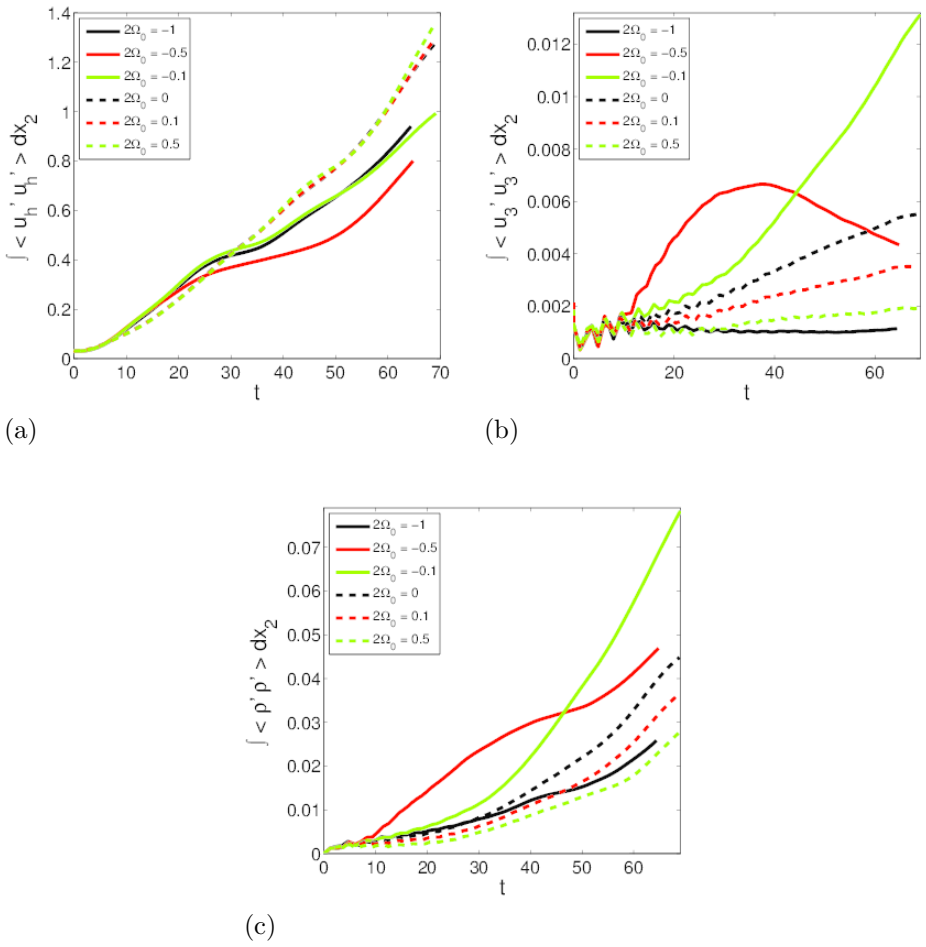

Figure 4.19: Plots showing integrated components of (a) horizontal and (b) vertical turbulent kinetic energy in addition to (c) density variance.

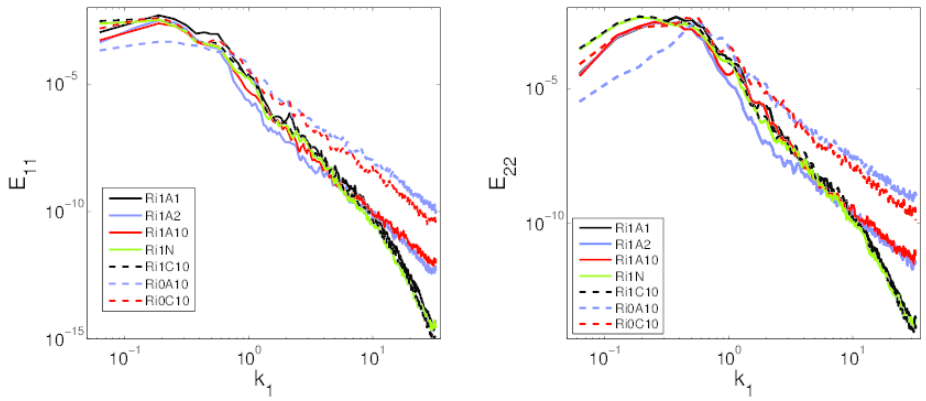

(a) (b)

Figure 4.20: Plots of streamwise spectra at the end of each high Re_0 simulation.

4.8 Conclusion

Part 1 investigated the three-dimensional instability of a stratified and rotating horizontally oriented shear layer with a hyperbolic tangent velocity profile. Part 2 is an exploration of the nonlinear evolution of the shear layer for $|2\Omega| \sim O(1)$ focusing on strongly stratified flow with $Ri_b(t) \geq 1$. The cases have a Reynolds number based on vorticity thickness, initially at $Re_0 = 2400$, that increases to approximately $Re = 16,800$ at the end of the simulations, and are simulated using nearly 1 billion grid points. Although, cases with a lower $Re_0 = 600$ are also simulated, the bulk of the presented results pertain to the higher-Re series.

Visualizations of coherent vortex dynamics demonstrated that the qualitative differences between anticyclonic and cyclonic rotation at weak rotation persist in cases with strong stratification and also showed the importance of the buoyancy-induced instability, a modified barotropic mode at zero absolute vorticity, that was found in Part I. During the initial evolution, the quasi-vertical vortices deform the fastest in the state with zero absolute vorticity at the centerline, and next fastest in the $2\Omega_0 = -0.5$ case. This implied that the loss of cyclostrophic balance when $2\Omega(t) = -1$ is more destabilizing to vortex cores than the initial influence of the inertial instability. The stratified $2\Omega_0 = -1$ case shows deformation of the barotropic modes along the x_1-x_3 plane, consistent with the formation of lateral

vorticity, ω_2, by baroclinic effects when the absolute vorticity is zero. Vorticity dynamics show secondary KH shear instabilities during the evolution of the inertial instability when $2\Omega(t) \approx -0.5$. Also, the zero absolute vorticity instability possesses a vorticity signature distinct from the inertial instability.

As the $2\Omega_0 = -0.1$ and $2\Omega_0 = -0.5$ cases progressed, a network of braid vortices formed and remained throughout the duration of both cases, even though $2|\Omega(t)|$ attained values as large as 2.7. The cyclonic rotation cases with $2\Omega_0 = 0.1$ and $2\Omega_0 = 0.5$ did not show such braid vortices and, instead, exhibited behavior very similar to the non-rotating case, but with vertical variability suppressed with increasing cyclonic rotation. The simulations at $Re_0 = 600$ and $Ri_{b,0} = 1$ exhibit initial deformation of the vortex cores similar to that at higher Re but, in strong contrast, do not show development of a network of braid vortices.

The shear layer thickens in the cross-stream direction owing to barotropic instabilities and turbulence. In the cases without stratification and with anticyclonic rotation, the thickening of the shear layer reduces to zero when the mean absolute vorticity approaches zero, consistent with the finding of Métais *et al.* (1995) and the arguments of Kloosterziel *et al.* (2007*a*). In contrast, the stratified case continues to thicken beyond the zero absolute vorticity state. The enhanced horizontal stirring by the quasi-2D dynamics in the stratified case combined with the presence of the zero absolute vorticity instability and associated baroclinic generation of enstrophy fluctuations allows continued reduction of horizontal mean shear by turbulent fluctuations.

Fluctuating enstrophy statistics elucidated dynamically distinct features of the various rotation regimes. Horizontal enstrophy dominated in anticyclonic cases with weak rotation ($2\Omega_0 = -0.1, -0.5$). Generation of horizontal enstrophy by nonlinear vortex stretching was substantial relative to the other terms in all cases, generation by vertical vortex stretching was only significant for intermediate rotation rates ($-0.5 \gtrsim 2\Omega(t) \gtrsim -3$). Baroclinic torque changed from a sink to a source of ω_2' fluctuations immediately after passing through the zero-absolute vorticity state, as expected from the behavior of linear barotropic modes in part I. Examination of the balance of terms in the transport equation for ω_2' shows

the important role of baroclinic production in allowing vorticity fluctuations to intensify after passing into the inertially stable regime.

The simulations are diagnosed for the state of velocity fluctuations. While the enstrophy budgets indicate that the flow is turbulent, buoyancy Reynolds numbers are very low, never exceeding unity even for the most unstable stratified cases. Mixing efficiency, inferred from dissipation of TKE and TPE, tends towards values on the order of 45% in the high Reynolds number, stratified series when rotation is destabilizing, somewhat smaller values in the case without rotation, and significantly lower values for stabilizing rotation. Skewness of velocity derivative is also suggestive of nonlinearity associated with three-dimensional turbulence in the cases with moderate anticyclonic rotation. All stratified cases with or without rotation are in a high-stratification regime in the sense of being quasi-two-component, with more than 95% of turbulent kinetic energy being horizontal. Lastly, streamwise spectra show much shallower spectra for the inertially unstable cases, albeit not nearly as shallow as the unstratified cases.

The contents of Chapter 4 are published in the *Journal of Fluid Mechanics*. E. Arobone and S. Sarkar. "Evolution of a stratified rotating shear layer with horizontal shear. Part 2. Nonlinear evolution", J. Fluid Mech., 732, 373-400, 2013. The authors are pleased to acknowledge support by the National Science Foundation CDI program through Grant No. OCE-0835839. The authors also are grateful for computational resources through the Triton Affiliations and Partners Program at San Diego Supercomputing Center and a Startup allocation through the Extreme Science and Engineering Discovery Environment (XSEDE).

Chapter 5

Effects of Three-Dimensionality on Frontal Stability and Turbulence

5.1 Introduction

The symmetric instability (SI) is an instability of baroclinic zonal flows where perturbations contain no longitudinal variation, and are thus two-dimensional. The stability analysis of Stone (1966) explores a balanced zonal flow of the form $u(z)$ which is balanced by a temperature field of the form $\theta(y, z)$. The symmetric instability dominates when the Richardson number ($Ri = N^2/S^2$) between 0.25 and 0.95 for $S = ||\partial \boldsymbol{u}_h/\partial x_3||$, while baroclinic and Kelvin-Helmholtz (K-H) instabilities dominate at higher and lower Ri, respectively. In a more general case, including horizontal shear, instability manifests when potential vorticity ($q = -\rho_0^{-1}(\omega_i + f\delta_{i3})\partial\rho'/\partial x_i$) or PV is of opposite sign of the Coriolis parameter in stably stratified regions of as noted in Hoskins (1974). These more general flows are susceptible to inertial/centrifugal and symmetric instabilities which act on absolute vertical vorticity opposing planetary rotation and vertical shear, respectively. In general, balanced baroclinic zonal flows have PV given by $q = -fS^2 + (\omega_3 + f)N^2$ (Thomas *et al.*, 2013).

An exceptionally sharp (1km) front near the beginning of the Kurushio extension was investigated by D'Asaro *et al.* (2011). Shipboard measurements, a Lagrangian float and a towed profiling vehicle allowed for measurements of turbulence intensity (inferred from vertical motions of the float), temperature, salinity, pressure, and velocity profiles. The front is less than $1km$ wide and about $20m$ deep and contains vertical motion resulting from upper ocean turbulence. Dissipation at the front is estimated to be $10-20$ times stronger than outside the front but surface winds and cooling are too weak to explain the observed turbulence. The potential vorticity was found to take the opposite sign of f for 0.2 days while the vessel passed through the front, strongly suggesting symmetric instability as the relevant mechanism. These results suggest that in some regions of the upper ocean, lateral density gradients and symmetric instability may be more important than atmospheric forcing in setting turbulence intensity.

Evolution of a symmetrically unstable density front is examined using linear stability theory and two-dimensional nonlinear numerical simulations in Taylor & Ferrari (2009). The *a priori* assumption of symmetric (no along-front or x_1 variation in Figure 5.1) allows for the two-dimensional (x_2, x_3) approximation of simulations presented in Taylor & Ferrari (2009). Linear stability analysis demonstrated that for large $|N/f|$ viscous effects on the slope of symmetric currents is negligible and that $Ri < 0.25$ is satisfied locally before the flow is fully nonlinear. Once the instability reaches finite amplitude, a secondary K-H instability forms. Following the secondary instability, small-scale turbulence injects positive PV into the mixed layer from the thermocline and from the upper boundary, resulting in a rapid equilibration of the flow as the PV approaches zero throughout the mixed layer.

The analysis of Stone (1966) is greatly expanded to include the parameter regime where perturbations are not nearly aligned with the spanwise or longitudinal direction in Stone (1970). Growth rates of tilted modes depend only on the amplitude of tilt and not the direction. Additionally, the strongest growth rates never occur in the newly explored regime, instead occurring near the baroclinic (spanwise) or symmetric (longitudinal) axes, depending on Ri.

The three-dimensional counterpart ($k_1 \neq 0$) to symmetric instability is explored in greater detail in Jones & Thorpe (1992) using non-hydrostatic numerical simulation. The basic flow is two-dimensional with velocity given by $u_1(x_3)$ and $\rho(x_2, x_3)$ and $Ri = 0.4$. Linear evolution is explored with respect to three initially-symmetric perturbation types : a streamfunction perturbation isolated in x_2 direction, a density perturbation isolated in the x_2 direction and a density perturbation isolated in the x_2 and x_3 directions (parcel perturbation). Initially, the first and second perturbations types loose symmetry developing a counter-clockwise angle of horizontal tilt relative to the symmetric axis resulting in decreased $\langle u_2' u_3' \rangle$ slowing perturbation growth. Later, both perturbations rotate in a clockwise manner reducing tilt and increasing growth. The parcel perturbation leads to tilting only in the clockwise direction. Analysis showed that off-symmetric modes grow fastest for large perturbation length scales, while symmetric modes grow fastest for small-scale disturbances.

Instabilities in a baroclinic zonal flow were explored in Molemaker *et al.* (2010) using quasigeostrophic and Boussinesq nonlinear simulations. This study explores the emergence of a forward energy cascade in a flow with $Ro = |S/f| < 1$ but not $Ro \ll 1$ and $Ri = N^2/S^2 > 1$. Turbulence in the Boussinesq case emerged via the generation of sharp fronts (locally $Ri < 1$ and $Ro > 1$) and subsequent frontal instabilities. Unbalanced motions represent only a small portion of the total kinetic energy of the flow, yet they are essential in driving energy to dissipative scales. Results suggest that total energy lost during spin-down of the flow approaches a constant value for the Boussinesq cases while approaching zero for quasigeostrophic cases as $Re \to \infty$. The inference is that frontal instabilities could play an important role in the extraction of energy from largely balanced flows, even far away from ocean boundaries.

For homogeneous baroclinic flows, it is shown that even though symmetric modes dominate as $t \to \infty$, there exists the possibility for non-symmetric modes to be favored over intermediate times when $Ri \leq 1$ and $Ro = |S/f| \geq 1$ (Mamatsashvili *et al.*, 2010). Optimal growth was determined for $Ri = 0.3$, 0.6 and 0.9 and $Ro = 1$, 3 and 10 at over the characteristic time period associated with symmetric

instability ($T = \sigma^{-1} \sim \mathcal{O}(f^{-1})$). In the three $Ro = 10$ cases, the energy gained by the optimal non-symmetric mode was over ten times greater than the growth in the symmetric mode. In all simulated cases, the optimal growth occurred when modes were significantly off-symmetric with $-1.84k_2 < k_1 < -0.48k_2$.

Direct numerical simulations of a zonal baroclinic flow were explored in Pieri *et al.* (2013). Here, Ri and M^2/N^2 were varied extensively and their effects on homogeneous turbulence identified. Turbulence grew in the symmetrically unstable range only when $M^2/N^2 > 0.2$. For $Ri \sim 0.1$, potential vorticity PDFs are rather symmetric but asymmetry increases with increasing Ri with asymmetry in favor of negative potential vorticity. Results were from simulations at a fairly low Reynolds number with $Re_{\lambda,0} = 33$ and simulations were only performed over short time intervals ($0 < St < 20$) such that development of SI was limited.

This study seeks to explore the manifestation of frontal instabilities and expected secondary instabilities in a fully three-dimensional symmetrically-unstable vertically-sheared flow. First the dependence on domain size is explored, then non-modal linear stability analysis is used to explain flow behavior before secondary shear instabilities. The effect of off-symmetry is explored using simulations of horizontally-tilted structures in both two- and three-dimensional flow. Lastly, a scaled down version of the front is used to explore the progression from off-symmetric currents to secondary shear instabilities to turbulence and its energetics.

5.2 Formulation

The dimensional equations for conservation of mass, momentum, and density for a Boussinesq fluid in a frame of reference rotating about the vertical axis are given below with dimensional variables denoted by * (centrifugal acceleration is neglected) :

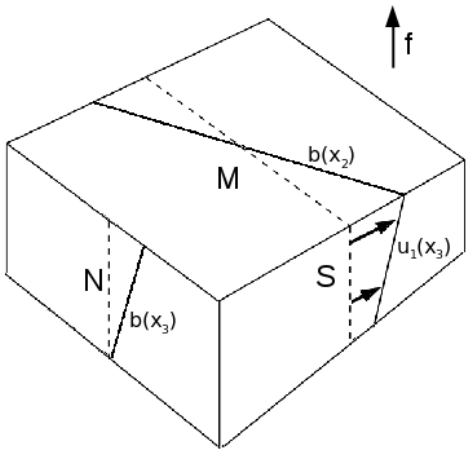

Figure 5.1: Schematic showing a stratified vertically-sheared flow in thermal wind balance. Spatial gradients in velocity and buoyancy are shown along with their respective time scales.

$$\frac{\partial u_i^*}{\partial x_i^*} = 0$$
$$\frac{\partial u_i^*}{\partial t^*} + \frac{\partial \left(u_i^* u_j^*\right)}{\partial x_j^*} + \epsilon_{i3k} f^* u_k^* = -\frac{1}{\rho_0^*}\frac{\partial p^*}{\partial x_i^*} + \nu^* \frac{\partial^2 u_i^*}{\partial x_j^* \partial x_j^*} - \frac{\rho'^* g^*}{\rho_0^*}\delta_{i3}$$
$$\frac{\partial \rho^*}{\partial t^*} + \frac{\partial \left(\rho^* u_j^*\right)}{\partial x_j^*} = \kappa^* \frac{\partial^2 \rho^*}{\partial x_j^* \partial x_j^*}$$

The density and pressure fields are decomposed in the following manner for uniform stratification,

$$\rho^*\left(x_i^*, t^*\right) = \rho_0^* + \frac{\partial \overline{\rho}^*}{\partial x_2^*} x_2^* + \frac{\partial \overline{\rho}^*}{\partial x_3^*} x_3^* + \rho'^*\left(x_i^*, t^*\right),$$
$$p^*\left(x_i^*, t^*\right) = \overline{p}^*\left(x_2^*, x_3^*\right) + p'^*\left(x_i^*, t^*\right),$$

where $\overline{\rho}^*$ represents the background stratification and $\overline{p}^*$ is in hydrostatic and geostrophic balance with the initial density profile $(\rho_0^* + \overline{\rho}^*)$ and initial mean velocity profile. The initial mean velocity corresponds to uniform vertical shear of the form

$$f^* \frac{\partial \bar{u}_1^*}{\partial x_3^*} = \frac{g^*}{\rho_0^*} \frac{\partial \bar{\rho}^*}{\partial x_2^*}.$$

The mean vertical shear is allowed to evolve with time as dictated by the conservation equations. Additionally we introduce variables $M^{*2} = -g^*/\rho_0^* \times \partial\bar{\rho}^*/\partial x_2^*$ and $N^{*2} = -g^*/\rho_0^* \times \partial\bar{\rho}^*/\partial x_3^*$. This implies that $\partial\bar{u}_1^*/\partial x_3^* = -M^{*2}/f^*$. Note that $M^{*2} < 0$ in the present problem. The physical problem of interest is illustrated in Figure 5.1. The non dimensional variables for this problem are given as

$$t = |M^*|\, t^*, \quad x_i = \frac{{x_i}^*}{L_3^*}, \quad u_i = \frac{{u_i}^*}{|M^*|\, L_3^*}, \quad \rho' = \frac{-{\rho'}^*}{L_3^* \left(\partial\overline{\rho}^*/\partial x_2^*\right)}, \quad p' = \frac{{p'}^*}{\rho_0^* \left|M^{*2}\right| L_3^{*2}}.$$

The following non-dimensional equations for mass conservation, momentum conservation and density perturbation evolution are obtained along with relevant non-dimensional parameters

$$\begin{aligned}
&\frac{\partial u_i}{\partial x_i} = 0, \\
&\frac{\partial u_i}{\partial t} + \frac{\partial \left(u_i u_j\right)}{\partial x_j} + \epsilon_{i3k} f u_k = -\frac{\partial p'}{\partial x_i} + Ekf \frac{\partial^2 u_i}{\partial x_j \partial x_j} - \rho' \delta_{i3}, \\
&\frac{\partial \rho'}{\partial t} + \frac{\partial \left(\rho' u_j\right)}{\partial x_j} + u_2 - \beta u_3 = \frac{Ekf}{Pr} \frac{\partial^2 \rho'}{\partial x_j \partial x_j}, \\
Ek = \frac{\nu^*}{f^* L_3^{*2}}, \quad &f = \frac{f^*}{|M^*|}, \quad \beta = \frac{N^{*2}}{|M^{*2}|}, \quad Pr = \frac{\nu^*}{\kappa^*}.
\end{aligned}$$

Based on these non-dimensional parameters the Richardson number for the base flow is given by $Ri = f^2\beta$. Homogeneous Neumann boundary conditions are used for u_1, u_2, and ρ' implying free-slip and no mass flux conditions at vertical boundaries. Homogeneous Dirichlet boundary conditions are used for u_3 at vertical boundaries implying no through-flow. Periodicity is enforced in the horizontal directions for all variables.

Table 5.1: Simulation parameters and case names. L_i and N_i represent the length of domain and number of computational points, respectively, in each direction. Multiple grids are used in simulating the bottom four cases. In all cases $L_3 = 1$.

case	Ek	θ	f	β	L_1	L_2	N_1	N_2	N_3
L1_4	10^{-4}	$0°$	0.152	21.4	4	8	64	256	128
L1_8	10^{-4}	$0°$	0.152	21.4	8	8	128	256	128
L1_16	10^{-4}	$0°$	0.152	21.4	16	8	256	256	128
L1_32	10^{-4}	$0°$	0.152	21.4	32	8	512	256	128
L1_64	10^{-4}	$0°$	0.152	21.4	64	8	1024	256	128
2D0	10^{-4}	$0°$	0.152	21.4	∞	8	1	1024	128
2D-5	10^{-4}	$-5°$	0.152	21.4	∞	8	1	1024	128
2D-10	10^{-4}	$-10°$	0.152	21.4	∞	8	1	1024	128
3D0	2×10^{-4}	$0°$	0.152	21.4	8	8	256-1024	256-1024	128
3D-5	2×10^{-4}	$-5°$	0.152	21.4	8	8	256-1024	256-1024	128
3D-10	2×10^{-4}	$-10°$	0.152	21.4	8	8	256-1024	256-1024	128
Turb-10	2×10^{-4}	$-10°$	0.25	8	4	4	256-1024	256-1024	256

5.3 Effect of Domain Size

This study begins by performing three-dimensional simulations in the parameter regime of the two-dimensional simulations of Taylor & Ferrari (2009). Initial conditions contain three-dimensional fluctuations in addition to the uniform shear and buoyancy gradient. The numerical algorithm uses either second-order central differencing or sixth-order compact differencing on a grid that is staggered in the x_2 and x_3 directions. A fourth-order (second-order for Turb-10) parallelized multigrid Poisson solver is used to solve for non-hydrostatic pressure every Runge-Kutta substep. The Navier-Stokes and density equations evolve using a third-order Runge-Kutta time-marching scheme. Parallelization is accomplished using MPI. Case specific computational details are shown in Table 5.1. Two dimensional simulations use a kinetic energy spectrum of $E \propto k^8 \exp(-4k^2/k_0^2)$, while the three-dimensional cases include only those modes where $10k_h^2 \leq k_3^2$ using a spectrum of the form $E \propto k^4 \exp(-2k^2/k_0^2)$. The restriction is introduced to prevent energy from going into large k_1 modes which are quickly dissipated in the three-dimensional cases.

Due to the fact that dependence on along-front domain length (L_1) is not known a priori, a range of horizontal aspect rations ($0.5 \leq L_1/L_2 \leq 8$) were used. In all simulations varying L_1, vertical vorticity quickly organized into structures primarily aligned along the horizontal axis tilted 45° *off-symmetric* in the clockwise direction. As time progressed, vertical vorticity gradually reduced its degree of off-symmetry and increased in horizontal scale as seen in Figure 5.2. In all L1_ cases but L1_64 the flow rapidly two-dimensionalized *before* the development of strong nonlinearity. The time of two-dimensionalization increases with increasing L_1, until case L1_64 which develops strong nonlinearities before the flow can reach a symmetric state.

The misalignment of ω_1 structures (off-symmetric instability currents) with respect to isopycnals throughout the simulation is seen in Figure 5.3. The misalignment becomes less dramatic at later time as the flow becomes more nonlinear and the vortical structure aligns more with the symmetric axis. The reason large L_1 is needed to capture near-symmetry is due to the periodic boundary conditions in the x_1 direction and the large horizontal scale (k_h) of the instability modes. For structures with a lateral width of δ, periodicity implies that the smallest off-symmetric angle possible is $\theta \sim \tan^{-1}(\delta/L_1)$ implying that nearly symmetric modes require $L_1 \gg \delta$. When L_1 is not sufficiently large, then energy rapidly transfers from the $\theta \sim \tan^{-1}(\delta/L_1)$ currents to symmetric ($\theta = 0$) currents rather than θ continuing to decrease gradually. The rest of this study seeks to further explain the emergence of nearly-symmetric flow and explore its subsequent evolution. In the 3D-5 and 3D-10 cases, the domain is rotated about the vertical axis to reduce the L_1 required to capture currents with a small degree of off-symmetry.

5.4 Non-Modal Linear Stability Analysis

Linear stability analysis of the baroclinic flow may lead to insights regarding the behavior of the coherent structures, specifically the decrease in off-symmetry with time and lack of emergence of symmetric modes. Mamatsashvili *et al.* (2010) explored the early transients ($t \sim f^{-1}$), but we are more interested in longer

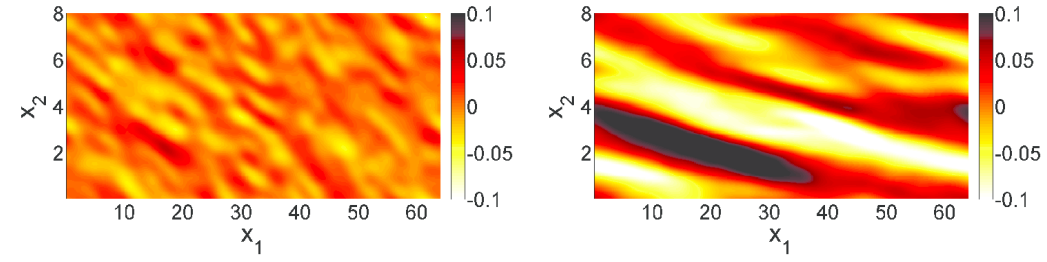

Figure 5.2: Contours of vertical vorticity (ω_3) from case L1_64 when (a) $t = 2.17f^{-1}$ and (b) $t = 7.09f^{-}1$. The cases with smaller L_1 two-dimensionalize (i.e. energy contained primarily in $k_1 = 0$ modes) well before $t \sim 7f^{-}1$.

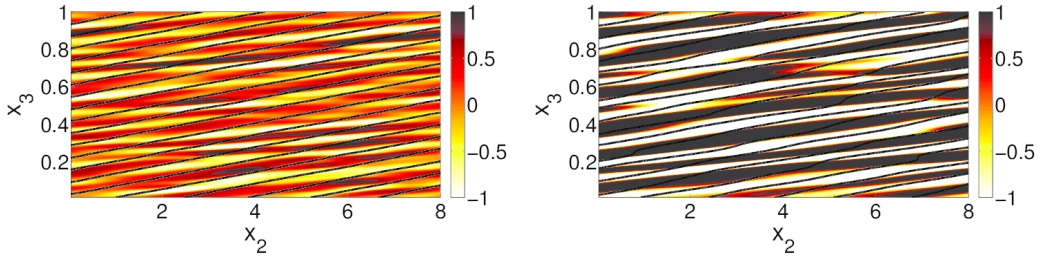

Figure 5.3: Contours of along-front vorticity (ω_1) and isopycnals from case L1_64 when (a) $t = 2.17f^{-1}$ and (b) $t = 7.09f^{-}1$. The cases with L_1 smaller than 64 display far better alignment between ω_1 and isopycnals when $t \sim 7f^{-}1$.

evolution times since secondary instability occurs when $t \gg f^{-1}$ in this flow. The base state corresponding to a balanced uniform front is given by

$$\langle u_1 \rangle = S x_3 = -\frac{M^2}{f} x_3 \qquad \langle \rho \rangle = \rho_0 + \nabla_2(\langle \rho \rangle) x_2 + \nabla_3(\langle \rho \rangle) x_3$$

Assuming modes of the form $\phi(t)\exp(ik_j x_j)$, one finds that $dk_3/dt = M^2 k_1/f$ as a direct consequence of flow homogeneity. Rotating the domain about the vertical axis such that $\tan\theta = -k_1/k_2$ allows for new coordinates such that $\tilde{k}_1 = 0$ and $\tilde{k}_2 = k_h$. Under this transformation the symmetric instability corresponds to $\theta = 0$, allowing exploration of the effect of off-symmetry by varying θ. The following linear inviscid governing equations describe motion in the rotated coordinate system.

$$\begin{aligned}
\frac{du_1'}{dt} &= f u_2' + \cos\theta \frac{M^2}{f} u_3' & \frac{du_2'}{dt} &= -f u_1' - \sin\theta \frac{M^2}{f} u_3' - i k_h p'/\rho_0 \\
\frac{du_3'}{dt} &= -i k_3 p'/\rho_0 - g\rho'/\rho_0 & \frac{d\rho'}{dt} &= -\sin\theta \frac{\partial \langle \rho \rangle}{\partial x_2} u_1' - \cos\theta \frac{\partial \langle \rho \rangle}{\partial x_2} u_2' - \frac{\partial \langle \rho \rangle}{\partial x_3} u_3' \\
0 &= i k_h u_2' + i k_3 u_3'
\end{aligned}$$

From continuity, the pressure and vertical velocity variables can be expressed as functions of the other variables. Normalizing all wavenumber components by dividing by k and letting $b' = -g\rho'/\rho_0$ gives the following evolution equation of the form $d\phi_i'/dt = A_{ij}\phi_j'$ for perturbations

$$\frac{d}{dt}\begin{bmatrix} u_1' \\ u_2' \\ b' \end{bmatrix} = \begin{bmatrix} 0 & (f - \cos\theta M^2 k_h/(f k_3)) & 0 \\ -f k_3^2 & \sin\theta k_h k_3 M^2/f & -k_h k_3 \\ -\sin\theta M^2 & N^2 k_h/k_3 - \cos\theta M^2 & 0 \end{bmatrix} \begin{bmatrix} u_1' \\ u_2' \\ b' \end{bmatrix}$$

The sin terms above grow in influence as the modes become more off-symmetric. Taking $\theta = 0$, or for *purely symmetric instability* we obtain a characteristic equation of the form

$$\sigma^2/k_3^2 = M^4/N^2 - f^2 - N^2\left(k_2/k_3 - M^2/N^2\right),$$

agreeing with the relation given in Taylor & Ferrari (2009) for geophysical modes ($k_3 \approx 1$). The time evolution of the normalized wavenumber components and are given by

$$dk_3^2/dt = -dk_h^2/dt = 2M^2 \sin\theta k_h^3 k_3/f. \tag{5.1}$$

This implies that frontal strength, degree of off-symmetry, and initial alignment of the wavenumber vector affect how rapidly shear modifies k_3. The non-modal stability problem is solved through introduction of

$$\boldsymbol{E}_{ij}(t) = \sqrt{\delta_{ij} + \delta_{i2}\delta_{2j}k_h^2 k_3^{-2}(t)}, \qquad \boldsymbol{D}(t) = \left(\frac{d\boldsymbol{E}(t)}{dt} + \boldsymbol{E}(t)\boldsymbol{A}(t)\right)\boldsymbol{E}^{-1}(t)$$
$$\text{and } \boldsymbol{\Phi}(T) = \exp\left(\int_0^T \boldsymbol{D}(t)dt\right).$$

Perturbation energy is given by $\|\boldsymbol{D}(t)\boldsymbol{\phi}(t)\|^2$ and perturbation energy growth over period T is given by the square of the maximum real eigenvalue of $\boldsymbol{\Phi}(T)$. Figure 5.4 shows the eigenvalues of $\boldsymbol{\Phi}(T)$ normalized by f (for SI at $Ri = 0.5$ one finds $\sigma = f$). As time increases, a trend of gradually decreasing off-symmetry is observed, agreeing with the results of section 5.3. There are several important subtleties which affect flow evolution. Even for small positive θ (the right half of the circles not shown in 5.4) the stabilization of near-symmetric modes is dramatic, with $dk_3/dt \propto \sin\theta$ implying a change of sign at the symmetric axis. The modes, initially with $k_3 < 0$, become more vertical as time increases when $\theta > 0$ and $dk_3/dt > 0$, implying stabilization of the currents by background stratification. It is not surprising that it is difficult to generate purely symmetric modes in the limit of $L_1/L_2 \gg 1$ (e.g. the L1_64 simulation) given that the symmetric axis is very nearly the stability boundary for $t \sim f^{-1}$.

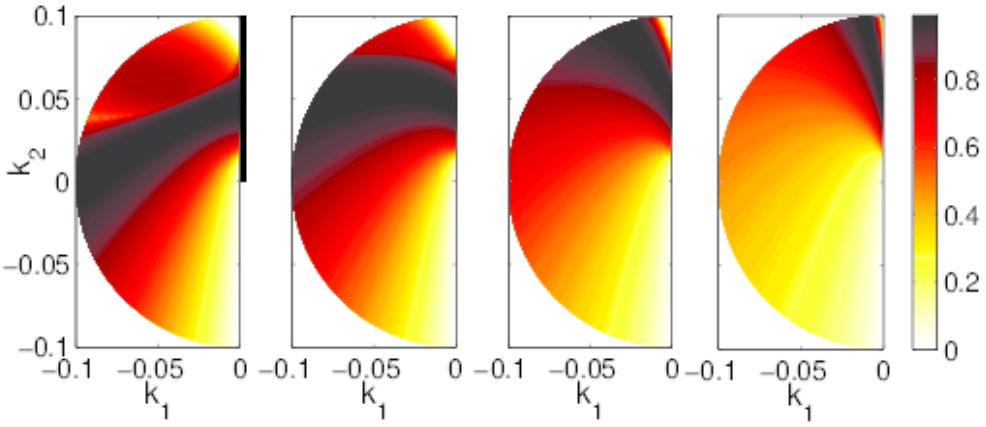

Figure 5.4: Plots showing the maximum real eigenvalues (normalized by f). Growth rates are shown over various periods given by $T = f^{-1}$, $2f^{-1}$, $4f^{-1}$ and $8f^{-1}$ from left to right, respectively.

As f is decreased while preserving Ri the stability diagrams do not change appreciably other than an increase in horizontal thickness due to change in β. Reducing Ri to 0.3 results in modes which are less off-symmetric, but the general trend in Figure 5.4 is still found. Three-dimensional fluctuations grow at near or greater than the symmetric growth rate throughout the range of time scales associated with development of SI without the strict requirement of $k_1 = 0$. It is because of the tendency for currents to become more aligned with the symmetric axis as time increases that we shift our attention to understanding the development of secondary shear instabilities in symmetric and nearly-symmetric flows.

5.5 Effect of Off-Symmetry

5.5.1 Two-Dimensional Simulations

To explore the more basic effects of off-symmetry, several two-dimensional simulations were performed. The first simulation mimicked that of Taylor & Ferrari (2009) with identical f, β and Ek. The other two simulations are identical except that the computational domain is rotated clockwise about the vertical axis by 5° in case 2D-5 and 10° in case 2D-10 (i.e. $\theta = -5°$ and $\theta = -10°$). This is similar to the rotation of the linear modes in the previous section. In the linear

stability analysis, solutions were constant along planes of the form $k_i x_i = C$ and therefore one-dimensional varying only in the direction of $\boldsymbol{k}$. These nonlinear two-dimensional simulations allow for fluctuations that are constant along horizontal lines of the form $k_1 x_1 + k_2 x_2 = C$ where $\tan\theta = k_1/k_2$.

The non-modal stability analysis of section 5.4 and simulation L1_64 illustrate the tendency for large-scale currents to nearly align with the symmetric axis when $t \gg f^{-1}$. Based on the observation that case L1_64 goes strongly nonlinear when $\theta \sim -5°$, one can compare the two-dimensional symmetric instability growth of perturbations to that of the off-symmetric growth observed in L1_64 and the tilted two dimensional simulation with $\theta \sim -5°$. Figure 5.5 shows growth of fluctuations in case L1_64 agreeing better with the off-symmetric two-dimensional simulation than the symmetric simulations after the initial flow adjustment. The reduction in growth is primarily due to vertical shearing of the off-symmetric instability because the growth rate associated with infinitesimal time (maximal real eigenvalue of $\boldsymbol{A}$ from section 5.4) only reduces to 99.3% of the symmetric value. The initial decay of fluctuations in the two dimensional simulations is not observed in three-dimensional cases owing to the fact that the three-dimensional instabilities of Mamatsashvili *et al.* (2010) associated with growth over $T \sim f^{-1}$ (similarly demonstrated in Figure 5.4) cannot manifest in the two dimensional nearly symmetric cases.

Snapshots of isopyncals and plane-normal vorticity are displayed from the symmetric and $\theta = -10°$ cases in Figure 5.6 as the flow becomes nonlinear. The primary distinctions between $\theta = 0$ and $\theta = -10°$ are due to the linear prediction of equation 5.1. Vertical shearing in the off-symmetric case ($\langle\omega_n\rangle = \sin\theta/f = -1.14$) continually reduces the vertical inclination of currents resulting in currents which are shallower than isopycnals. The increase of $|k_3|$ by vertical shearing suggests the vertical scale in the off-symmetric cases should be lower than the symmetric case, but this is not observed because of viscous effects. The viscous growth rate for SI is given by

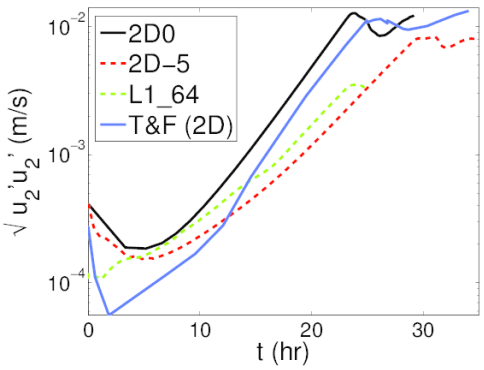

Figure 5.5: Evolution of across-front fluctuations in two-dimensional simulations with varying tilt and a three dimensional simulation (L1_64) with no tilt and a large along-front domain length.

$$\sigma/f \sim \sqrt{Ri^{-1}-1} - \nu k_3^2/f = \sqrt{Ri^{-1}-1} - 4\pi^2 Ek\,\delta^2$$

This implies that growth rates should rapidly drop off (for instance, decrease by more than 25%) when the vertical scale is $\delta \lesssim 1/8$ for $Ri = 0.5$ and $Ek = 10^{-4}$. The continual shearing due to non-zero $\langle \omega_n \rangle$ leads to merging of currents and misalignment with respect to isopyncals, but shearing does not reduce the vertical scale of currents due to currents forming at a scale already marginally influenced by viscosity.

The turbulent kinetic energy (TKE) budgets are shown for cases 2D0 and 2D-10 in Figure 5.7 (a) and (b), respectively. The terms contain in the budgets are shear production $P = -\left\langle u_i' u_j' \right\rangle \partial \left\langle u_i \right\rangle / \partial x_j$, buoyancy flux $B = -\left\langle u_3' \rho' \right\rangle$ and viscous dissipation $\epsilon = 2Ek \left\langle s_{ij}' s_{ij}' \right\rangle$. It takes considerably longer to develop off-symmetric currents, as anticipated from the linear stability analysis for $t \to \infty$. Buoyancy flux plays a dramatically different role in the two cases, only contributing as a sink after the symmetric case breaks down and being a significant energy source for the off-symmetric case.

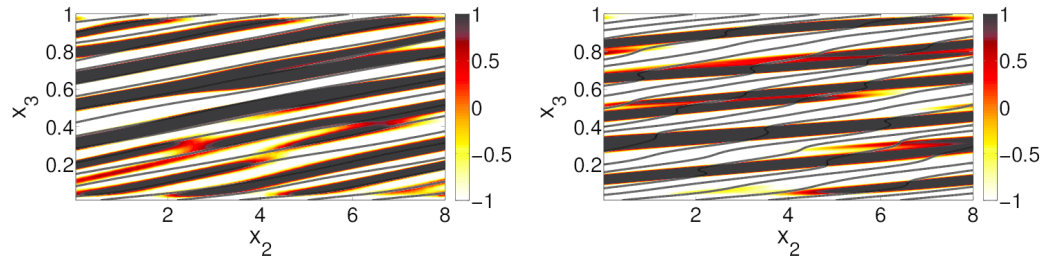

(a) (b)

Figure 5.6: Contours of plane-normal vorticity from two dimensional simulations. (a) $\theta = 0°$ and $t = 6.84f^{-1}$ and (b) $\theta = -10°$ and $t = 13.4f^{-1}$. Isopycnals are also shown by thin solid curves.

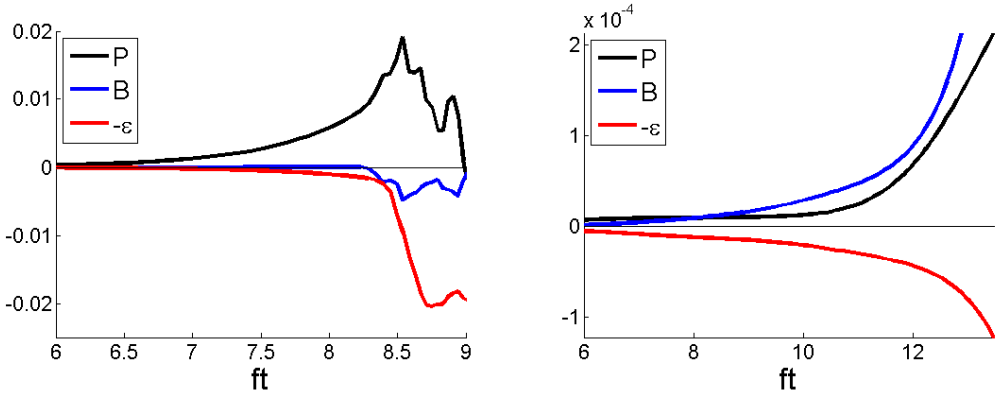

(a) (b)

Figure 5.7: Volume integrated turbulent kinetic energy budgets from two-dimensional simulations with (a) $\theta = 0°$ and (b) $\theta = -10°$.

5.5.2 Three-Dimensional Simulations

In cases 3D0, 3D-5 and 3D-10 the spatial extent in the x_1 direction is set to 8 allowing for increased spatial resolution relative to the $L1\_64$ case at comparable computational cost. This reduced domain size allows for increased resolution of the secondary K-H instability as first explored in two-dimensional simulations of Taylor & Ferrari (2009). In two-dimensional frontal simulations K-H rollers are forced to align with the x_1' direction unlike our three-dimensional simulations. Figure 5.8 shows λ_2 isocontours (Jeong & Hussain, 1995) capturing coherent vortical structures emerging as a result of secondary K-H instability with orientation substantially tilted with respect to the x_1' axis. The emergence of the K-H rollers is most rapid in the symmetric cases while the wavelength associated with instability decreases as off-symmetry increases. The faster growth rates associated with SI are responsible for the more rapid attainment of $Ri < 0.25$ in localized regions of the flow.

It appears counter-intuitive that positive ω_n vortex sheets would roll up before the stronger negative ones since K-H growth rates for mixing layers are proportional to shear strength. It will be shown in the section 5.6.2 that this preference is due to the these regions being unstable to gravitational instability.

The alignment of coherent secondary K-H rollers is explained by the following analysis. For symmetric instability ($k_h/k_3 = \beta^{-1}$ and $\theta = 0$) the modal stability problem simplifies to an eigenvalue problem of the form $\lambda_{\max}\boldsymbol{\phi} = \boldsymbol{A}\boldsymbol{\phi}$ with $b' = 0$. Solving for the corresponding eigenvector gives

$$\begin{bmatrix} u_1' \\ u_2' \\ u_3' \end{bmatrix} = \begin{bmatrix} \sqrt{(Ri^{-1}-1)(1+\beta^{-2})} \\ -1 \\ \beta^{-1} \end{bmatrix} \exp\left(i\beta^{-1}k_3x_2 + ik_3x_3 + k_3\sqrt{Ri^{-1}-1}ft\right),$$

which predicts that SI currents will flow at a horizontal angle significantly tilted with respect to the across-front direction. In the case of $Ri = 0.5$ and $\beta^{-2} \ll 1$ an angle of 45° is predicted. Cases 3D0, 3D-5 and 3D-10 were not able to resolve the intense non-linearity observed after breakdown of the secondary

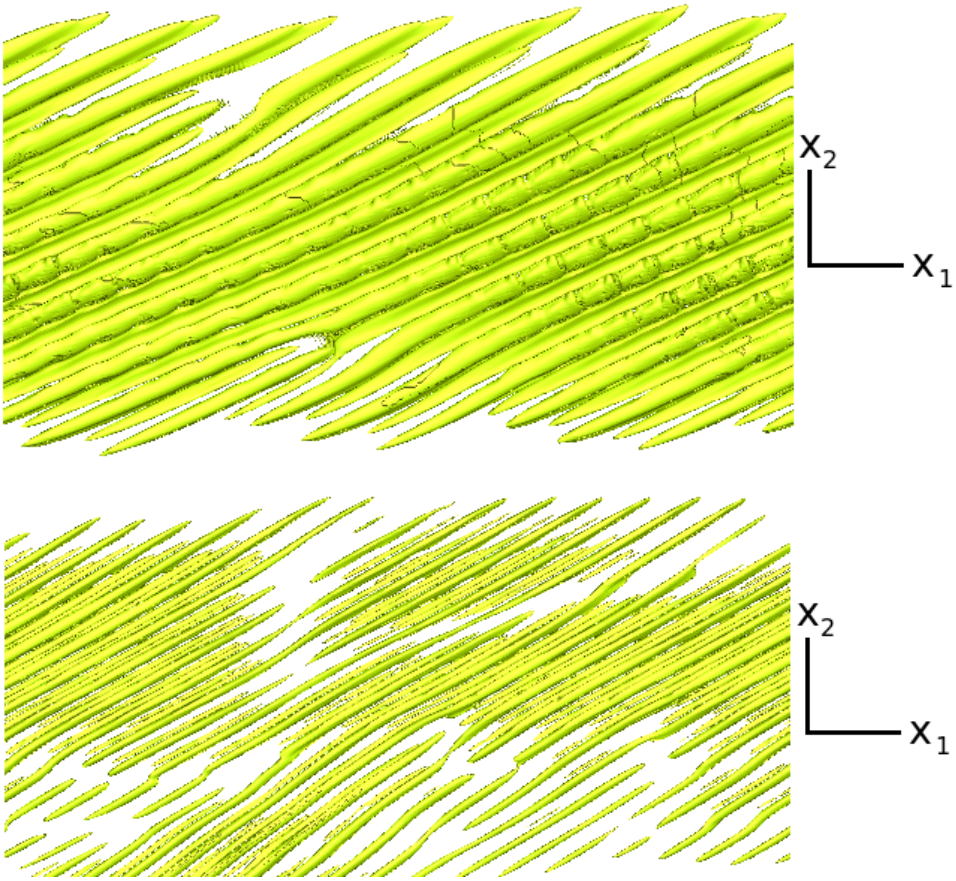

(a)

Figure 5.8: Isosurface of λ_2 during development of secondary instability for (a) case 3D0 when $t = 9.08f^{-1}$ and (b) case 3D-10 when $t = 7.93f^{-1}$.

instability. Section 5.6.2 will explore the transition to turbulence of a similar ($Ri = 0.5$) front on case Turb-10.

5.6 Frontal Turbulence

Computational exploration of turbulence in a strong submesoscale front using direct numerical simulation is challenging owing largely to the wide range of time scales ($S^* \sim N^* \gg M^* \gg f^*$) influencing flow evolution. By increasing $f^*/|M^*|$ from 0.152 to 0.25 and decreasing $\beta = N^{*2}/|M^{*2}|$ from 21.4 to 8 in case Turb-10 we are able to reduce S/f by a factor of almost three without significantly violating the separation of time scales assumption. Increasing grid resolution by

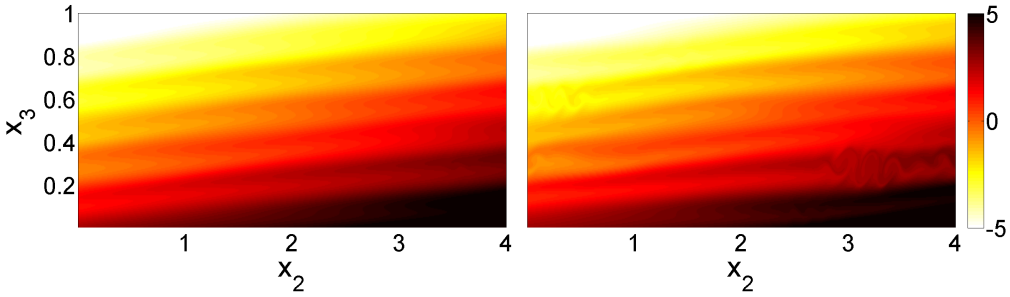

Figure 5.9: Vertical snapshots of density variation $\rho - \rho_0 = \rho' + x_2 - \beta x_3$ when $t = 9f^{-1}$ (left) and $t = 9.23f^{-1}$ (right). Showing density fluctuations immediately preceding and during secondary instability.

a factor of two helps fully resolve the shear-convective instabilities which will be discussed in this section. In order to reduce computational complexity the size of the domain in each of the horizontal directions is reduced by a factor of two to focus on turbulence rather than the evolution of the currents.

5.6.1 Qualitative Features

The two major features of off-SI not observed in SI are the misalignment of currents and isopycnals and the fact that buoyancy flux is a significant source of fluctuating kinetic energy. These two features are related in the sense that vertical shear drives misalignment which then drives motion across isopycnals leading to a density variation very similar to that seen in the Turb-10 case in Figure 5.9. Unstably stratified regions appear throughout the domain as a result of these slantwise currents. Eventually the shear and density anomaly grow strong enough to lead to secondary instability. The vorticity signature associated with the development of secondary instability is shown in Figure 5.10. At this time the two-dimensional assumption appears very reasonable with ω_n in the $x_1 - x_3$ plane showing next to no dependence on x_1. The regions of the density field being strongly stirred in Figure 5.9 coincide with vortex sheets with positive vorticity in Figure 5.10. After this point (i.e. $ft > 9$), the flow in the $x_1 - x_3$ plane develops weak variability in the x_1 direction as normal vorticity fluctuations grow due to secondary shear-convective instability.

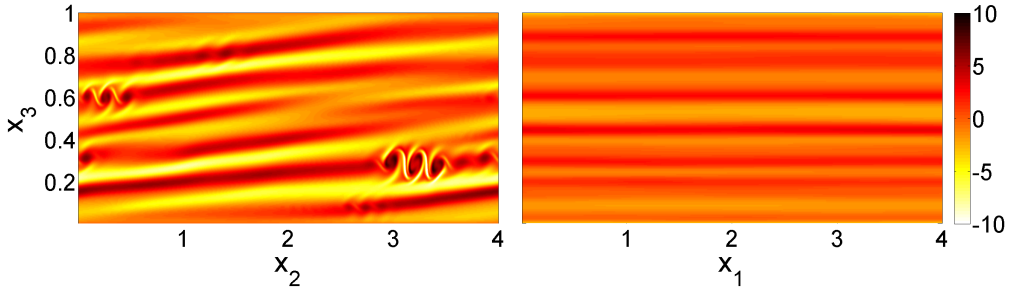

Figure 5.10: A vertical plane of ω_1 at $x_1 = 2$ (left) and a vertical plane of ω_2 at $x_2 = 2$ (right) showing horizontal vorticity during secondary instability at $t = 9.15f^{-1}$.

Eventually, the normal vorticity in the $x_1 - x_3$ plane grows strong enough to itself breakdown, quickly destabilizing the vertical vorticity field. Figure 5.11 shows the development of tertiary shear instability once normal vorticity fluctuations in the $x_1 - x_3$ plane are strong enough to meander and extract energy from the vertical shear. Prior to this point ($ft = 10.7$) mean vorticity was strong relative to vorticity fluctuations such that the effect of shear was primarily the stabilization of vorticity fluctuations in the $x_1 - x_3$ plane. The secondary shear-convective instability is required to rapidly increase vorticity fluctuations in the $x_1 - x_3$ plane because near-SI currents do not effectively augment ω_2 fluctuations. The flow rapidly three-dimensionalizes once the shearing plane destabilizes after the manifestation of the tertiary instability. Figure 5.12 shows ω_1 and ω_2 vorticity fluctuations as the domain rapidly fills with turbulence. By the end of the simulation, nearly the whole computational domain appears turbulent.

5.6.2 Quantitative Analysis

The vorticity dynamics suggest a three-step process drives the transition from linear perturbations to turbulence. First, the off-SI currents grow in a manner consistent with the linear stability analysis. These modes correspond to vortex sheets which are not aligned with isopycnals and contain primarily ω_1 and to a lesser extent ω_2 with no x_1 dependence. Next, these vortex sheets roll up rapidly in the $x_2 - x_3$ plane, increasing ω_2^2 until it is comparable to ω_1^2. This is due to the

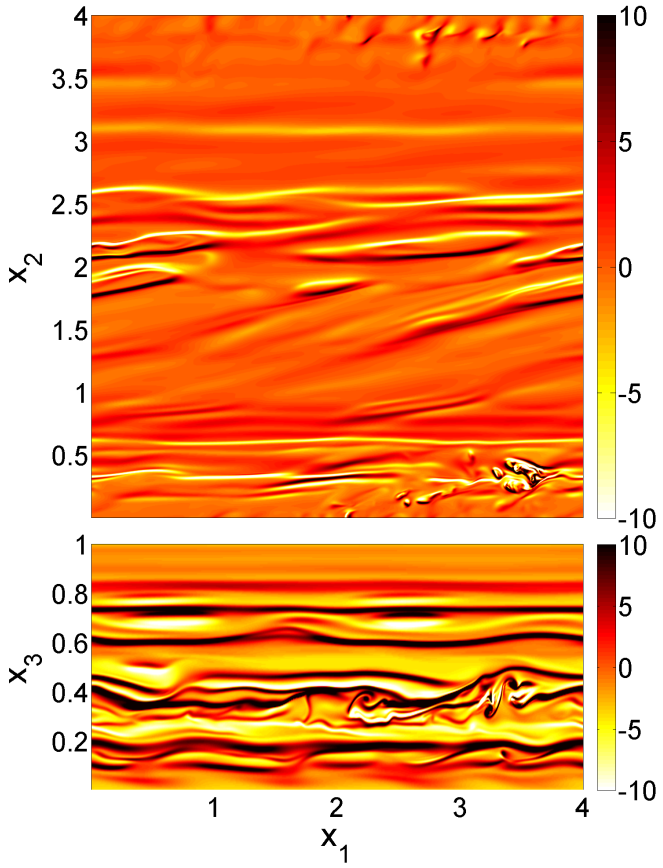

Figure 5.11: A vertical plane of ω_2 at $x_2 = 2$ (bottom) and a horizontal plane of ω_3 at $x_3 = 0.5$ (top) when $t = 10.7f^{-1}$. Snapshots of horizontal and vertical vorticity are shown when flow begins to three-dimensionalize.

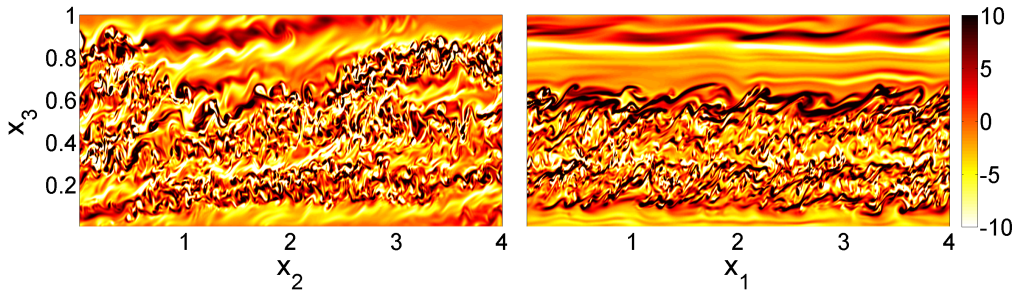

Figure 5.12: A vertical plane of ω_1 at $x_1 = 2$ (left) and a vertical plane of ω_2 with $x_2 = 2$ (right) at $t = 11.6f^{-1}$. Snapshots of horizontal vorticity are taken when strong turbulence fills most of the domain.

orientation of coherent vortices during secondary instability as shown in Figure 5.8. The secondary instability results in the generation of some vertical vorticity fluctuations, but not until the destabilization of the strongly sheared plane can the flow be called fully three-dimensional. This picture is reinforced quantitatively by Figure 5.13 which shows the evolution of volume-averaged vorticity fluctuations broken down by component. From this plot several regions of fundamental change exist. When $ft \sim 9$, the rate of change of ω_2^2 and ω_3^2 rapidly increases. Next, when $ft \sim 11$ the rate of change of ω_1^2 and ω_3^2 rapidly increases. Lastly, when $ft \sim 11.2$ enstrophy shows a sudden decrease followed by a time of linear enstrophy growth as the domain fills with turbulence. This reinforces the notion of three discrete transitional events in the flow.

The bulk energetics of the flow are given via turbulent kinetic and potential energy budgets in Figure 5.14. The turbulent kinetic energy budget shows discrete events at $tf \sim 9$ when shear production (P) switches on as a source, $tf \sim 11$ when buoyancy flux (B) switches becomes a sink, and $tf = 11.2$ when dissipation suddenly jumps. All three are consistent with the observed vorticity dynamics with P switching on due to secondary K-H instability, B switching off due to the development of three-dimensionality and dissipation peaking when the three-dimensional flow breaks down into turbulence. The turbulent potential energy budget shows the rate of extraction of energy from potential energy in the front ($\langle \rho' u_2' \rangle$), the negative buoyancy flux ($-\beta \langle \rho' u_3' \rangle$) and potential energy dissipation (ϵ_ρ). Here $\langle \rho' u_2' \rangle$ shows a drop following secondary instability and dissipation shows a dramatic ramp-up after the tertiary instability and increases further once the flow is turbulent. Mixing efficiency can be approximated by the ratio of time-integrated ϵ_ρ to time-integrated $\langle \rho' u_2' \rangle$. The turbulent potential energy budget suggests very high mixing efficiency under this definition and it appears that very efficient mixing would continue in the turbulent regime. Comparing the magnitudes of ϵ_ρ and $\epsilon + \epsilon_\rho$ also suggests a high mixing efficiency, taking values of roughly 75% in the turbulent regime.

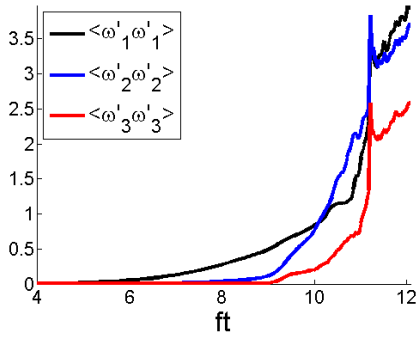

Figure 5.13: Evolution of volume averaged fluctuating enstrophy components showing the development of near-SI followed by secondary instabilities and finally three-dimensional turbulence.

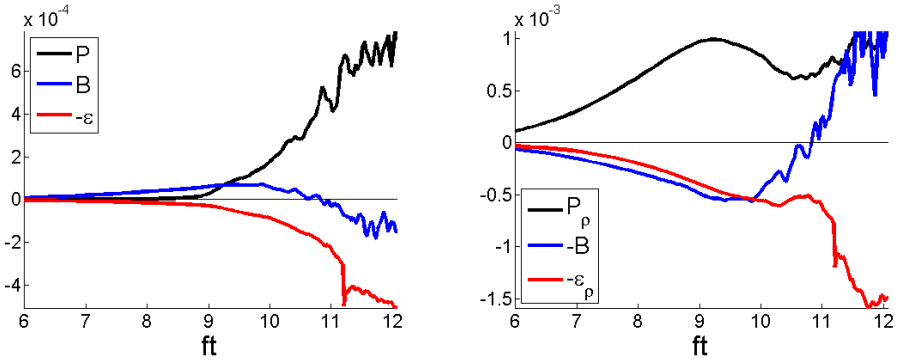

Figure 5.14: Terms from the volume integrated turbulent kinetic energy (left) and turbulent potential energy (right) budgets throughout the duration of case Turb-10.

5.7 Conclusion

This study explores the development of instability and turbulence in a symmetrically unstable variant of Eady's model with $Ri = 0.5$. The novelty of the approach is the simulation of fully three-dimensional turbulent transition in a flow unstable to symmetric instability. Linear stability is also performed to understand and interpret three-dimensional effects which are manifested not only in transition to turbulence but also during the initial evolution of small-amplitude, three-dimensional disturbances.

The initial vertical vorticity fluctuations organize into structures that are inclined at approximately $-45°$ in the x_1-x_2 plane and instability currents that are misaligned with respect to the isopycnals. This behavior for $ft = \mathcal{O}(1)$ is consistent with the results of Mamatsashvili *et al.* (2010). As time advances, the horizontal scale of the flow continually increases, especially in the along-front direction, and the flow tends towards two-dimensionality. However, for sufficiently large horizontal domains, nonlinearity emerges for currents that, although near-symmetric (the angle θ with the along-front direction is roughly $5°$ in the largest domain case) are not exactly symmetric. In other words, it is the off-symmetric instability that evolves nonlinearly rather than the pure symmetric ($k_1 = 0$) instability.

Non-model linear stability analysis showed a tendency for flow to nearly align with the symmetric axis once $ft \gg 1$. The vertical scale of observed off-symmetric modes decreases with time resulting in misalignment of off-symmetric currents and isopycnals. The net effect of strong vertical shear is to make $|k_3| \gg |k_2| \gg |k_1|$ when $ft \gg 1$. The analysis shows that vertical shear stabilizes nearly-symmetric modes tilted in the direction opposite to that observed in the simulations which explains why these oppositely-tilted modes do not amplify in the simulations. For these modes, the characteristic slope k_2/k_3 increases in magnitude with time leading to currents that are steeper than the isopycnals resulting in rapid suppression. It is because of these issues that the analysis of purely symmetric instability through two-dimensional simulations may not be appropriate for strongly-sheared fronts.

Computational domains are rotated about the vertical axis to capture near-

symmetric currents in both the linear stability analysis and numerical simulations. A two-dimensional simulation rotated to be nearly aligned with off-symmetric currents found in the DNS displayed perturbation growth rates similar to those seen in a three-dimensional simulation with similarly-oriented currents. Misalignment of off-symmetric currents and isopycnals allow currents to be strengthened by both the reservoir of kinetic energy in the vertical shear and the reservoir of potential energy in the density front, simultaneously. The secondary shear instability is misaligned with the symmetric axis, implying that two dimensional simulations are unable to accurately capture secondary shear instabilities in both symmetric and off-symmetric currents.

Finally, the forward cascade from balanced vertical shear to turbulence is demonstrated using a high resolution simulation. The evolution from quiescent flow to nearly two-dimensional off-symmetric currents followed by secondary shear-convective instability is presented. Another important transitional event occurs later when vorticity fluctuations in the vertical shearing plane grow large enough for nonlinearity to overcome the stabilizing effect of stratified shear when $Ri = 0.5$ enhancing extraction of kinetic energy from the shear. This transition leads to fully three-dimensional vortical flow which rapidly becomes more multiscale until three-dimensional well-developed shear-driven turbulence emerges. Mixing is strong and increases by a factor of three after the destabilization of the shearing plane.

The contents of this chapter are in the process of being submitted for publication in the *Journal of Fluid Mechanics*. The dissertation author is the primary researcher and the research supervisor is the co-author of the paper. The authors are grateful for computational resources through a research allocation through the Extreme Science and Engineering Discovery Environment (XSEDE).

Chapter 6

Summary

Two idealized rotating and stratified flows are explored using linear stability analysis and three-dimensional direct numerical simulations. The first problem is a barotropic mean flow containing horizontally-oriented shear flow in the form of a mixing layer. The second problem concerns a uniform baroclinic mean flow in the form of a homogeneous density front in thermal wind balance with uniform vertical shear. Both flows are studied in the regime of submesoscale shear flows, with appropriate Richardson and Rossby numbers. This regime contains flows with lateral length scales of roughly 1 to 20 kilometers. The horizontal shear flow results in simultaneous inertial and barotropic instabilities provided the mixing layer vorticity is opposite in sign and substantially greater in magnitude than the Coriolis parameter. When the vorticity of the mixing layer is opposite in sign and similar in magnitude to the Coriolis parameter the barotropic instability is fundamentally altered. The vertical wavenumber associated with this new instability increases by an order of magnitude which destabilizes barotropic vortices leading to increased turbulence intensity. The presence of strong vortical fluctuations persists well outside of the inertially unstable regime is a novel result.

Symmetric instability (fluctuations have no along-front variation and are aligned with isopycnals) has been identified in the literature as a potential route to turbulence at fronts as an alternative to wind-driven boundary layer mixing. Linear analysis and simulations of a uniform baroclinic flow in initial geostrophic balance performed here suggest that the instability responsible for initiating transition to

turbulence should be near-symmetric and not exactly symmetric as predicted for asymptotically large time scales. Owing to near-symmetry, the instability fundamentally differs from the purely symmetric instability due to currents crossing surfaces of constant density and tapping the reservoir of potential energy available in the front. The presence of strong vertical shear only intensifies this effect as time increases. A highly-resolved turbulent simulation demonstrates a pathway to turbulence from quiescent flow via near-symmetric currents which succumb to shear-convective instabilities which in turn act to destabilize vorticity fluctuations aligned with the mean vorticity in the base flow. Once these fluctuations are sufficiently strong enough, the flow three-dimensionalizes and rapidly breaks down into turbulence throughout the domain.

In the future, a study investigating the development of turbulence from a flow containing both vertical and horizontal shear could help answer the fundamental question of how energy cascades to turbulence in largely balanced flows containing reservoirs of fluid with differing momentum and density. This case would complete the forward cascade proposed by Molemaker *et al.* (2010) where the largely balanced ocean interior drives local frontogenesis with strong horiztonal shear leading to efficient energy extraction by the instability mechanisms discussed throughout this thesis.

Appendix A

Modal Linear Stability Analysis Derivation

This section complements the material in chapter 3 giving details about the linear stability analysis performed in that chapter and corresponding journal publication. The rotating Boussinesq equations of motion are stated here for $\langle\rho\rangle = \rho_0 + \frac{d\langle\rho\rangle}{dx_3}x_3$ where $\frac{d\langle\rho\rangle}{dx_3}$ is constant.

$$\frac{Du_i}{Dt} + \epsilon_{i3k}fu_k = \frac{-1}{\rho_0}\frac{\partial p}{\partial x_i} - \frac{\rho' g}{\rho_0}\delta_{i3} + \nu\frac{\partial^2 u_i}{\partial x_j \partial x_j}$$
$$\frac{D\rho'}{Dt} + u_3\frac{d\langle\rho\rangle}{dx_3} = \kappa\frac{\partial^2\rho'}{\partial x_j\partial x_j} \qquad \frac{\partial u_i}{\partial x_i} = 0$$

Letting $b = -\frac{\rho'^* g\delta_\omega}{\Delta U^2}$ and using the non-dimensional parameters $Re = \frac{\Delta U\delta_{\omega,0}}{\nu}$, $Pr = \frac{\nu}{\kappa}$, $Ri_{b,0} = -\frac{g}{\rho_0}\frac{d\langle\rho\rangle}{dx_3}\frac{\delta_\omega^2}{\Delta U^2}$, and $Ro = \frac{\Delta U}{f\delta_\omega}$ one finds the following dimensionless equations

$$\frac{Du_i}{Dt} + \epsilon_{i3k}\frac{u_k}{Ro} = -\frac{\partial p}{\partial x_i} + b\delta_{i3} + \frac{1}{Re}\frac{\partial^2 u_i}{\partial x_j^2}$$
$$\frac{Db}{Dt} + Ri_b u_3 = \frac{1}{RePr}\frac{\partial^2 b}{\partial x_j^2} \qquad \frac{\partial u_i}{\partial x_i} = 0$$

Next the flow variables are decomposed into base and perturbation components as follows

$$\phi\left(x_1, x_2, x_3, t\right) = \bar{\phi}\left(x_2\right) + \phi'\left(x_1, x_2, x_3, t\right)$$

The base states we wish to investigate are those where f and N are constant and

$$\bar{u}_1\left(x_2\right) = \frac{1}{2}\tanh\left(\frac{2x_2}{\delta_\omega}\right) \qquad \bar{u}_2\left(x_2\right) = 0 \qquad \bar{u}_3\left(x_2\right) = 0$$
$$\frac{\partial \bar{p}}{\partial x_i} = \epsilon_{i3k}\frac{\bar{u}_k}{Ro} - \bar{b}\delta_{i3} \qquad \text{(hydrostatic and geostrophic balance)}$$

Substituting into the governing equations and removing terms that are quadratic one obtains

$$\frac{\partial u_1'}{\partial t} + \bar{u}_1\frac{\partial u_1'}{\partial x_1} + u_2'\frac{d\left\langle u_1\right\rangle}{dx_2} - \frac{u_2'}{Ro} = -\frac{\partial p'}{\partial x_1} + \frac{1}{Re}\left(\frac{\partial^2 u_1'}{\partial x_1^2} + \frac{\partial^2 u_1'}{\partial x_2^2} + \frac{\partial^2 u_1'}{\partial x_3^2}\right)$$
$$\frac{\partial u_2'}{\partial t} + \bar{u}_1\frac{\partial u_2'}{\partial x_1} + \frac{u_1'}{Ro} = -\frac{\partial p'}{\partial x_2} + \frac{1}{Re}\left(\frac{\partial^2 u_2'}{\partial x_1^2} + \frac{\partial^2 u_2'}{\partial x_2^2} + \frac{\partial^2 u_2'}{\partial x_3^2}\right)$$
$$\frac{\partial u_3'}{\partial t} + \bar{u}_1\frac{\partial u_3'}{\partial x_1} = -\frac{\partial p'}{\partial x_3} + b' + \frac{1}{Re}\left(\frac{\partial^2 u_3'}{\partial x_1^2} + \frac{\partial^2 u_3'}{\partial x_2^2} + \frac{\partial^2 u_3'}{\partial x_3^2}\right)$$
$$\frac{\partial u_1'}{\partial x_1} + \frac{\partial u_2'}{\partial x_1} + \frac{\partial u_3'}{\partial x_3} = 0$$
$$\frac{\partial b'}{\partial t} + \bar{u}_1\frac{\partial b'}{\partial x_1} + Ri_b u_3' = \frac{1}{Re}\left(\frac{\partial^2 b'}{\partial x_1^2} + \frac{\partial^2 b'}{\partial x_2^2} + \frac{\partial^2 b'}{\partial x_3^2}\right)$$

Infinitesimal perturbations of the form $\phi'\left(x_2\right)\exp\left(ik_1x_1 + ik_3x_3 + \sigma t\right)$ are considered. Substituting and simplifying gives

$$
\begin{aligned}
\left(\sigma + ik_1\bar{u}_1\right)u_1' + u_2'\frac{d\bar{u}_1}{dx_2} - \frac{u_2'}{Ro} &= -ik_1p' + \frac{1}{Re}\left(-\left(k_1^2+k_3^2\right) + \frac{d^2}{dx_2^2}\right)u_1' \\
\left(\sigma + ik_1\bar{u}_1\right)u_2' + \frac{u_1'}{Ro} &= -\frac{dp'}{dx_2} + \frac{1}{Re}\left(-\left(k_1^2+k_3^2\right) + \frac{d^2}{dx_2^2}\right)u_2' \\
\left(\sigma + ik_1\bar{u}_1\right)u_3' &= -ik_3p' + b' + \frac{1}{Re}\left(-\left(k_1^2+k_3^2\right) + \frac{d^2}{dx_2^2}\right)u_3' \\
ik_1u_1' + \frac{du_2'}{dx_2} + ik_3u_3' &= 0 \\
\left(\sigma + ik_1\bar{u}_1\right)b' + Ri_bu_3' &= \frac{1}{Re_0Pr}\left(-\left(k_1^2+k_3^2\right) + \frac{d^2}{dx_2^2}\right)b'
\end{aligned}
$$

Taking $\frac{\partial}{\partial x_3}$ of the buoyancy equation and substituting continuity we find

$$
\left[ik_3b'\right]\sigma = \quad Ri_bik_1u_1' + Ri_b\frac{d}{dx_2}u_2' + \left[k_1k_3\bar{u}_1 + \frac{ik_3}{RePr}\left(-\left(k_1^2+k_3^2\right) + \frac{d^2}{dx_2^2}\right)\right]b' \tag{A.1}
$$

Subtracting $\frac{\partial}{\partial x_2}$ of the x_1 momentum equation from $\frac{\partial}{\partial x_1}$ of the x_2 momentum equation drops out the pressure gradient term and gives

$$
\begin{aligned}
\left(-\frac{d}{dx_2}u_1' + ik_1u_2'\right)\sigma = &\left[ik_1\left(\frac{d\bar{u}_1}{dx_2} + \bar{u}_1\frac{d}{dx_2} - \frac{1}{Ro}\right) + \frac{\left(k_1^2+k_3^2\right)}{Re}\frac{d}{dx_2} - \frac{1}{Re}\frac{d^3}{dx_2^3}\right]u_1' \\
&+ \left[\frac{d\bar{u}_1}{dx_2}\frac{d}{dx_2} + \frac{d^2\bar{u}_1}{dx_2^2} - \frac{1}{Ro}\frac{d}{dx_2} - \frac{ik_1\left(k_1^2+k_3^2\right)}{Re} + \frac{ik_1}{Re}\frac{d^2}{dx_2^2}\right]u_2'
\end{aligned} \tag{A.2}
$$

Taking $\frac{\partial}{\partial x_1}$ of the x_1-momentum equation and adding it to $\frac{\partial}{\partial x_3}$ of the x_3-momentum equation gives

$$
\begin{aligned}
&ik_1\left(\sigma + ik_1\bar{u}_1\right)u_1' + ik_3\left(\sigma + ik_1\bar{u}_1\right)u_3' + ik_1u_2'\frac{d\bar{u}_1}{dx_2} - ik_1\frac{u_2'}{Ro} - ik_3b' \\
&\qquad - \frac{1}{Re}\left(-\left(k_1^2+k_3^2\right) + \frac{d^2}{dx_2^2}\right)\left[ik_1u_1' + ik_3u_3'\right] = \left(k_1^2+k_3^2\right)p'
\end{aligned}
$$

By continuity one finds

$$-\sigma\frac{d^2u_2'}{dx_2^2} - ik_1\frac{d\bar{u}_1}{dx_2}\frac{du_2'}{dx_2} - ik_1\bar{u}_1\frac{d^2u_2'}{dx_2^2} + ik_1\frac{du_2'}{dx_2}\frac{d\bar{u}_1}{dx_2} + ik_1u_2'\frac{d^2\bar{u}_1}{dx_2^2} - \frac{ik_1}{Ro}\frac{du_2'}{dx_2} - ik_3\frac{db'}{dx_2}$$
$$+\frac{1}{Re}\left(-\left(k_1^2+k_3^2\right)+\frac{d^2}{dx_3^2}\right)\frac{d^2u_2'}{dx_2^2} = \left(k_1^2+k_3^2\right)\frac{dp'}{dx_2}$$

Substituting the x_2 momentum equation gives

$$\left\{\left[k_1^2+k_3^2-\frac{d^2}{dx_2^2}\right]u_2'\right\}\sigma = \left[\frac{k_1^2+k_3^2}{Ro}\right]u_1' - \left[ik_3\frac{d}{dx_2}\right]b'$$
$$+\left\{ik_1\left[-\left(k_1^2+k_3^2\right)\bar{u}_1 + \bar{u}_1\frac{d^2}{dx_2^2} - \frac{d^2\bar{u}_1}{dx_2^2} + \frac{1}{Ro}\frac{d}{dx_2}\right]\right.$$
$$\left.+\frac{1}{Re}\left[2\left(k_1^2+k_3^2\right)\frac{d^2}{dx_2^2} - \left(k_1^2+k_3^2\right)^2 - \frac{d^4}{dx_2^4}\right]\right\}u_2' \tag{A.3}$$

The equations from Deloncle *et al.* (2007) are given here, where $D = \frac{d}{dx_2}$, $U = \bar{u}_1$, and $Ri_{b,0}F_h^2 = 1$. For a linear system of the form

$$A\begin{pmatrix} u_1' \\ u_2' \\ b' \end{pmatrix} = \sigma B\begin{pmatrix} u_1' \\ u_2' \\ b' \end{pmatrix}$$

A and B follow

$$A = \begin{bmatrix} 0 & ik_1\left\{U\left(D^2-k_1^2-k_3^2\right)-D^2U\right\} & ik_3D \\ ik_1\left(DU+UD\right) & D^2U+k_1^2U+DUD & 0 \\ ik_1Ri_b & Ri_bD & k_1k_3U \end{bmatrix}$$

$$B = \begin{bmatrix} 0 & k_1^2+k_3^2-D^2 & 0 \\ -D & ik_1 & 0 \\ 0 & 0 & ik_3 \end{bmatrix}$$

From equations $A.1$, $A.2$, and $A.3$ a more general A allowing for viscous flow in a rotating frame of reference is found, where $\nabla^2 = D^2 - k^2$, $f = Ro^{-1}$, $\omega_a = -DU + f$, $\nu = Re^{-1}$, and $\kappa = (RePr)^{-1}$ for compactness

$$\begin{bmatrix} -fk^2 & ik_1\left\{U\nabla^2 + D\omega_a\right\} + \nu\nabla^2 & ik_3D \\ ik_1\left(DU - \omega_a\right) - \nu\nabla^2 D & D^2U + k_1^2U - \omega_a D + \nu ik_1\nabla^2 & 0 \\ ik_1Ri_b & Ri_bD & k_1k_3U + \kappa ik_3\nabla^2 \end{bmatrix}$$

Appendix B

Horizontal Shear Layer Simulator

This flow solver evolves a three-dimensional flow field according to the incompressible Navier-Stokes equations in either a triply- or doubly-periodic domain and is written using Fortan 95. Numerical integration is accomplished using a low storage Runge-Kutta method which has 3rd order temporal accuracy. For the channel solver (two periodic directions) Fourier collocation is used in the x_1 and x_3 directions while 4th order compact difference approximations are used in the x_2 direction's collocated grid. The FFTW3 library is used to compute Fourier Transforms and MPI is used for parallelization.

B.1 Governing Equations

We wish to solve the following non-dimensional hyperbolic partial differential equations describing velocity and density fluctuation evolution

$$\begin{aligned}
\frac{\partial u_i}{\partial t} &= -\frac{\partial \left(u_i u_j\right)}{\partial x_j} - \epsilon_{ijk}\frac{\delta_{j3}}{Ro}u_k - Ri_b\delta_{i3}\rho' + \frac{1}{Re_0}\frac{\partial^2 u_i}{\partial x_j \partial x_j} - \frac{\partial p}{\partial x_i} \\
\frac{\partial \rho'}{\partial t} &= u_3 - \frac{\partial \left(\rho' u_j\right)}{\partial x_j} + \frac{1}{Re_0 Pr}\frac{\partial^2 \rho'}{\partial x_j \partial x_j}
\end{aligned}$$

The density evolution equation requires uniform vertical stratification and the problem is non-dimensionalized such that $d\left\langle\rho\right\rangle/dx_3 = 1$. Additionally, we use a dynamic pressure, p_d, which represents the physical pressure neglecting contribu-

tion of geostrophic (p_g) and hydrostatic (p_h) components as shown below.

$$p = p_d + p_h + p_g, \quad \text{where} \quad \frac{dp_h}{dx_3} = -\langle\rho\rangle\, g \quad \text{and} \quad \frac{dp_g}{dx_2} = -\frac{\langle u_1\rangle}{Ro}$$

There is no evolution equation for pressure in incompressible flows, therefore one must solve a Poisson equation to enforce continuity via pressure forces. The divergence of the Navier-Stokes equations can be expressed as

$$\begin{aligned} \frac{\partial u_i}{\partial t} &= H_i - \frac{\partial p_d}{\partial x_i} \\ \frac{\partial}{\partial t}\left[\frac{\partial u_i}{\partial x_i}\right] &= \frac{\partial H_i}{\partial x_i} - \frac{\partial^2 p_d}{\partial x_i \partial x_i} \end{aligned}$$

Where H_i represents the right hand side of the momentum equations excluding the pressure gradient term. In order for the velocity field to remain divergence-free, then the left hand side must be zero, giving

$$\frac{\partial H_i}{\partial x_i} = \frac{\partial^2 p_d}{\partial x_i \partial x_i}.$$

In order to ensure that the flow is divergence-free at the beginning of the simulation another Poisson equation must be solved. Letting u_i^* represent a divergence-free field 'near' the current velocity field u_i. Any vector field can be decomposed into a solenoidal and irrotational component. Also, any irrotational vector field can be expressed as the gradient of a scalar potential function. Therefore, for some unknown scalar function ϕ one finds

$$\begin{aligned} u_i &= u_i^* + \frac{\partial \phi}{\partial x_i} \\ \frac{\partial}{\partial x_i}\left[u_i\right] &= \frac{\partial}{\partial x_i}\left[u_i^* + \frac{\partial \phi}{\partial x_i}\right] \\ \frac{\partial u_i}{\partial x_i} &= \frac{\partial^2 \phi}{\partial x_i \partial x_i} \end{aligned}$$

After solving the above Poisson equation, velocities are updated in the following manner

$$u_i - \frac{\partial \phi}{\partial x_i} \quad \Longrightarrow \quad u_i$$

B.2 Domain Decomposition

The domain decomposition and corresponding notation are shown for a flow variable U in figure $B.1$. A pencil domain decomposition (split in two directions) offers superior scalability of domain transposes in comparison to a slab decomposition (split in one direction). MPI processes are grouped into rows and columns. Figure $B.2$ shows the orientation of data with respect to rows and columns for each configuration used in the channel solver. A transpose from x_1 oriented pencils to x_3 oriented pencils (and vice versa) is not included in physical space because contiguous data in the x_3 direction is never needed in physical space. Also, there is no complex transpose between x_1 and x_2 pencils because FFTs are always performed first in the x_1 direction, then the x_3 direction, and finally in the x_2 direction, when necessary. The number of rows and columns do not have to be equal, but it is recommended for optimal scalability. NX and NZ must be divisible by the number of columns and all three grid dimensions must be divisible by the number of rows.

Two MPI routines are needed to perform domain transposes using pencil decomposition, ALLTOALL and COMM_SPLIT. ALLTOALL scatters data and then gathers data to and from every process in a communicator. If process 0 contained the array $\{0, 1\}$ and process 1 contained the array $\{2, 3\}$ perfoming ALLTOALL on integer elements would yield the array $\{0, 2\}$ on process 0 and $\{1, 3\}$ on process 1. This is shown in Figure B.3. Here, ALLTOALL is used to transform from being contiguous in the x_1 direction to being contiguous in the x_3 direction. The domain is split into quadrants and the number centered in the quadrant indicates which process will receive its data during the ALLTOALL call.

When using pencil decomposition, all processes do not need to communicate with each other during transposing. Instead, only a single row or single column of processes must communicate, meaning that the transpose operation can be

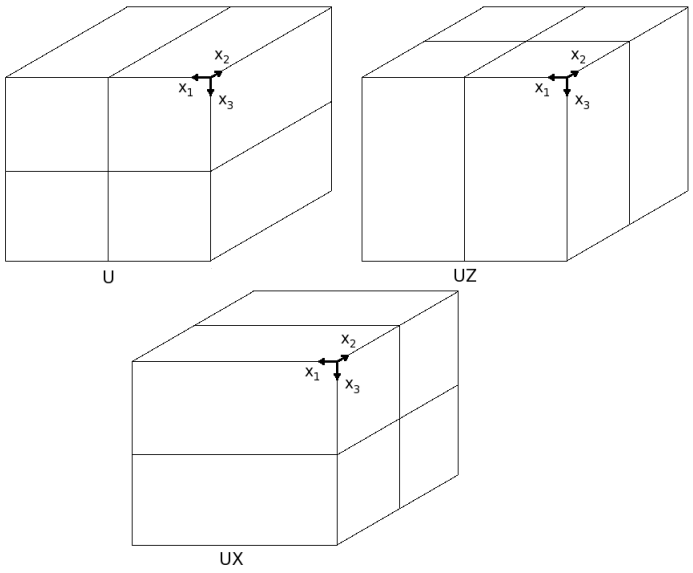

Figure B.1: Domain decomposition, for a generic flow variable U. X indicates the domain is contiguous in the x_1 direction.Z indicates the domain is contiguous in the x_3 direction. Otherwise, the domain is contiguous in the x_2 direction.

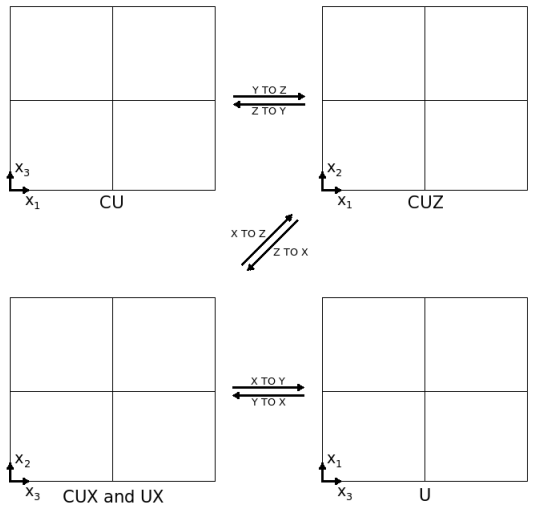

Figure B.2: How data is stored across rows and columns of processes.

parallelized across rows if only columns are communicating and vice versa. The COMM_SPLIT subroutine allows for the division of COMM_WORLD into groups of individual rows or columns of processes. Figure B.4 shows how processes are split into colors (white and gray) allowing independent transpose operations to be performed in parallel.

B.3 Temporal Integration

Our algorithm employs a low storage third order Runge-Kutta scheme (Williamson, 1980), which approximates the solution for a system of ordinary differential equations of the form

$$\frac{\partial \phi_i}{\partial t} = f_i\left(\phi_i\right).$$

The method is given by

$$\begin{aligned} F_i &= f_i\left(\phi_i\right) & \phi_i &= \phi_i + \Delta t \beta_1 F_i \\ F_i &= \zeta_2 F_i + f_i\left(\phi_i\right) & \phi_i &= \phi_i + \Delta t \beta_2 F_i \\ F_i &= \zeta_3 F_i + f_i\left(\phi_i\right) & \phi_i &= \phi_i + \Delta t \beta_3 F_i \end{aligned}$$

Where $\beta_1 = 1/3$, $\beta_2 = 15/16$, $\beta_3 = 8/15$, $\zeta_2 = -5/9$, and $\zeta_3 = -153/128$. As seen above, there are two global variables required to march forward in time for every flow variable. In our algorithm, u_i and ρ' store the values of the variables from the previous RK substep and F_i and $F_{\rho'}$ build the right hand side of the momentum equations and fluctuating density advection-diffusion equation.

B.4 Channel Solver Algorithm

This algorithm is pseudo-spectral, meaning that non-linear terms are computed in physical space, while derivatives are calculated in Fourier space. When explaining the algorithm, a hat over a variable indicates that it is in Fourier space. It is recommended that the number of points in the periodic directions be powers

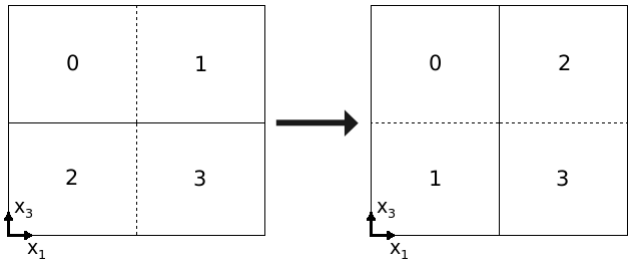

Figure B.3: ALLTOALL example : Originally domain is divided in the x_3 direction, but then the domain divided in x_1. Numbers indicate subdomains while solid lines indicate processor boundaries and dashed lines separate subdomains.

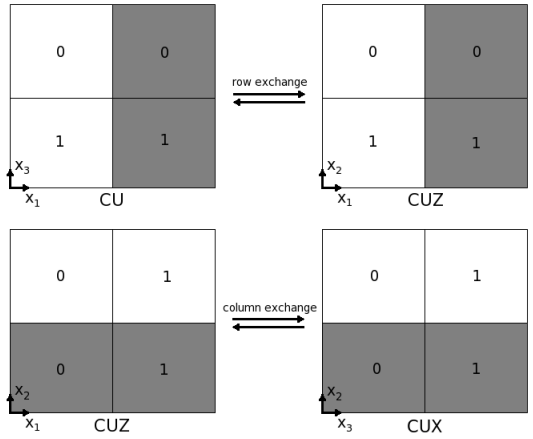

Figure B.4: When transposing using pencil decomposition parallelization can be accomplished across different colored groups as shown for two different transposing operations. Numbers indicate ranks of processes within rows or columns.

of 2, but FFTW3 has efficient specialized algorithms for FFTs on vectors whose length is of the form $2^a 3^b 5^c 7^d 11^e 13^f$ where $e + f \leq 1$. Fourier and inverse Fourier transforms are performed one direction at a time. The operations performed during conversion the flow variables to and from Fourier space is given below where the C prefix indicates complex arrays :

$$U \overset{\text{transpose}}{\Longleftrightarrow} UX \overset{\text{FFT in x}}{\Longleftrightarrow} CUX \overset{\text{transpose}}{\Longleftrightarrow} CUZ \overset{\text{FFT in z}}{\Longleftrightarrow} CUZ \overset{\text{transpose}}{\Longleftrightarrow} CU. \tag{B.1}$$

Here, the channel solver algorith will be overviewed showing the details of each Runga-Kutta substep. If $rk > 1$, where rk is the current Runge-Kutta substep (1, 2 or 3), then multiply the F from the previous RK step by ζ, otherwise define flow variables as zero.

$$\hat{F}_i = \zeta_{rk} \hat{F}_i \qquad \hat{F}_{\rho'} = \zeta_{rk} \hat{F}_{\rho'}$$

Begin building right hand side of evolution equations, store buoyancy and Coriolis terms in $\hat{F}_i$

$$\begin{aligned} \hat{F}_1 &= \hat{F}_1 + \frac{\hat{u}_2}{Ro} \\ \hat{F}_2 &= \hat{F}_2 - \frac{\hat{u}_1}{Ro} \\ \hat{F}_3 &= \hat{F}_3 - Ri_b \hat{\rho}' \end{aligned}$$

Add vertical velocity to right hand side in $\hat{F}_{\rho'}$ to force fluctuating scalar equation(s).

$$\hat{F}_{\rho'} = \hat{F}_{\rho'} + \hat{u}_3$$

Add viscous terms to right hand side for each flow variable, ϕ_i. Derivatives in the x_2 direction are computed using compact differencing (discussed in section B.5).

$$\hat{S}_1 = \frac{\delta^2 \hat{\phi}_i}{\delta x_2 \delta x_2}, \qquad \hat{F}_1 = \hat{F}_i + \frac{1}{Re_0} \left[\hat{S}_1 - \left(k_1^2 + k_3^2 \right) \hat{\phi}_i \right]$$

Nonlinear terms are computed in physical space implying variables must be converted to physical space. First, we transpose the domain from pencils in the x_2 direction ($\hat{\phi}_i$) to pencils in the x_3 direction ($\hat{\phi}_i^z$) and then perform inverse FFTs in the z direction. Then transpose from pencils in the x_3 direction to pencils in the x_1 direction ($\hat{\phi}_i^x$) and convert to physical space using inverse FFTs (ϕ_i^x) before computation of nonlinear terms. The term v_2 is the contravariant velocity which gives the value of velocity at locations halfway between collocated grid points.

$$\hat{u}_i \to \hat{u}_i^z \to \hat{u}_i^x \to u_i^x, \qquad \hat{v}_2 \to \hat{v}_2^z \to \hat{v}_2^x \to v_2^x, \qquad \hat{\rho}' \to \hat{\rho}'^z \to \hat{\rho}'^x \to \rho'^x$$

Add nonlinear terms located at collocated points to $\hat{F}$

$$\begin{aligned}
S_1^x &= u_1^x u_1^x, \qquad S_1^x \to \hat{S}_1^x \to \hat{S}_1^z \to \hat{S}_1, \qquad \hat{F}_1 = \hat{F}_1 - ik_1\hat{S}_1 \\
S_1^x &= u_3^x u_3^x, \qquad S_1^x \to \hat{S}_1^x \to \hat{S}_1^z \to \hat{S}_1, \qquad \hat{F}_3 = \hat{F}_3 - ik_3\hat{S}_1 \\
S_1^x &= u_1^x u_2^x, \qquad S_1^x \to \hat{S}_1^x \to \hat{S}_1^z \to \hat{S}_1, \qquad \hat{F}_2 = \hat{F}_2 - ik_1\hat{S}_1 \\
S_1^x &= u_1^x u_3^x, \qquad S_1^x \to \hat{S}_1^x \to \hat{S}_1^z \to \hat{S}_1, \qquad \hat{F}_1 = \hat{F}_1 - ik_3\hat{S}_1, \\
&\qquad\qquad\qquad\qquad\qquad\qquad\qquad\qquad\qquad\qquad\qquad\qquad \hat{F}_3 = \hat{F}_3 - ik_1\hat{S}_1 \\
S_1^x &= u_2^x u_3^x, \qquad S_1^x \to \hat{S}_1^x \to \hat{S}_1^z \to \hat{S}_1, \qquad \hat{F}_2 = \hat{F}_2 - ik_3\hat{S}_1 \\
S_1^x &= u_1^x \rho'^x, \qquad S_1^x \to \hat{S}_1^x \to \hat{S}_1^z \to \hat{S}_1, \qquad \hat{F}_{\rho'} = \hat{F}_{\rho'} - ik_1\hat{S}_1 \\
S_1^x &= u_2^x \rho'^x, \qquad S_1^x \to \hat{S}_1^x \to \hat{S}_1^z \to \hat{S}_1, \qquad \hat{F}_{\rho'} = \hat{F}_{\rho'} - \frac{\delta\hat{S}_1}{\delta x_2} \\
S_1^x &= u_3^x \rho'^x, \qquad S_1^x \to \hat{S}_1^x \to \hat{S}_1^z \to \hat{S}_1, \qquad \hat{F}_{\rho'} = \hat{F}_{\rho'} - ik_3\hat{S}_1
\end{aligned}$$

Nonlinear terms in the momentum equations requiring derivatives in the transverse direction are calculated at face center points (halfway between collocated points). Collocated variables are interpolated using cubic interpolation, but first transposing must be performed because variables are currently split across the x_2 direction and we wish to interpolate in that direction. Note that the compact differencing stencil is modified for these lateral derivatives because the derivative of nonlinear

products on face center points is desired at collocated points.

$$
\begin{aligned}
& u_i^x \to u_i, \qquad v_2^x \to v_2 \\
S_1 \;=\; & v_2\tilde{u}_1, \qquad S_1 \to \qquad S_1^x \to \hat{S}_1^x \to \hat{S}_1^z \to \hat{S}_1, \qquad \hat{F}_1 = \hat{F}_1 - \frac{\delta \hat{S}_1}{\delta x_2} \\
S_1 \;=\; & v_2\tilde{u}_2, \qquad S_1 \to \qquad S_1^x \to \hat{S}_1^x \to \hat{S}_1^z \to \hat{S}_1, \qquad \hat{F}_2 = \hat{F}_2 - \frac{\delta \hat{S}_1}{\delta x_2} \\
S_1 \;=\; & v_2\tilde{u}_3, \qquad S_1 \to \qquad S_1^x \to \hat{S}_1^x \to \hat{S}_1^z \to \hat{S}_1, \qquad \hat{F}_3 = \hat{F}_3 - \frac{\delta \hat{S}_1}{\delta x_2} \\
& u_i \to u_i^x, \qquad v_2 \to v_2^x
\end{aligned}
$$

Here, cubic interpolation is accomplished using the following stencil (for a uniform x_2-grid) where integral indices indicate locations on the collocated grid and fractional indices indicate locations on the contravariant grid.

$$
\tilde{\phi_j} \;=\; -\frac{1}{16}\phi_{j-3/2} + \frac{9}{16}\phi_{j-1/2} + \frac{9}{16}\phi_{j+1/2} - \frac{1}{16}\phi_{j+3/2}
$$

Convert variables back to Fourier space

$$
u_i^x \to \hat{u}_i^x \to \hat{u}_i^z \to \hat{u}_i, \qquad v_2^x \to \hat{v}_2^x \to \hat{v}_2^z \to \hat{v}_2, \qquad \rho'^x \to \hat{\rho}'^x \to \hat{\rho}'^z \to \hat{\rho}'
$$

Next pressure is computed and pressure gradient terms are added to $\hat{F}$

$$
-\left(k_x^2 + k_z^2\right)\hat{p}_d + \frac{\delta^2 \hat{p}_d}{\delta x_2 \delta x_2} \;=\; ik_1\hat{F}_1 + \frac{\delta \hat{F}_2}{\delta x_2} + ik_3\hat{F}_3
$$

Boundary conditions for pressure are Neumann with slope set to zero for all fluctuating components. The mean pressure ($k_1 = 0, k_3 = 0$) is set to zero at both x_2 boundaries.

$$
\hat{F}_1 = \hat{F}_1 - ik_1\hat{p}_d, \qquad \hat{F}_2 = \hat{F}_2 - \frac{\delta \hat{p}_d}{\delta x_2}, \qquad \hat{F}_3 = \hat{F}_3 - ik_3\hat{p}_d
$$

Lastly, velocity and scalar fields are damped using a Rayleigh damping function near x_2 boundaries, note that the $k_x = 0$ and $k_z = 0$ component of $\hat{F}_1$ is treated differently so that the mean $\hat{u}_1$ relaxes to $\pm\frac{1}{2}$ as expected for the shear layer. This

is performed after the pressure solve to minimize its impact on the rest of the flow domain. Any divergence that may result in the flow field is then projected out in the projection step after each RK substep.

$$\hat{F}_1(0,0,x_2) = \hat{F}_1(0,0,x_2) - \sigma(x_2)\left[\hat{u}_1(0,0,x_2) - \frac{x_2}{2\|x_2\|}\right]$$

$$\hat{F}_i = \hat{F}_i - \sigma(x_2)\,\hat{\phi}_i$$

Where the Rayleigh damping function takes the following form for sponge thickness a

$$\sigma(x_2) = \begin{cases} (\beta_{rk}\Delta t)^{-1}\exp\left[(a - x_2 - L/2)/a\right] & \text{if } -\frac{L}{2} < x_2 < -\frac{L}{2} + a \\ (\beta_{rk}\Delta t)^{-1}\exp\left[(a + x_2 - L/2)/a\right] & \text{if } \frac{L}{2} - a < x_2 < \frac{L}{2} \\ 0 & \text{otherwise} \end{cases}$$

Update flow variables

$$\hat{\phi}_i = \hat{\phi}_i + \beta_{rk}\Delta t\hat{F}_i$$

The contravariant velocity (v_2) is calculated using cubic interpolation of u_2. Divergence is removed from the velocity field by solving the following implicit equation

$$-\left(k_x^2 + k_z^2\right)\hat{\phi} + \frac{\delta^2\hat{\phi}}{\delta x_2 \delta x_2} = ik_x\hat{u}_1 + \underline{\frac{\delta\hat{v}_2}{\delta x_2}} + ik_z\hat{u}_3$$

Note that the contravariant velocity is used in place of the collocated value. Where $\delta\hat{v}_2/\delta x_2$ differentiates over Δx_2 instead of $2\Delta x_2$ because $\hat{\phi}$ takes values at cell centers and $\hat{v}_2$ at face centers. Next the divergence is projected away from the velocity field, including the contravariant velocity.

$$\hat{u}_1 = \hat{u}_1 - ik_x\hat{\phi}, \qquad \hat{u}_3 = \hat{u}_3 - ik_z\hat{\phi}, \qquad \hat{u}_2 = \hat{u}_2 - \frac{\delta\hat{\phi}}{\delta x_2}, \qquad \underline{\hat{v}_2 = \hat{v}_2 - \frac{\delta\hat{\phi}}{\delta x_2}}$$

Again, here the $\delta\hat{\phi}/\delta x_2$ term used to update $\hat{v}_2$ differentiates over Δx_2. This way

fluctuations in $\hat{v}_2$ with wavelength $2\Delta x_2$ affect $\hat{\phi}$ and vice versa. This prevents artificial $2\Delta x_2$ wavelength oscillations from forming as are commonly an issue in algorithms using collocated grids. There is also a triply periodic algorithm, but it is not included here due to its lack of relevance to the work contained herein.

B.5 Differentiation

When 4th order compact finite differencing is applied to a uniform Cartesian grid then the finite difference stencils are calculated as follows

$$\begin{aligned}
\frac{1}{6}\left(\frac{\delta\hat{f}}{\delta x_2}\right)_{j+1} + \frac{2}{3}\left(\frac{\delta\hat{f}}{\delta x_2}\right)_{j} + \frac{1}{6}\left(\frac{\delta\hat{f}}{\delta x_2}\right)_{j-1} &= \frac{\hat{f}_{j+1} - \hat{f}_{j-1}}{2\Delta x_2} \\
\frac{1}{24}\left(\frac{\delta\hat{f}}{\delta x_2}\right)_{j+1} + \frac{11}{12}\left(\frac{\delta\hat{f}}{\delta x_2}\right)_{j} + \frac{1}{24}\left(\frac{\delta\hat{f}}{\delta x_2}\right)_{j-1} &= \frac{\hat{f}_{j+1/2} - \hat{f}_{j-1/2}}{\Delta x_2} \\
\frac{1}{12}\left(\frac{\delta^2\hat{f}}{\delta x_2^2}\right)_{j+1} + \frac{5}{6}\left(\frac{\delta^2\hat{f}}{\delta x_2^2}\right)_{j} + \frac{1}{12}\left(\frac{\delta^2\hat{f}}{\delta x_2^2}\right)_{j-1} &= \frac{\hat{f}_{j+1} - 2\hat{f}_j + \hat{f}_{j-1}}{\Delta x_2^2}
\end{aligned}$$

Where the second scheme is used when derivatives at cell centers are computed using values at face centers or vice versa.

When solving a Poisson equation of the form $\nabla^2\phi = f$ with two periodic directions one observes

$$-\left(k_x^2 + k_z^2\right)\hat{\phi}_j + \left(\frac{\delta^2\hat{\phi}}{\delta x_2^2}\right)_j = \hat{f}_j \tag{B.2}$$

Substituting the 4th order Pade formula gives

$$-\left(k_x^2 + k_z^2\right)\hat{\phi}_j - \frac{1}{10}\left(\frac{\delta^2\hat{\phi}}{\delta x_2^2}\right)_{j+1} - \frac{1}{10}\left(\frac{\delta^2\hat{\phi}}{\delta x_2^2}\right)_{j-1} + \frac{6}{5\left(\Delta x_2\right)^2}\left(\hat{\phi}_{j+1} - 2\hat{\phi}_j + \hat{\phi}_{j-1}\right) = \hat{f}_j$$

Substituting equation B.2 and simplifying gives

$$\begin{aligned} &-\left[\frac{1}{10}\left(k_x^2+k_z^2\right)-\frac{6}{5\left(\Delta x_2\right)^2}\right]\hat{\phi}_{j+1} \\ &\quad -\left[\left(k_x^2+k_z^2\right)+\frac{12}{5\left(\Delta x_2\right)^2}\right]\hat{\phi}_j \\ &-\left[\frac{1}{10}\left(k_x^2+k_z^2\right)-\frac{6}{5\left(\Delta x_2\right)^2}\right]\hat{\phi}_{j-1} \quad = \tfrac{1}{10}\hat{f}_{j+1}+\hat{f}_j+\tfrac{1}{10}\hat{f}_{j-1} \end{aligned}$$

B.6 Initial Conditions

Two dimensional initial conditions are prescribed in the following manner for a prescribed energy spectrum, $E(k)$. Here * indicates a complex conjugate. For a periodic two dimensional flow the following is observed

$$\begin{aligned} & k_1\hat{u}_1(k_1,k_2)+k_2\hat{u}_2(k_1,k_2)=0 \\ E(k) &= \int \hat{u}_1\hat{u}_1^*(k_1,k_2)+\hat{u}_2\hat{u}_2^*(k_1,k_2)\,dA(k) \\ E(k) &= \sum_{k\approx\sqrt{k_1^2+k_2^2}} \hat{u}_1\hat{u}_1^*(k_1,k_2)+\frac{k_1^2}{k_2^2}\hat{u}_1\hat{u}_1^*(k_1,k_2)\,4\pi k^2 \\ E(k) &= \sum_{k\approx\sqrt{k_1^2+k_2^2}} \left[1+\frac{k_1^2}{k_2^2}\right]\hat{u}_1\hat{u}_1^*(k_1,k_2)\,4\pi k^2 \end{aligned}$$

Letting θ be a random number on the interval $[0,2\pi)$ and N_b represent the number of discrete combinations of k_1 and k_2 values that approximately yield the discrete

wavenumber value k. The following relation results for $\hat{u}_1 = C(k_1, k_2)\exp(i\theta)$

$$\begin{aligned} E(k) &= \sum_{k\approx\sqrt{k_1^2+k_2^2}} \left[1 + \frac{k_1^2}{k_2^2}\right] C^2(k_1, k_2)\, 4\pi k^2 \\ C(k_1, k_2) &= \sqrt{\frac{E(k)}{4\pi k^2 N_b \left[1 + k_1^2 k_2^{-2}\right]}} \\ \hat{u}_1 &= C(k_1, k_2)\exp(i\theta) \\ \hat{u}_2 &= -\frac{k_1 C(k_1, k_2)}{k_2}\exp(i\theta) \end{aligned}$$

Three dimensional initial conditions are prescribed in a similar manner following Rogallo (1981). For random numbers θ_1, θ_2 and ϕ on the interval $[0, 2\pi)$, $k_h = \sqrt{k_1^2 + k_2^2}$ and $k = \sqrt{k_i^2}$

$$\alpha = \left(\frac{E(k)}{4\pi k^2}\right)^{1/2} \exp(i\theta_1)\cos\phi, \qquad \beta = \left(\frac{E(k)}{4\pi k^2}\right)^{1/2} \exp(i\theta_2)\sin\phi$$

$$\hat{u}_1 = \frac{\alpha k k_2 + \beta k_1 k_3}{k k_h}, \qquad \hat{u}_2 = \frac{\beta k_2 k_3 - \alpha k k_1}{k k_h}, \qquad \hat{u}_3 = \frac{\beta k_h}{k}$$

B.7 Validation

Validation of the algorithm was performed though analysis of shear layer statistics with and without stratification. The unstratified shear layer was simulated at $Re_0 = 681$ and various statistics were examined include growth rate and turbulent kinetic energy (TKE) budget. The TKE budget is shown in Figure B.5 and compares well to the values shown in figure 5 of Brucker & Sarkar (2007) which also contains values from TKE budgets of Rogers & Moser (1994) and Pantano & Sarkar (2002). The budget very nearly closes, with the faint line with x symbols near the $\partial K/\partial t$ term representing the sum of the right hand side terms from the TKE evolution equation, $P - \epsilon - \partial T/\partial x_2$.

Another simulation was performed with stratification ($Ri_{b,0} = 1.13$) at the same Reynolds number. Validation was more thorough in this case where qualita-

tive agreement of vortical structures in addition to statistics was examined against prior results for the horizontal shear layer (Basak & Sarkar, 2006; Arobone & Sarkar, 2010). A similar vortical evolution from three dimensional turbulence to quasi-vertical vortices then pancake vortices was observed. The TKE budgets (Figure B.6) closed very well for the stratified simulation and nearly matched figure 8 (b) of (Arobone & Sarkar, 2010).

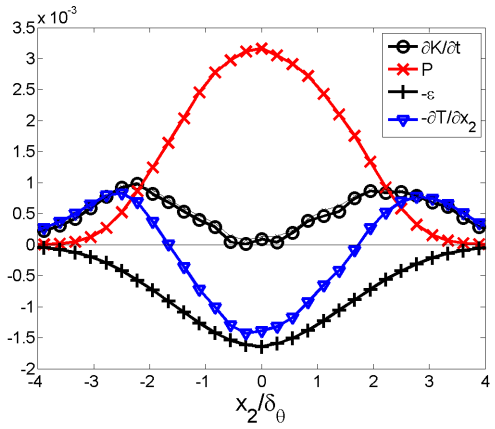

Figure B.5: TKE budget for unstratified shear layer when centerline $dk/dt \approx 0$. $Re_0 = 681$

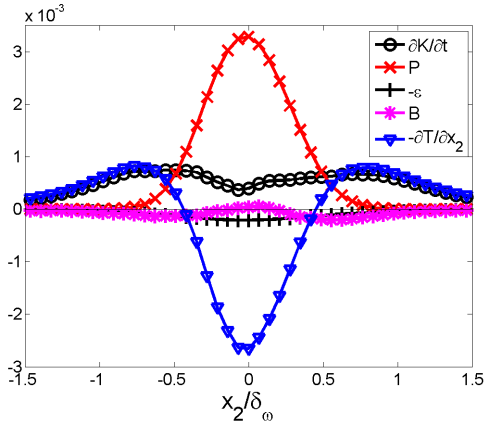

Figure B.6: TKE budget for stratified shear layer at $t = 50.43$. $Re_0 = 681$, $Ri_b = 1.132$, and $Pr = 1$

Appendix C

Ocean Front Simulator

This flow solver evolves a three-dimensional flow field according to the incompressible Navier-Stokes equations in a domain which is periodic in either one or two directions. The code is designed to evolve rotating Boussinesq flows on a regular nearly isotropic grid as accurately and efficiently as possible and is written using Fortran 95. Numerical integration is accomplished using a low storage Runge-Kutta method which has third order temporal accuracy. Sixth order compact difference approximations and interpolation are used in the x_2 and x_3 directions' staggered grids. A two-dimensional parallelized fourth-order multigrid solver is used to compute pressure and project away divergence. The FFTW3 library is used to compute Fast Fourier Transforms and MPI is used for parallelization.

C.1 Governing Equations

We wish to solve the following non-dimensional hyperbolic partial differential equations describing velocity and density fluctuation evolution

$$\frac{\partial u_i}{\partial t} = f_i = -\frac{\partial \left(u_i u_j\right)}{\partial x_j} + \frac{\epsilon_{ij3}}{Ro} u_j - \delta_{i3}\rho + \frac{1}{RoEk}\frac{\partial^2 u_i}{\partial x_j \partial x_j} - \frac{\partial p}{\partial x_i}$$
$$\frac{\partial \rho}{\partial t} = f_\rho = -\frac{\partial \left(\rho u_j\right)}{\partial x_j} + \frac{1}{RoEkPr}\frac{\partial^2 \rho}{\partial x_j \partial x_j}$$

There is no evolution equation for pressure in incompressible flows so instead a Poisson equation must be solved. The divergence of the Navier-Stokes equations can be expressed as

$$\begin{aligned} \frac{\partial u_i}{\partial t} &= H_i - \frac{\partial p}{\partial x_i} \\ \frac{\partial}{\partial t}\left[\frac{\partial u_i}{\partial x_i}\right] &= \frac{\partial H_i}{\partial x_i} - \frac{\partial^2 p}{\partial x_i \partial x_i} \end{aligned}$$

Where H_i represents the right hand side of the momentum equations excluding the pressure gradient term. In order for the velocity field to remain divergence-free, then the left hand side must be zero, giving

$$\frac{\partial^2 p}{\partial x_i \partial x_i} = \frac{\partial H_i}{\partial x_i}$$

In order to remove divergence from the flow field a different Poisson equation must be solved. Any vector field can be decomposed into solenoidal ($\nabla \cdot \mathbf{u} = 0$) and irrotational ($\nabla \times \mathbf{u} = \mathbf{0}$) components. Also, any irrotational vector field can be expressed as the gradient of a scalar potential function (ϕ). Therefore, for some unknown scalar function ϕ one finds

$$u_i = u_i^* + \frac{\partial \phi}{\partial x_i}$$

Where u_i^* represents a divergence-free field 'near' the current velocity field u_i. Taking the divergence of both sides gives the following process for removing divergence

$$\frac{\partial^2 \phi}{\partial x_i \partial x_i} = \frac{\partial u_i}{\partial x_i} \qquad \rightarrow \qquad u_i^* = u_i - \frac{\partial \phi}{\partial x_i}$$

C.2 Domain Decomposition

The domain decomposition and corresponding notation are shown for a flow variable u in Figure C.1. The use of transposing allows for better scalability of the parallel algorithm by greatly limiting the number of ghost cell data transfers needed. Domain transposing allows data to be contiguous in the periodic direction

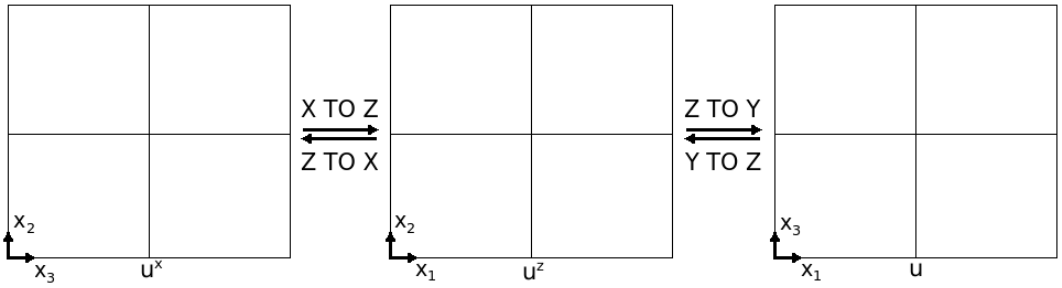

Figure C.1: How data is stored across rows and columns of processes and what routines are used to change domain decomposition.

during FFTs or contiguous in the direction of finite difference derivative calculations, as necessary. The multigrid scalability is not significantly inhibited because one of the two directions is contiguous during multigrid iterations. When using pencil decomposition, all processes do not need to communicate with each other during transposing. Instead, only a single row or single column of processes must communicate, meaning that the transpose can be parallelized across rows if only columns are communicating and vice versa.

MPI processes are grouped into rows (NR) and columns (NC). Figure C.1 shows the orientation of data with respect to rows and columns for each configuration used in the duct solver. Transposes are available to change between all three data layouts for real or complex data. The number of rows (NR) and columns (NC) do not have to be equal, but it is recommended for optimal scalability. NX and NZ must be divisible by NC while NY and NZ must be divisible by NR.

Two MPI routines are needed to perform domain transposes using pencil decomposition, ALLTOALL and COMM_SPLIT. ALLTOALL scatters data and then gathers data to and from every process in a communicator. If process 0 contained the array $\{0, 1\}$ and process 1 contained the array $\{2, 3\}$ perfoming ALLTOALL on integer elements would yield the array $\{0, 2\}$ on process 0 and $\{1, 3\}$ on process 1.

C.3 Temporal Integration

The algorithm employs a low storage third order Runge-Kutta scheme (Williamson,1980), which approximates the solution for a system of ordinary differential equations of the form

$$\frac{\partial \phi_i}{\partial t} = f_i\left(\phi_i\right).$$

The method is given by

$$\begin{aligned} F_i &= f_i\left(\phi_i\right) & \phi_i &= \phi_i + \Delta t \beta_1 F_i \\ F_i &= \zeta_2 F_i + f_i\left(\phi_i\right) & \phi_i &= \phi_i + \Delta t \beta_2 F_i \\ F_i &= \zeta_3 F_i + f_i\left(\phi_i\right) & \phi_i &= \phi_i + \Delta t \beta_3 F_i \end{aligned}$$

Where $\beta_1 = 1/3$, $\beta_2 = 15/16$, $\beta_3 = 8/15$, $\zeta_2 = -5/9$, and $\zeta_3 = -153/128$. As seen above, there are two global variables required to march forward in time for every flow variable. In our algorithm, u_i and ρ' store the values of the variables from the previous RK substep and F_i and F_ρ build the right hand side of the momentum equations and fluctuating density evolution equation, respectively.

C.4 Duct Solver Algorithm

This algorithm is pseudo-spectral with non-linear terms and derivatives in non-periodic directions computed in physical space, while derivatives in the periodic direction are calculated in Fourier space. When explaining the algorithm, a hat over a variable indicates that it is in Fourier space. It is recommended that the number of points in the periodic directions be powers of 2, but FFTW3 has efficient specialized algorithms for FFTs on vectors whose length is of the form $2^a 3^b 5^c 7^d 11^e 13^f$ where $e + f \leq 1$. Fourier and inverse Fourier transforms are performed only when data is contiguous in the periodic direction (x_1).

In this section the duct solver algorithm will be overviewed showing the details of each Runga-Kutta substep.

If $(rk > 1)$ then multiply the F from the previous RK step by ζ_{rk}, otherwise define as zero.

$$F_i^x = \zeta_{rk} F_i^x \qquad F_\rho^x = \zeta_{rk} F_\rho^x$$

Add nonlinear divergence terms involving x_1 derivatives to $\hat{F}^x$. First interpolate u_1 to staggered points using R_2 and R_3.

$$\begin{aligned} S_1^x &= u_1^x u_1^x, & S_1^x &\to \hat{S}_1^x, & \hat{F}_1^x &= \hat{F}_1^x - ik_x \hat{S}_1^x \\ S_1^x &= u_1^x \rho^x, & S_1^x &\to \hat{S}_1^x, & \hat{F}_\rho^x &= \hat{F}_\rho^x - ik_x \hat{S}_1^x \end{aligned}$$

$$u_1^x \to u_1^z, \quad R_3^z = \frac{\delta^0 u_1}{\delta x_3^0}, \quad u_1^z \to u_1, \quad R_2 = \frac{\delta^0 u_1}{\delta x_2^0}$$
$$R_3^z \to R_3^x, \quad R_2 \to R_2^z \to R_2^x, \quad u_1 \to u_1^z \to u_1^x$$

$$\begin{aligned} S_1^x &= R_2^x v_2^x, & S_1^x &\to \hat{S}_1^x, & \hat{F}_2^x &= \hat{F}_2^x - ik_x \hat{S}_1^x \\ S_1^x &= R_3^x v_3^x, & S_1^x &\to \hat{S}_1^x, & \hat{F}_3^x &= \hat{F}_3^x - ik_x \hat{S}_1^x \end{aligned}$$

Transpose such that flow variables (and right hand side, F) are contiguous in the x_2 direction then add $\partial^2/\partial x_2^2$ viscous terms and nonlinear terms involving x_2 derivatives to right hand side

$$u_i^x \to u_i^z \to u_i, \quad v_2^x \to v_2^z \to v_2, \quad \rho^x \to \rho^z \to \rho$$
$$\hat{F}_i^x \to F_i^x \to F_i^z \to F_i, \quad \hat{F}_\rho^x \to F_\rho^x \to F_\rho^z \to F_\rho$$

Boundary conditions should be enforced at $x_2 = 0$ and $x_2 = L_y$ boundaries at this point in the algorithm.

$$\begin{aligned} S_1 &= \frac{\delta^2 u_1}{\delta x_2^2}, \quad F_1 = F_1 + \frac{S_1}{Re_0} & S_1 &= \frac{\delta^2 u_2}{\delta x_2^2}, \quad F_2 = F_2 + \frac{S_1}{Re_0} \\ S_1 &= \frac{\delta^2 u_3}{\delta x_2^2}, \quad F_3 = F_3 + \frac{S_1}{Re_0} & S_1 &= \frac{\delta^2 \rho}{\delta x_2^2}, \quad F_\rho = F_\rho + \frac{S_1}{Re_0 Pr} \end{aligned}$$

$$R_1 = \frac{\delta^0 u_1}{\delta x_2^0}, \qquad R_3 = \frac{\delta^0 v_3}{\delta x_2^0}$$
$$v_2 \to v_2^z, \qquad R_2^z = \frac{\delta^0 v_2^z}{\delta x_3^0}, \qquad v_2^z \to v_2, \qquad R_2^z \to R_2$$

$$S_1 = u_2\rho, \quad F_\rho = F_\rho - \frac{\delta S_1}{\delta x_2} \qquad S_1 = v_2 R_1, \quad F_1 = F_1 - \frac{\delta S_1}{\delta x_2}$$
$$S_1 = u_2^2, \quad F_2 = F_2 - \frac{\delta S_1}{\delta x_2} \qquad S_1 = R_2 R_3, \quad F_3 = F_3 - \frac{\delta S_1}{\delta x_2}$$

Then flow variables (also F_i and F_ρ) are transposed from pencils in the x_2 direction to pencils in the x_3 direction to add contribution of $\partial^2/\partial x_3^2$ viscous terms and nonlinear terms involving x_3 derivatives

$$u_i \to u_i^z, \qquad v_3^x \to v_3^z, \qquad \rho \to \rho^z, \qquad F_i \to F_i^z$$
$$F_\rho \to F_\rho^z, \qquad R_2 \to R_2^z, \qquad R_3 \to R_3^z$$

Boundary conditions should be enforced at $x_3 = 0$ and $x_3 = L_z$ boundaries at this point in the algorithm.

$$S_1^z = \frac{\delta^2 u_1^z}{\delta x_3^2}, \quad F_1^z = F_1^z + \frac{S_1^z}{RoEk} \qquad S_1^z = \frac{\delta^2 u_2^z}{\delta x_3^2}, \quad F_2^z = F_2^z + \frac{S_1^z}{RoEk}$$
$$S_1^z = \frac{\delta^2 u_3^z}{\delta x_3^2}, \quad F_3^z = F_3^z + \frac{S_1^z}{RoEk} \qquad S_1^z = \frac{\delta^2 \rho^z}{\delta x_3^2}, \quad F_\rho^z = F_\rho^z + \frac{S_1^z}{RoEkPr}$$

$$R_1^z = \frac{\delta^0 u_1^z}{\delta x_3^0}$$

$$S_1^z = u_3^z \rho^z, \quad F_\rho^z = F_\rho^z - \frac{\delta S_1^z}{\delta x_3} \qquad S_1^z = v_3^z R_1^z, \quad F_1^z = F_1^z - \frac{\delta S_1^z}{\delta x_3}$$
$$S_1^z = R_3^z R_2^z, \quad F_2^z = F_2^z - \frac{\delta S_1^z}{\delta x_3} \qquad S_1^z = \left(u_3^z\right)^2, \quad F_3^z = F_3^z - \frac{\delta S_1^z}{\delta x_3}$$

Interpolate u_1 to face center points in the x_2 direction and also find its $x_1 - x_3$

planar average

$$u_1^z \to u_1, \quad R_1 = \frac{\delta^0 u_1}{\delta x_2^0}, \quad \langle u_1 \rangle = \frac{1}{N_x N_z} \sum R_1, \quad u_1 \to u_1^z, \quad R_1 \to R_1^z$$

Begin computation of horizontally filtered hydrostatic pressure

$$\rho^z \to \rho, \qquad R_{2,j} = \rho_{j+1} + \rho_{j-1}, \qquad \rho \to \rho^z \to \rho^x, \qquad R_2 \to R_2^x$$
$$R_3^x = \rho_{i+1}^x + \rho_{i-1}^x, \qquad \rho_x \to \rho_z, \qquad R_3^x \to R_3^z$$
$$R_2^z = \frac{8\rho^z + R_2^z + R_3^z}{12}, \qquad R_4^z = \left(\frac{\delta}{\delta x_3}\right)^{-1} R_2^z$$
$$R_2^x = \rho^x - R_2^x, \qquad R_3^z = \frac{\delta^0 R_2^z}{\delta x_3^0}$$

Convert variables back to Fourier space and transpose

$$u_i^z \to u_i^x \to \hat{u}_i^x, \quad v_2 \to v_2^z \to v_2^x \to \hat{v}_2^x, \quad v_3^z \to v_3^x \to \hat{v}_3^x$$
$$\rho^z \to \rho^x \to \hat{\rho}^x, \quad F_i^z \to F_i^x \to \hat{F}_i^x, \quad F_\rho^z \to F_\rho^x \to \hat{F}_\rho^x$$
$$R_1^z \to R_1^x \to \hat{R}_1^x, \quad R_3^z \to R_3^x \to \hat{R}_3^x, \quad R_4^z \to R_4^x \to \hat{R}_4^x$$

Add buoyancy and Coriolis terms to $\hat{F}_i^x$

$$\hat{F}_1^x = \hat{F}_1^x + \frac{\hat{u}_2^x}{Ro}, \qquad \hat{F}_2^x = \hat{F}_2^x - \frac{\hat{R}_1^x}{Ro}, \qquad \hat{F}_3^x = \hat{F}_3^x - \hat{R}_3^x$$

Neglect the influence of $\langle u_1 \rangle$ on rotation

$$\hat{F}_2^x\,(k_x = 0) = \hat{F}_2^x\,(k_x = 0) + \frac{\langle u_1 \rangle}{Ro}$$

Add viscous terms to right hand side, beginning with $\partial^2/\partial x_1^2$ terms

$$\hat{F}_1^x = \hat{F}_1^x - \frac{k_x^2}{RoEk}\hat{u}_1^x, \qquad \hat{F}_2^x = \hat{F}_2^x - \frac{k_x^2}{RoEk}\hat{v}_2^x$$
$$\hat{F}_3^x = \hat{F}_3^x - \frac{k_x^2}{RoEk}\hat{v}_3^x, \qquad \hat{F}_\rho^x = \hat{F}_\rho^x - \frac{k_x^2}{RoEk}\hat{\rho}^x$$

The right hand side terms of the momentum equations are then transposed

such that the x_2 direction is contiguous for multigrid. Next pressure is computed (combined with velocity projection) and pressure gradient terms are added to $\hat{F}$.

$$\hat{R}_1^x = ik_x\left(\hat{F}_1^x + \beta_{rk}\Delta t\hat{u}_1^x\right) + k_x^2\hat{R}_4^x \qquad \hat{R}_1^x \to \hat{R}_1^z \qquad \hat{R}_4^x \to \hat{R}_4^z \qquad \hat{F}_2^x \to \hat{F}_2^z$$

$$\hat{F}_3^x \to \hat{F}_3^z \qquad \hat{v}_i^x \to \hat{v}_i^z$$

$$\hat{R}_1^z = \hat{R}_1^z + \frac{\delta\hat{F}_3^z}{\delta x_3} + \beta_{rk}\Delta t\frac{\delta\hat{v}_3^z}{\delta x_3} \qquad \hat{R}_1^z \to \hat{R}_1 \qquad \hat{R}_4^z \to \hat{R}_4$$

$$\hat{F}_2^z \to \hat{F}_2 \qquad \hat{v}_2^z \to \hat{v}_2$$

$$\hat{R}_1 = \hat{R}_1 + \frac{\delta\hat{F}_2}{\delta x_2} + \beta_{rk}\Delta t\frac{\delta\hat{v}_2}{\delta x_2} - \frac{\delta^2\hat{R}_4}{\delta x_2^2}$$

$$-k_x^2\hat{p} + \frac{\delta^2\hat{p}}{\delta x_2^2} + \frac{\delta^2\hat{p}}{\delta x_3^2} = \hat{R}_1 \qquad \hat{R}_1 = \hat{p}$$

$$\hat{F}_2 = \hat{F}_2 - \frac{\delta\hat{R}_1}{\delta x_2} - \frac{\delta\hat{R}_4}{\delta x_2} \qquad \hat{R}_1 \to \hat{R}_1^z \qquad \hat{R}_4 \to \hat{R}_4^z \qquad \hat{F}_2 \to \hat{F}_2^z$$

$$\hat{F}_3^z = \hat{F}_3^z - \frac{\delta\hat{R}_1^z}{\delta x_3} \qquad \hat{R}_1^z \to \hat{R}_1^x \qquad \hat{R}_4^z \to \hat{R}_4^x$$

$$\hat{F}_2^z \to \hat{F}_2^x \qquad \hat{F}_3^z \to \hat{F}_3^x$$

$$\hat{F}_1^x = \hat{F}_1^x - ik_x\left(\hat{R}_1^x + \hat{R}_4^x\right)$$

Next convert to physical space using inverse FFTs and update flow variables

$$\hat{u}_1^x \to u_1^x, \qquad \hat{v}_i^x \to v_i^x, \qquad \hat{\rho}^x \to \rho^x$$

$$u_1^x = u_1^x + \beta_{rk}\Delta tF_1^x, \qquad v_i^x = v_i^x + \beta_{rk}\Delta tF_i^x, \qquad \rho^x = \rho^x + \beta_{rk}\Delta tF_\rho^x$$

The collocated velocities are calculated via 6th order interpolation

$$v_3^x \to v_3^z \qquad v_2^x \to v_2^z \to v_2 \qquad u_3^z = \frac{\delta^0 v_3^z}{\delta x_3^0} \qquad u_2 = \frac{\delta^0 v_2}{\delta x_2^0}$$

$$u_3^z \to u_3^x \qquad v_3^z \to v_3^x \qquad u_2 \to u_2^z \to u_2^x \qquad v_2 \to v_2^z \to v_2^x$$

C.5 Differentiation

When 6th order compact finite difference is used with a Cartesian grid then the finite difference derivatives (including the zeroth) are calculated as follows

$$\begin{aligned}
\frac{3}{10}\hat{f}_{j-1} + \hat{f}_j + \frac{3}{10}\hat{f}_{j+1} &= \frac{3}{4}\left(\hat{f}_{j-0.5} + \hat{f}_{j+0.5}\right) + \frac{1}{20}\left(\hat{f}_{j-1.5} + \hat{f}_{j+1.5}\right) \\
\frac{9}{62}\hat{f}'_{j-1} + \hat{f}'_j + \frac{9}{62}\hat{f}'_{j+1} &= \frac{63}{62}\frac{\hat{f}_{j+0.5} - \hat{f}_{j-0.5}}{\Delta x} + \frac{17}{62}\frac{\hat{f}_{j+1.5} - \hat{f}_{j-1.5}}{3\Delta x} \\
\frac{1}{3}\hat{f}'_{j-1} + \hat{f}'_j + \frac{1}{3}\hat{f}'_{j+1} &= \frac{14}{9}\frac{\hat{f}_{j+1} - \hat{f}_{j-1}}{2\Delta x} + \frac{1}{9}\frac{\hat{f}_{j+2} - \hat{f}_{j-2}}{4\Delta x} \\
\frac{2}{11}\hat{f}''_{j-1} + \hat{f}''_j + \frac{2}{11}\hat{f}''_{j+1} &= \frac{12}{11}\frac{\hat{f}_{j+1} - 2\hat{f}_j + \hat{f}_{j-1}}{\Delta x^2} + \frac{3}{11}\frac{\hat{f}_{j+2} - 2\hat{f}_j + \hat{f}_{j-2}}{4\Delta x^2}
\end{aligned}$$

The terminating stencils are shown below

$$\begin{aligned}
\hat{f}_j + \hat{f}_{j+1} &= \frac{3}{2}\hat{f}_{j+0.5} + \frac{1}{4}\left(\hat{f}_{j-0.5} + \hat{f}_{j+1.5}\right) + \mathcal{O}\left(\Delta x^4\right) \\
\hat{f}'_j - \hat{f}'_{j+1} &= \frac{2\hat{f}_{j+0.5} - \hat{f}_{j-0.5} - \hat{f}_{j+1.5}}{\Delta x} + \mathcal{O}\left(\Delta x^3\right) \\
\hat{f}'_j + \hat{f}'_{j+1} &= \frac{3}{2}\frac{\hat{f}_{j+1} - \hat{f}_j}{\Delta x} + \frac{1}{2}\frac{\hat{f}_{j+2} - \hat{f}_{j-1}}{3\Delta x} + \mathcal{O}\left(\Delta x^4\right) \\
\hat{f}''_j - \hat{f}''_{j+1} &= \frac{\hat{f}_{j+1} - 2\hat{f}_j + \hat{f}_{j-1}}{\Delta x^2} - \frac{\hat{f}_{j+2} - 2\hat{f}_{j+1} + \hat{f}_j}{\Delta x^2} + \mathcal{O}\left(\Delta x^3\right)
\end{aligned}$$

C.6 Inhomogeneous Pressure Boundary Conditions

Similar to Marshall et al. JGR (1997) we avoid inhomogeneous boundary conditions during the multigrid pressure solve by defining hydrostatic and non-hydrostatic pressure components

$$p = p_H + p_N \qquad\qquad p_H = -\int_{x_3}^{x_{ref}} \rho dx_3'$$

Adding the influence of the hydrostatic pressure to the vertical momentum equation has the effect of canceling the buoyancy term

$$\begin{aligned}\frac{\partial u_3}{\partial t} &= -\frac{\partial}{\partial x_j}\left(u_j u_3\right) - \rho + Re^{-1}\frac{\partial^2 u_3}{\partial x_j^2} - \frac{\partial p_H}{\partial x_3} - \frac{\partial p_N}{\partial x_3} \\ &= -\frac{\partial}{\partial x_j}\left(u_j u_3\right) + Re^{-1}\frac{\partial^2 u_3}{\partial x_j^2} - \frac{\partial p_N}{\partial x_3}\end{aligned}$$

The full pressure solve becomes

$$\frac{\partial^2 p_N}{\partial x_j^2} + \frac{\partial^2 p_H}{\partial x_j^2} = \frac{\partial^2 p_N}{\partial x_j^2} + \frac{\partial^2 p_H}{\partial x_h^2} - \frac{\partial \rho}{\partial x_3} = \frac{\partial F_j}{\partial x_j} \quad \rightarrow \quad \frac{\partial^2 p_N}{\partial x_j^2} = \frac{\partial F_j}{\partial x_j} - \frac{\partial^2 p_H}{\partial x_h^2}$$

Implying that the filtered buoyancy term is also dropped from the pressure solve. To compute p_H we integrate the expression using the trapezoidal rule

$$\int_{x_0}^{x_0+h} f(x)dx = \frac{h}{2}\left[f(x_0) + f(x_0+h)\right] + \mathcal{O}(h^3)$$

Boundary conditions on full pressure are then

$$\frac{\partial p}{\partial x_3} = \frac{\partial p_H}{\partial x_3} + \frac{\partial p_N}{\partial x_3} = -\rho \qquad \text{provided} \qquad \frac{\partial p_N}{\partial x_3} = 0$$

Giving homogeneous Neumann boundary conditions for p_N, as desired.

C.7 Validation : Taylor-Green Vortices

To assess implementation of the flow solver two-dimensional Taylor-Green vortices are evolved. The velocity fields for a domain of $[0, L_1] \times [-L_y/2, L_y/2] \times [-L_z/2, L_z/2]$ and corresponding wavenumbers k_2 and k_3. The velocity fields are given to be the following for $k_2 = k_3$

$$u_2 = \sin(kx_2)\cos(kx_3)\exp\left(-2\nu k^2 t\right), u_3 = -\cos(kx_2)\sin(kx_3)\exp\left(-2\nu k^2 t\right)$$

Average kinetic energy therefore is given by

$$\frac{1}{2A}\iint u_2^2 + u_3^2 dA = \frac{\exp(-4\nu k^2 t)}{4}$$

At time $t = 59.90$ the average kinetic energy is found to be 9.726×10^{-2} compared to the value of 9.708×10^{-2} obtained using the relation above. Similarly, at time $t = 252.6$ the average kinetic energy is 4.630×10^{-3} compared to the value of 4.667×10^{-3}.

C.8 Validation : Shear Layer

The $Ri_{b,0} = 1.12$ case of chapter 2 was simulated with free slip and no through flow conditions at both vertical boundaries. Figure C.2 shows direction comparisons between root mean square lateral velocity fluctuations and late-time turbulent kinetic energy budgets from both cases. Agreement is very good, outside of the dissipation term. This term differs because the initial conditions were not matched.

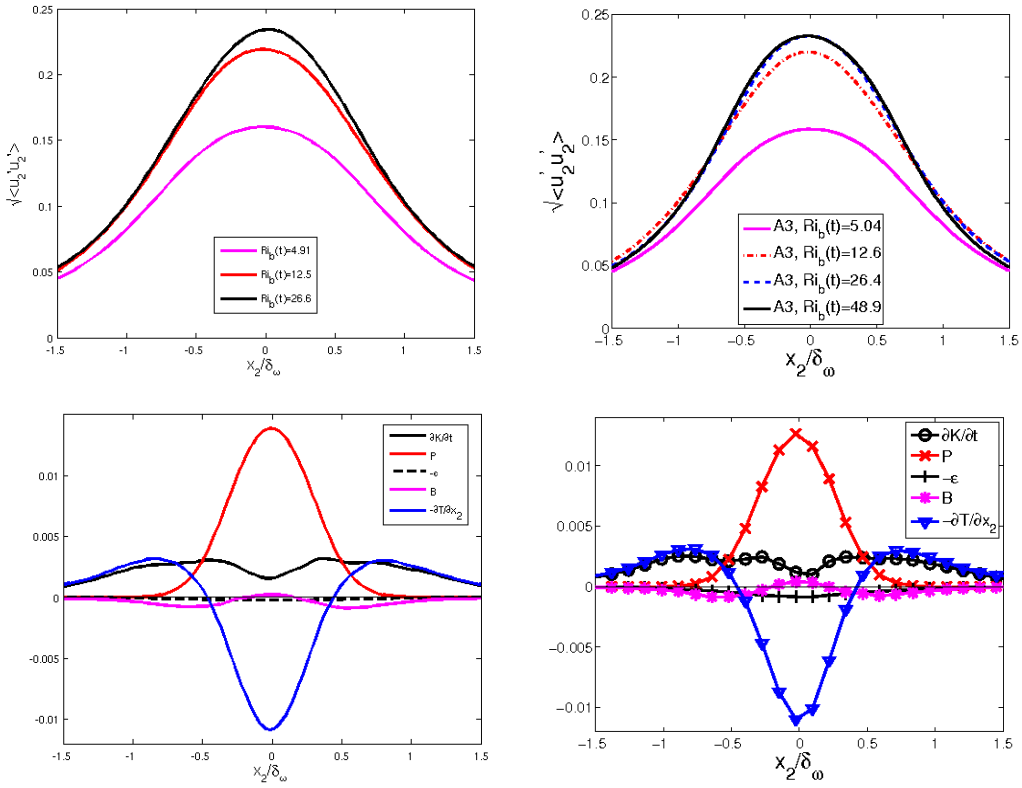

Figure C.2: Evolution of $\sqrt{< u_2' u_2' >}$ is shown (top) and turbulent kinetic energy budgets are computed for $t \approx 71$ (bottom). The left plots are from the duct solver, while the right plots are from chapter 2.

Appendix D

Fourth-Order Parallel Two-Dimensional Multigrid

D.1 Smoother

A fourth order compact finite difference stencil is used to approximate $\nabla^2\hat{\phi} = \hat{f}$ on a uniform two-dimensional grid with spacing Δx

$$\frac{1}{6\Delta x^2}\begin{bmatrix} 1 & 4 & 1 \\ 4 & -20 & 4 \\ 1 & 4 & 1 \end{bmatrix}\hat{\phi} - \frac{1}{12}\begin{bmatrix} 0 & 1 & 0 \\ 1 & 8 & 1 \\ 0 & 1 & 0 \end{bmatrix}k^2\hat{\phi} = \frac{1}{12}\begin{bmatrix} 0 & 1 & 0 \\ 1 & 8 & 1 \\ 0 & 1 & 0 \end{bmatrix}\hat{f} \qquad \text{(D.1)}$$

From this and boundary conditions we can formulate a system of equations of the form $\boldsymbol{A}x = b$. The above stencil is derived from the 2D Mehrstellen discretization and its order of accuracy is demonstrated in appendix A. An iterative approach is used to solve the system of equations, this approach also functions as a smoother. Red-black Gauss-Seidel method is ideal for second order multigrid on uniform grids, but not appropriate because of the nine-point stencil used on the left hand side of equation (D.1). A four-color Gauss-Seidel method or red-black Jacobi method can be used instead. We choose the latter method because it requires two as opposed to four parallel communications per iteration with a similar convergence rate (Trottenberg *et al.*, 2001). The method is outlined below for a checkerboard

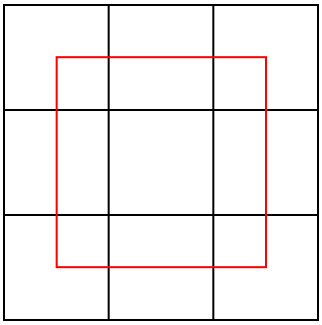

Figure D.1: Fine grid (black) and corresponding coarse grid (red).

grid where D and H represent the diagonal and hallow matrix decomposition of A, respectively,

$$\begin{aligned} &\text{updating half of checkerboard points :} && \hat{\phi}_{s+1/2} = D^{-1}H\hat{\phi}_s \\ &\text{updating other checkerboard points :} && \hat{\phi}_{s+1} = D^{-1}H\hat{\phi}_{s+1/2} \end{aligned}$$

MPI send and receive calls are needed after each substep, but only in the x_3 direction.

D.2 Restriction

When moving to a coarser grid equation (D.1) only changes in the sense that Δx is modified. The residual on the other hand must be restricted from fine values to coarse values. We use a cell-centered multigrid approach which is illustrated in Figure D.1. For the simple uniform grid a simple bilinear interpolation scheme for restricting residual $r = b - A\hat{x}$ follows

$$r'_{i,j} = \frac{1}{4}\left(r_{2i-1,2j-1} + r_{2i,2j-1} + r_{2i-1,2j} + r_{2i,2j}\right)$$

D.3 Prolongation

When moving to a finer grid the solution must be improved using the coarse grid solution. Simple uniform grid bilinear interpolation gives

$$
\begin{aligned}
e_{2i,2j} &= \frac{1}{16}\left(9e'_{i,j} + 3e'_{i,j+1} + 3e'_{i+1,j} + e'_{i+1,j+1}\right) \\
e_{2i+1,2j} &= \frac{1}{16}\left(9e'_{i+1,j} + 3e'_{i,j} + 3e'_{i+1,j+1} + e'_{i,j+1}\right) \\
e_{2i,2j+1} &= \frac{1}{16}\left(9e'_{i,j+1} + 3e'_{i,j} + 3e'_{i+1,j+1} + e'_{i+1,j}\right) \\
e_{2i+1,2j+1} &= \frac{1}{16}\left(9e'_{i+1,j+1} + 3e'_{i+1,j} + 3e'_{i,j+1} + e'_{i,j}\right)
\end{aligned}
$$

D.4 Parallelization

The domain is only split in one of the two multigrid directions allowing for straightforward parallelization. Non-blocking sends are used to transfer one line of data between processes with data first being sent left-to-right followed by right-to-left. Serial multigrid is also available to increase the total number of multigrid levels beyond the maximum number allowed by parallel multigrid. Coarse grids of size NY/NR x NZ/NR and smaller are smoothed on the root process of each column.

D.5 The Mehrstellen Discretization

Below is the Mehrstellen 4th order Laplacian operator for a isotropic uniform grid

$$
\frac{1}{6\Delta x^2}\begin{bmatrix} 1 & 4 & 1 \\ 4 & -20 & 4 \\ 1 & 4 & 1 \end{bmatrix}\hat{x} = \frac{1}{12}\begin{bmatrix} 0 & 1 & 0 \\ 1 & 8 & 1 \\ 0 & 1 & 0 \end{bmatrix}\hat{f}
$$

We will derive the Laplacian operator for an anisotropic grid The 5th order Taylor series expansions of $\hat{x}$ (and similarly $\hat{f}$) are given as (let $\alpha = \Delta y/\Delta x$ and $h = \Delta x$)

$$\begin{aligned}
\hat{x}_{0,0} &= \hat{x}_{0,0} \\
\hat{x}_{0,\pm1} &= \hat{x}_{0,0} \pm h\hat{x}_{,x} + \frac{h^2}{2}\hat{x}_{,xx} \pm \frac{h^3}{6}\hat{x}_{,xxx} + \frac{h^4}{24}\hat{x}_{,xxxx} \\
\hat{x}_{\pm1,0} &= \hat{x}_{0,0} \pm ah\hat{x}_{,y} + \frac{\alpha^2h^2}{2}\hat{x}_{,yy} \pm \frac{\alpha^3h^3}{6}\hat{x}_{,yyy} + \frac{\alpha^4h^4}{24}\hat{x}_{,yyyy} \\
\hat{x}_{\pm1,1} &= \hat{x}_{0,0} \pm h\hat{x}_{,x} + \alpha h\hat{x}_{,y} + \frac{h^2}{2}\left[\hat{x}_{,xx} \pm 2\alpha\hat{x}_{,xy} + \alpha^2\hat{x}_{,yy}\right] \\
&\quad + \frac{h^3}{6}\left[\pm\hat{x}_{,xxx} + 3\alpha\hat{x}_{,xxy} \pm 3\alpha^2\hat{x}_{,xyy} + \alpha^3\hat{x}_{,yyy}\right] \\
&\quad + \frac{h^4}{24}\left[\hat{x}_{,xxxx} \pm 4\alpha\hat{x}_{,xxxy} + 6\alpha^2\hat{x}_{,xxyy} \pm 4\alpha^3\hat{x}_{,xyyy} + \alpha^4\hat{x}_{,yyyy}\right] \\
\hat{x}_{1,\pm1} &= \hat{x}_{0,0} + h\hat{x}_{,x} \pm \alpha h\hat{x}_{,y} + \frac{h^2}{2}\left[\hat{x}_{,xx} \pm 2\alpha\hat{x}_{,xy} + \alpha^2\hat{x}_{,yy}\right] \\
&\quad + \frac{h^3}{6}\left[\hat{x}_{,xxx} \pm 3\alpha\hat{x}_{,xxy} + 3\alpha^2\hat{x}_{,xyy} \pm \alpha^3\hat{x}_{,yyy}\right] \\
&\quad + \frac{h^4}{24}\left[\hat{x}_{,xxxx} \pm 4\alpha\hat{x}_{,xxxy} + 6\alpha^2\hat{x}_{,xxyy} \pm 4\alpha^3\hat{x}_{,xyyy} + \alpha^4\hat{x}_{,yyyy}\right]
\end{aligned}$$

Assuming matrices of the form

$$A = \begin{bmatrix} d & b & d \\ c & a & c \\ d & b & d \end{bmatrix} \qquad B = \begin{bmatrix} 0 & q & 0 \\ r & p & r \\ 0 & q & 0 \end{bmatrix}$$

$A\hat{x} = B\hat{f}$ satisfies Poisson's equation to fourth order accuracy provided the following equations are satisfied (note that $\hat{f} = \hat{x}_{,xx} + \hat{x}_{,yy}$)

$$\begin{aligned}
(a + 2b + 2c + 4d)\hat{x} = 0 \qquad & (\alpha^2h^2c + 2\alpha^2h^2d)\hat{x}_{yy} - \hat{x}_{yy} = 0 \\
\alpha^2h^4d\hat{x}_{,xxyy} - (h^2q + \alpha^2h^2r)\hat{x}_{,xxyy} = 0 \qquad & (p + 2q + 2r)\hat{f} - \hat{f} = 0 \\
(h^4b + 2h^4d)\hat{x}_{,xxxx} - 12h^2q\hat{x}_{,xxxx} = 0 \qquad & (h^2b + 2h^2d)\hat{x}_{,xx} - \hat{x}_{,xx} = 0 \\
(\alpha^4h^4c + 2\alpha^4h^4d)\hat{x}_{,yyyy} - 12\alpha^2h^2r\hat{x}_{,yyyy} = 0 &
\end{aligned}$$

Solving this system of equations gives A and B of the form

$$A = \begin{bmatrix} \alpha^2+1 & 2(5\alpha^2-1) & \alpha^2+1 \\ -2(\alpha^2-5) & -20(\alpha^2+1) & -2(\alpha^2-5) \\ \alpha^2+1 & 2(5\alpha^2-1) & \alpha^2+1 \end{bmatrix} \qquad B = \alpha^2 h^2 \begin{bmatrix} 0 & 1 & 0 \\ 1 & 8 & 1 \\ 0 & 1 & 0 \end{bmatrix}$$

The three dimensional Poisson solve takes the form $A\hat{x} = B(\hat{f} + k^2\hat{x})$, substitution gives A of the form

$$A = \begin{bmatrix} \alpha^2+1 & 2(5\alpha^2-1)-(\alpha kh)^2 & \alpha^2+1 \\ -2(\alpha^2-5)-(\alpha kh)^2 & -20(\alpha^2+1)-8(\alpha kh)^2 & -2(\alpha^2-5)-(\alpha kh)^2 \\ \alpha^2+1 & 2(5\alpha^2-1)-(\alpha kh)^2 & \alpha^2+1 \end{bmatrix}$$

D.6 Validation

We wish to solve $\nabla^2\phi = f$, using ϕ of the following forms over the domain $[0,1]\times[0,1]$

$$\begin{aligned} \phi_1(x_i) &= \exp\left[-\sigma^2\left(x_2^2+x_3^2\right)\right]\sin(kx_1)\sin(kx_2)\sin(kx_3) \\ \phi_2(x_i) &= \left(x_2^4 - x_2^2/4\right)\left(x_3^4 - x_3^2/4\right) \\ \phi_3(x_i) &= \sin(kx_1)\sin(kx_2)\sin(kx_3) \\ \phi_4(x_i) &= \cos(kx_1)\cos(kx_2)\cos(kx_3) \end{aligned}$$

The three right hand sides given above are inputted as source terms into the Poisson solver. Table D.1 gives a 'best case' residual, R, which is computed by comparing the exact right hand side values with values of $A\phi$ (finite difference approximation of $\nabla^2\phi$). Additionally several errors are computed for different values of max residual r, where $r\|\hat{f}\| = \|A\hat{\phi} - \hat{f}\|$ is less than 10^{-4}, 10^{-6}, or 10^{-10}. Ideally we would like the residual to be comparable to the errors in approximating $\hat{f}$ using $A\hat{\phi}$ for an exact $\hat{\phi}$. Case 1 has gradients isolated from the x_2 and x_3 boundaries, while case 2 gradients are concentrated near the boundaries. Cases 3 and 4 are homogeneous using Dirichlet and Neumann boundary conditions, respectively. For an unknown reason for case 2 the errors outperform the 'best' case value considerably. Table

Table D.1: Normalized residuals for 256^3 domain using 8-grid. Here $R = \|A\hat{\phi} - \hat{f}\|\|\hat{f}\|^{-1}$ and $e = \|\tilde{\phi} - \hat{\phi}\|\|\hat{\phi}\|^{-1}$. Errors are computed using three different values of max residual.

case	1	1	1	2	3	3	3	4	4	4
k	8	32	64		8	32	64	8	32	64
σ	8	32	64							
R	6e-7	2e-4	2e-3	2e-2	2e-7	4e-5	7e-4	3e-7	4e-5	7e-4
e_{-4}	5e-5	2e-4	3e-3	2e-4	4e-5	5e-5	7e-4	4e-5	5e-5	7e-4
e_{-6}	9e-7	2e-4	3e-3	2e-4	6e-7	5e-5	7e-4	5e-7	4e-5	7e-4
e_{-10}	7e-7	2e-4	3e-3	2e-4	3e-7	4e-5	7e-4	3e-7	4e-5	7e-4

Table D.2: Verification of order of accuracy for $k = 32\pi$ ($\sigma = 32$ for case 1) using a residual of 10^{-10}.

case	1	3	4
$e(256^3)$	1.68e-4	4.44e-5	4.36e-5
$e(512^3)$	1.04e-5	2.81e-6	2.75e-6
ratio	16.2	15.8	15.9

D.2 demonstrates the order of accuracy of the solver showing that increasing the number of points in each direction results in approximately a factor of 16 reduction in error.

Bibliography

Afanasyev, Y. D. & Peltier, W. R. 1998 The three-dimensionalization of stratified flow over two-dimensional topography. *J. Atmos. Sci.* **55**, 19–39.

Arobone, E. & Sarkar, S. 2010 The statistical evolution of a stratified mixing layer with horizontal shear invoking feature extraction. *Phys. Fluids* **22** (115108), 1–15.

Arobone, E. & Sarkar, S. 2012 Evolution of a stratified rotating shear layer with horizontal shear. i. linear stability. *J. Fluid Mech.* **703**, 29–48.

Bartello, P., Métais, O. & Lesieur, M. 1994 Coherent structures in rotating three-dimensional turbulence. *J. Fluid Mech.* **273**, 1–29.

Basak, S. & Sarkar, S. 2006 Dynamics of a stratified shear layer with horizontal shear. *J. Fluid Mech.* **568**, 19–54.

Billant, P. & Chomaz, J. 2001 Self-similarity of strongly stratified inviscid flows. *Phys. Fluids* **13** (6), 1645–1651.

Billant, P. & Chomaz, J.-M. 2000*a* Experimental evidence for a new instability of a vertical columnar vortex pair in a strongly stratified fluid. *J. Fluid Mech.* **418**, 167–188.

Billant, P. & Chomaz, J.-M. 2000*b* Experimental evidence for a new instability of a vertical columnar vortex pair in a strongly stratified fluid. *J. Fluid Mech.* **418**, 167–188.

Billant, P. & Chomaz, J.-M. 2000*c* Theoretical analysis of the zigzag instability of a vertical columnar vortex pair in a strongly stratified fluid. *J. Fluid Mech.* **419**, 29–63.

Blumen, W. 1971 Hydrostatic neutral waves in a parallel shear flow of a stratified fluid. *J. Atmos. Sci.* **28**, 340–344.

Browand, F., Guyomar, D. & Yoon, S.-C. 1987 The behavior of a turbulent front in a stratified fluid: experiments with an oscillating grid. *J. Geophys. Res.* **92** (C5), 5329–5341.

Brucker, K. & Sarkar, S. 2007 Evolution of an initially turbulent stratified shear layer. *Phys. Fluids* **19**, 101105.

Carnevale, G. F., Kloosterziel, R. C., Orlandi, P. & van Sommeren, D. D. J. A. 2011 Predicting the aftermath of vortex breakup in rotating flow. *J. Fluid Mech.* **669**, 90–119.

Chakraborty, P., Balachandar, S. & Adrian, R. J. 2005 On the relationships between local vortex identification schemes. *J. Fluid Mech.* **535**, 189–214.

Chong, M. S., Perry, A. E. & Cantwell, B. J. 1990 A general classification of three-dimensional flow fields. *Phys. Fluids A* **2** (5), 765–777.

D'Asaro, E., Lee, C., Rainville, L., Harcourt, R. & Thomas, L. 2011 Enhanced turbulence and energy dissipation at ocean fronts. *Science* **332**, 318–322.

Deloncle, A., Billant, P. & Chomaz, J. M. 2008 Nonlinear evolution of the zigzag instability in stratified fluids: a shortcut on the route to dissipation. *J. Fluid Mech.* **599**, 229–239.

Deloncle, A., Billant, P. & Chomaz, J.-M. 2011 Three-dimensional stability of vortex arrays in a stratified and rotating fluid. *J. Fluid Mech.* **678**, 482–510.

Deloncle, A., Chomaz, J.-M. & Billant, P. 2007 Three-dimensional stability of a horizontally sheared flow in a stably stratified fluid. *J. Fluid Mech.* **570**, 297–305.

Donoho, D. & Johnstone, J. 1994 Ideal spatial adaptation by wavelet shrinkage. *Biometrika* **81**, 425–455.

Eldevik, T. & Dysthe, K. 2002 Spiral eddies. *J. Phys. Oceanogr.* **32**, 851–869.

Farge, M., Pellegrino, G. & Schneider, K. 2001 Coherent vortex extraction in 3d turbulent flows using orthogonal wavelets. *Phys. Rev. Lett.* **87**, 054501.

Flament, P., Armi, L. & Washburn, L. 1985 The evolving structure of an upwelling filament. *J. Geophys. Res.* **90**, 11765–11778.

Flament, P., Lumpkin, R., Tournadre, J. & Armi, L. 2001 Vortex pairing in an unstable anticyclonic shear flow: discrete subharmonics of one pendulum day. *J. Fluid Mech.* **440**, 401–409.

Gent, P. & McWilliams, J. 1983*a* Consistent balanced models in bounded and periodic domains. *Dyn. Atmos. Oceans* **7**, 67–93.

Gent, P. & McWilliams, J. 1983*b* Regimes of validity for balanced models. *Dyn. Atmos. Oceans* **7**, 167–183.

Haller, G. 2005 An objective definition of a vortex. *J. Fluid Mech.* **525**, 1–26.

Hosegood, P., Gregg, M. & Alford, M. 2006 Sub-mesoscale lateral density structure in the oceanic surface mixed layer. *Geophys. Res. Lett.* **33** (L22604).

Hoskins, B. 1974 The role of potential vorticity in symmetric stability and instability. *Q. J. R. Meteorol. Soc.* **100**, 480–482.

Ivey, G. N. & Corcos, G. M. 1982 Boundary mixing in a stratified fluid. *J. Fluid Mech.* **121**, 1–26.

Jacobitz, F. G., Liechtenstein, L., Schneider, K. & Farge, M. 2008 On the structure and dynamics of sheared and rotating turbulence: direct numerical simulation and wavelet-based coherent vortex extraction. *Phys. Fluids* **20**, 045103.

Jacobitz, F. G. & Sarkar, S. 1998 The effect of nonvertical shear on turbulence in a stably stratified medium. *Phys. Fluids* **10**, 1158–1168.

Jacobitz, F. G. & Sarkar, S. 2000 A direct numerical study of transport and anisotropy in a stably stratified turbulent flow with uniform horizontal shear **63**, 343–360.

Jeong, J. & Hussain, F. 1995 On the identification of a vortex. *J. Fluid Mech.* **285**, 69–94.

Johnson, J. A. 1963 The stability of shearing motion in a rotating fluid. *J. Fluid Mech.* **17**, 337–352.

Jones, S. & Thorpe, A. 1992 The three-dimensional nature of 'symmetric' instability. *Q. J. R. Meteorol. Soc.* **118**, 227–258.

Kerswell, R. R. 2002 Elliptical instability. *Ann. Rev. Fluid Mech.* **34**, 83–113.

Kloosterziel, R. C., Carnevale, G. F. & Orlandi, P. 2007*a* Inertial instability in rotating and stratified fluids: barotropic vortices. *J. Fluid Mech.* **583**, 379–412.

Kloosterziel, R. C. & van Heijst, G. J. F. 1991 An experimental study of unstable barotropic vortices in a rotating fluid. *J. Fluid Mech.* **223**, 1–24.

Kloosterziel, R. C., Orlandi, P. & Carnevale, G. F. 2007*b* Saturation of inertial instability in rotating planar shear flows. *J. Fluid Mech.* **583**, 413–422.

Koop, C. G. & Browand, F. K. 1979 Instability and turbulence in a stratified fluid with shear. *J. Fluid Mech.* **93**, 135–159.

Kunze, E. & Sanford, T. 1993 Submesoscale dynamics near a seamount. part i: Measurements of ertel vorticity. *J. Phys. Oceanogr.* **23**, 2567–2588.

Lesieur, M., Yanase, S. & Métais, O. 1991 Stabilizing and destabilizing effects of a solid-body rotation on quasi-two-dimensional shear layers. *Phys. Fluids A* **3** (3), 403–407.

Lilly, D. K. 1973 Stratified turbulence and the mesoscale variability of the atmosphere. *J. Atmos. Sci.* **40**, 749–761.

Liu, Y., Maxworthy, T. & Spedding, G. 1987 Collapse of a turbulent front in a stratified fluid 1. nominally two-dimensional evolution in a narrow tank. *J. Geophys. Res.* **92** (C5), 5427–5433.

Mamatsashvili, G., Vsarlosov, V., Hagelishvili, G., Hanishvili, R. & Kalashnik, M. 2010 Transient dynamics of nonsymmetric perturbations versus symmetric instability in baroclinic zonal shear flows. *J. Atmos. Sci.* **97**, 2972–2989.

McWilliams, J. 1985 Submesoscale, coherent vortices in the ocean. *Rev. Geophys.* **23**, 165–182.

McWilliams, J. 2010 A perspective on submesoscale geophysical turbulence. *IUTAM Symposium on Turbulence in the Atmosphere and Oceans* .

Métais, O., Flores, C., Yanase, S., Riley, J. J. & Lesieur, M. 1995 Rotating free-shear flows. part 2. numerical simulations. *J. Fluid Mech.* **293**, 47–80.

Meunier, P., Boulanger, N. & Dizès, S. L. 2007 Structure of a stratified tilted vortex. *J. Fluid Mech.* **583**, 443–458.

Molemaker, M., McWilliams, J. & Capet, X. 2010 Balanced and unbalanced routes to dissipation in an equilibrated eady flow. *J. Fluid Mech.* **654**, 35–63.

Molemaker, M., McWilliams, J. & Yavneh, I. 2005 Baroclinic instability and loss of balance. *J. Phys. Oceanogr.* **35**, 1505–1517.

Munk, W., Armi, L., Fischer, K. & Zachariasen, F. 2000 Spirals on the sea. *Proc. R. Soc. A* **456**, 1217–1280.

Otheguy, P., Billant, P. & Chomaz, J.-M. 2006*a* The effect of planetary rotation on the zigzag instability of co-rotating vortices in a stratified fluid. *J. Fluid Mech.* **553**, 273–281.

Otheguy, P., Billant, P. & Chomaz, J.-M. 2006*b* Elliptic and zigzag instabilities on co-rotating vertical vortices in a stratified fluid. *J. Fluid Mech.* **553**, 253–272.

Pantano, C. & Sarkar, S. 2002 A study of compressibility effects in the high-speed turbulent shear layer using direct simulation. *J. Fluid Mech.* **451**, 329–371.

Pham, H. & Sarkar, S. 2010 Internal waves and turbulence in a stable stratified jet. *J. Fluid Mech.* pp. 297–324.

Pham, H., Sarkar, S. & Brucker, K. A. 2009 Dynamics of a stratified shear layer above a region of uniform stratification. *J. Fluid Mech.* **630**, 191–223.

Pieri, A., Godeferd, F., Cambon, C. & Salhi, A. 2013 Non-geostrophic instabilities of an equilibrium baroclinic state. *J. Fluid Mech.* **734**, 535–566.

Plougonven, R. & Zeitlin, V. 2009 Nonlinear development of inertial instability in a barotropic shear. *Phys. Fluids* **21** (106601), 1–15.

Pollard, R. & Regier, L. 1992 Vorticity and vertical circulation at an ocean front. *J. Phys. Oceanogr.* **22**, 609–625.

Potylitsin, P. G. & Peltier, W. R. 1998 Stratification effects on the stability of columnar vortices on the f-plane. *J. Fluid Mech.* **355**, 45–79.

Potylitsin, P. G. & Peltier, W. R. 1999 Three-dimensional destabilization of stuart vortices. *J. Fluid Mech.* **387**, 205–226.

Potylitsin, P. G. & Peltier, W. R. 2003 On the nonlinear evolution of columnar vortices in a rotating environment. *Geophys. Astrophys. Fluid Dynamics* **97**, 365–391.

Praud, O., Sommeria, J. & Fincham, A. M. 2006 Decaying grid turbulence in a rotating stratified tank. *J. Fluid Mech.* **547**, 389–412.

Riley, J. J. & de Bruyn Kops, S. M. 2003 Dynamics of turbulence strongly influenced by buoyancy. *Phys. Fluids* **15** (7), 2047–2059.

Rogallo, R. S. 1981 Numerical experiments in homogeneous turbulence. *Tech. Rep.* 81315. NASA.

Rogers, M. M. & Moser, R. D. 1994 Direct simulation of a self-similar turbulent mixing layer. *Phys. Fluids* **6**, 903–923.

Smith, L. M. & Waleffe, F. 2002 Generation of slow large scales in forced rotating stratified turbulence. *J. Fluid Mech.* **451**, 145–168.

Smyth, W. D. & McWilliams, J. C. 1998 Instability of an axisymmetric vortex in a stably stratied, rotating environment. *Theoret. Comput. Fluid Dyn.* **11**, 305–322.

Smyth, W. D. & Moum, J. N. 2000*a* Anisotropy of turbulence in stably stratified mixing layers. *Phys. Fluids* **12** (6), 1343–1362.

Smyth, W. D. & Moum, J. N. 2000*b* Length scales of turbulence in stably stratified mixing layers. *Phys. Fluids* **12** (6), 1327–1342.

Smyth, W. D., Moum, J. N. & Caldwell, D. R. 2001 The efficiency of mixing in turbulent patches: Inferences from direct simulations and microstrucure observations. *J. Phys. Oceanogr.* **31**, 1969–1992.

Smyth, W. D. & Peltier, W. R. 1994 Three-dimensionalization of barotropic vortices on the f-plane. *J. Fluid Mech.* **265**, 25–64.

Stone, P. 1966 On non-geostrophic baroclinic stability. *J. Atmos. Sci.* **23**, 390–400.

Stone, P. 1970 On non-geostrophic baroclinic stability : Part ii. *J. Atmos. Sci.* **27**, 721–726.

Strang, E. J. & Fernando, H. J. S. 2001 Entrainment and mixing in stratified shear flows. *J. Fluid Mech.* **428**, 349–386.

Taylor, J. & Ferrari, R. 2009 On the equilibration of a symmetrically unstable front via a seconday shear instability. *J. Fluid Mech.* **622**, 103–113.

Thomas, L., Tandon, A. & Mahadevan, A. 2008 Sub-mesoscale processes and dynamics. *Geophysical Monograph Series* **177**, 17–38.

Thomas, L., Taylor, J., Ferrari, R. & Joyce, T. 2013 Symmetric instability in the gulf stream. *Deep-Sea Res. II* **91**, 96–110.

Thorpe, S. A. 1973 Experiments on instability and turbulence in a stratified shear flow. *J. Fluid Mech.* **61**, 731–751.

Thorpe, S. A. 1982 On the layers produced by rapidly oscillating a vertical grid in a uniformly stratified fluid. *J. Fluid Mech.* **124**, 391–409.

Trottenberg, U., Oosterlee, C. & Schuller, A. 2001 *Multigrid*. London: Academic Press.

Tse, K. L., Mahalov, A., Nicolaenko, B. & Fernando, H. J. S. 2003 Quasi-equilibrium dynamics of shear-stratified turbulence in a model tropospheric jet. *J. Fluid Mech.* **496**, 73–103.

Waite, M. L. & Smolarkiewicz, P. K. 2008 Instability and breakdown of a vertical vortex pair in a strongly stratified fluid. *J. Fluid Mech.* **606**, 239–273.

Williamson, J. H. 1980 Low-storage Runge-Kutta schemes. *J. Comput. Phys.* **35**, 48–56.

Winant, C. D. & Browand, F. K. 1974 Vortex pairing : the mechanism of turbulent mixing-layer growth at moderate reynolds number. *J. Fluid Mech.* **63** (2), 237–255.

W.R., P. & Caulfield, C. 2003 Mixing efficiency in stratified shear flows. *Ann. Rev. Fluid Mech.* **35**, 135–167.

Yanase, S., Flores, C., Métais, O. & Riley, J. J. 1993 Rotating free-shear flows. I. Linear stability analysis. *Phys. Fluids* **5** (11), 2725–2737.